APPLICATION OF HIGHLY POROUS CARBONS FOR ELECTROCHEMICAL ENERGY STORAGE DEVICES

A Dissertation
Presented to
The Academic Faculty

by

Wentian Gu

In Partial Fulfillment
of the Requirements for the Degree
Doctor of Philosophy in the
School of Materials Science and Engineering

Georgia Institute of Technology
August 2015

APPLICATION OF HIGHLY POROUS CARBONS FOR ELECTROCHEMICAL ENERGY STORAGE DEVICES

Approved by:

Dr. Gleb Yushin, Advisor
School of Materials Science and Engineering
Georgia Institute of Technology

Dr. Faisal Alamgir,
School of Materials Science and Engineering
Georgia Institute of Technology

Dr. Ting Zhu,
School of Materials Science and Engineering
Georgia Institute of Technology

Dr. Alexander Alexeev,
School of Mechanical Engineering
Georgia Institute of Technology

Dr. Thomas Fuller,
School of Chemical & Biomolecular Engineering
Georgia Institute of Technology

Date approved: July 2, 2015

To my Family.

ACKNOWLEDGEMENTS

I would like to thank my parents who make me possible in the splendid world. Their love empowered and enlightened my life.

My sincere appreciations to my Advisor Professor Gleb Yushin for all his patient guidance, strong support, and kind encouragement over the years. I have learned much from his solid and profound knowledge, smart and logical thoughts about the research. I am also encouraged by his high spirit and optimistic characters shown in his research career. Also many thanks to Prof. Thomas Fuller, Prof. Zhiqun Lin, Prof. Faisal Alamgir and Prof. Alexander Alexeev for taking their precious time to be on my committee and providing me with valuable feedback.

I thank Huan-Ting Lin who contributed significantly to the works in this thesis. I was pleased to have the opportunity to work with Dr. S. Marta. The wonderful discussions and materials she provided greatly helped progress this project. I would like to thank Dr. Bogdan Zdyrko at Sila Nanotechnologies, Inc. and Dr. Oleg Borodin at US Army Lab for their contributions to the work presented.

I thank Dr. Hyea Kim for giving key suggestions and help in research, Dr. Alexander Magasinski, Naoki Nitta and Cindy Huang for their help with materials characterizations, analysis and data interpretations. Thanks to Dr. Lu Wei for her kind help during my early days in this amazing group. I thank all current and former members of the Yushin Lab including Dr. Jong Seok Moon, Ben Hertzberg, Yair Korenblit, Kara Evanoff, Jim Benson, Dr. Igor Kovalenko, Sofiane Boukhalfa, Prof. Vojtech Svoboda, Youyang Zhao, Jessica Hong, Enbo Zhao, Xinran Wang, Prof. Chuanli Qin, Danni Lei,

Prof. Hailei Zhao, Prof. Junjun Wei, Daniel Gordon, Anirudh Ramanujapuram, Georges Nassif and many others for their assistance and warm friendship.

I would like to thank all my dear friends who have accompanied and testified my life here at Georgia Tech: Dr. Yiming Chen, Dr. Sihong Wang, Dr. Yunlong Zi, Dr. Wenzhuo Wu, Dr. Fan Bai, Dr. Wei Lin, Dr. Zhuo Li and Dr. Xiaonan Wen. Thank you all for your friendship, encouragement and support which helped me overcome the difficulties and fight through.

Special thanks to my wife Di Mei for her consistent support and encouragement during my Ph.D. studies. When I decided to go abroad to pursue PhD study, she supported my decision and we have kept our love promised to each other ever since. She managed to survive and thrive alone without my accompany in Beijing. Without her understanding and sacrifices, I would not have been able to achieve my degree. I am proud of her.

TABLE OF CONTENTS

LIST OF TABLES

LIST OF FIGURES

SUMMARY

Modernized and large scale industrialization has lead to the rapidly increasing energy consumption and foreseeable exhaustion of conventional fossil fuels, which obliged the researchers to seek for alternative renewable power source to support sustainable development of the society. By now, most of the cultivated renewable energies are converted and stored in the form of electricity in electrochemical energy storage devices. Many essential applications of electricity power source, such as in portable electronics, electric vehicles, aircraft, satellites, etc. demand for high specific and volumetric energy density, high power, and long cycle life of the energy storage devices, especially currently applied high-power supercapacitors and high energy density Li-ion batteries. Therefore, it is necessary to improve the performance of the electrode materials for these energy storage devices to meet the target for future electricity powered products.

Highly porous carbon plays an important role in the fabrication of electrode materials, both for high-power supercapacitors and Li-ion batteries. It qualifies as suitable electrodes for high-power supercapacitors, thanks to its large surface area and high electrical conductivity. To further increase the specific capacitance of porous carbons, researchers have proposed heavy surface functionalization on carbon materials for additional pseudocapacitance. However, the potential negative effects caused by the surface functionalizations, including promoted self-discharge, shrinkage of electrochemical window of electrolyte and more sluggish rate performance, have been long-overlooked. As the first topic of this thesis, I discuss the effect of oxygen-containing functional groups (including hydroxyl, carbonyl and carboxyl groups) on the self-

discharge behavior of carbon-based electrical double layer supercapacitors (EDLCs). The effects of carbon pore size and pore size distribution, pore alignment, electrolyte solvent and conducting ion are also studied. Based on the understandings of these multiple factors which have impact on the performance of carbon-based EDLCs, I describe a novel S-doped activated carbon synthesized by carbonization and simultaneous activation of S-based polymers, which is almost free of bottle-neck pores and performs excellent capacitance and capacitance retention.

Besides their essential role in carbon-based EDLCs, highly porous carbon materials have also been intensively studied as structural scaffold and conductive additives to assist the highly capacitive but poorly conductive active electrode materials for Li-ion batteries. In the second part of this work, I discuss the application of mesoporous activated carbon spheres as structural matrix and conductive 3D network which enables higher capacity, better rate retention and longer cycle life of metal fluoride-based cathode materials, compared to the simple mixture of non-porous conductive carbon filler and the active material.

As a whole, this dissertation expands our understandings of key parameters influencing the application of highly porous carbon materials for multiple energy storage devices, and demonstrates the possibility of improving the performance of carbon-based energy storage devices via optimizing these parameters.

CHAPTER 1

MOTIVATION AND PROBLEM STATEMENT

Production and storage of clean and renewable energy has become one of the most exciting yet challenging topics in recent decades. The pressing need for green energy production and efficient energy storage has been further emphasized by the shortage of conventional energy sources and the continuous environment deterioration. While many forms of natural energy, such as solar, wind, and water power, have been considered candidates for the next-generation energy sources, electrochemical energy storage devices, such as rechargeable batteries and supercapacitors, dominate the solutions for the transmittance and storage of renewable energy. By now, these devices have been commercialized and applied in a wide range of industries, ranging from portable electronics to transportation to military and aerospace.

Two major categories of electrochemical energy storage devices widely applied by far in commercial products are supercapacitors and batteries. Supercapacitors usually offer excellent power density characteristic thanks to the much faster kinetics of ion adsorption or redox reactions, and abundant ion adsorption sites enabled by large surface area of the most frequently applied highly porous activated carbons, yet at the expense of lower energy density, due to the limitation of reaction sites on the surface of electrodes rather than throughout the bulk. Conversely, batteries offer very high specific energy and energy density (energy stored per unit mass or volume of a device), but suffer from relatively short cycle life, low specific power and power density, due to the large volume change, mechanical failure of the electrode, sluggish kinetics of the redox reactions, low

conductivity of the active electrode material, passivation or detachment of the electrode material from the current collector, and other reasons.

In order to increase the specific capacity (and specific capacitance) of porous carbon electrodes, their surface can be functionalized to induce a reversible pseudocapacitive reactions as an additional charge storage mechanism[1-3]. At the same time, many functional groups are unstable and have adverse effects on the reliability of capacitors, causing self-discharge, leakage current, degradation and other negative contributions[2]. By far, no comprehensive understanding exists on the specific contributions of various functional groups to both the desirable and undesirable performance characteristics of double layer capacitors in various electrolytes. The successful formation of only stable (yet redox-active in organic electrolytes) functional groups on carbon has not been achieved in commercial devices and the feasibility of this concept is still unclear.

Gaining better understandings of the real role of oxygen-containing surface functionalization (which is one of the most common form of surface functionalization forms on carbon materials) enabled pseudocapacitance, and the effect of key parameters of carbon electrode and the electrolyte, including the carbon pore size, polarity of electrolyte solvent, and the acidity of electrolyte on the performance of carbon-based EDLCs will contribute to reasonable design of efficient energy storage devices. The first goal of this work is to systematically study the effects of carbon electrode structure, electrolyte recipe and electrode surface functionalizations on the capacitance, capacitance retention at high rates, and the self-discharge behavior of carbon-based EDLCs. Based on this knowledge, sulfur-containing activated carbon with high capacity and stable

capacitance retention is designed for optimized carbon based EDLCs. Besides, by harnessing the difference between the characteristic times required to establish a double layer and that of the pseudocapacitive redox reactions, a simple method to estimate the fraction of the pseudocapacitance is proposed.

On the other hand, in occasions where high energy density of the energy storage device is more important, Li-ion rechargeable battery is the better choice over supercapacitors. By now, conventional intercalation -type materials dominate as cathode materials for commercial Li-ion batteries, such as lithium cobalt oxide (LCO), lithium nickel manganese cobalt oxide (NMC), lithium nickel cobalt aluminum oxide (NCA) and other lithium transition metal oxides, is often limited by the low capacity and relatively low energy density of such cathodes[4-7]. The capacity of such electrodes is contributed by the lattice interstitials in the crystal, which can accommodate the Li ions. Because it usually takes at least one transition metal atom to build up such an interstitial, without a major change in the lattice structure during charge/discharge, the maximum theoretical capacity of such cathode structures would be limited to one electron transfer (one Li) per transition metal. Besides, distortion of local lattice structures happens frequently during charge-discharge cycling, which renders the influenced interstitial sites no longer available for Li-ion storage and results in irreversible capacity fading.

In recent years, researchers have developed conversion-type materials, majorly consisted of transition metal halides and chalcogenides, as a new category of cathode materials with much higher charge capacities than conventional cathode materials and reasonably high voltage. Unlike conventional intercalation-type cathode materials, the capacity of conversion-type materials is contributed by displacement reactions, in which

Li-ions replace the transition metal ions and results in the production of transition metal and lithium based compound as new phases. In this process, multiple electrons transfer is enabled per transition metal, which results in higher charge capacities. However, to achieve the practical application of conversion-type cathode materials, several challenges need to be addressed. Firstly, the large band gap of transition metal halides and chalcogenides leads to their poor electrical conductivities. Secondly, the vigorous phase change during the displacement reactions causes huge volume change, which would results in mechanical failure of the electrodes if not addressed properly. Thirdly, the metal nanoparticles produced from lithiation of conversion-type cathode materials may be easily passivated by the common carbonate based electrolytes applied for Li-ion batteries. To address these and other problems of conversion-type materials, hierarchical structured and highly conductive carbon nanostructure is the most straightforward solution. Systematic studies on the effect of carbon type, pore size and pore size distributions are necessary for the performance optimization of conversion-type cathode materials, and therefore the better solution of energy storage with higher capacity devices.

As the second goal of this work, I aim to study porous activated carbon material as conductive structural scaffold for conversion-type cathode based Li-ion batteries. The effect of carbon type, carbon pore size and pore size distributions on the performance of conversion-type cathode will be presented. Investigations will also be done on how the fundamental relationships between the carbon structure, active material - carbon composition, electrolyte salt concentration, electrolyte additives, and operating temperature affect the electrochemical reactions. Such studies will enable the optimized improvement of the capacity, capacity retention at high rates, and cycle life of

conversion-type cathode materials, taking FeF_2 as an example, which is a step closer to the commercial application of these materials.

CHAPTER 2

LITERATURE REVIEW

2.1 Highly porous carbon materials as electrode for EDLCs

2.1.1 Supercapacitors

On the basis of the differences in energy storage mechanisms, supercapacitors can be classified into two broad categories. One is the electrical double-layer capacitor (EDLC), in which the capacitance comes from the pure electrostatic charge accumulated across the so-called double layer at the electrode/electrolyte interface. The large surface area of the EDLC electrodes combined with a small thickness of the double layer results in a specific and volumetric capacitance two orders of magnitude larger than that of the electrolytic capacitors (Figure 2.1). The second category is a pseudocapacitor, in which fast and reversible Faradic (charge transfer) processes take place across the electrode/electrolyte interface. Quite often, these two mechanisms may function simultaneously in many supercapacitors. The energy density of supercapacitors is dependent on the capacitance of their electrodes and the maximum operating voltage. The latter is determined by the window of electrochemical stability of the electrolyte. Such stability windows, however, may be influenced by the surface chemistry and other properties of the supercapacitor electrodes as well as electrolyte purity. The energy of an EDLC could be estimated according to following equation:

$$E^{EDLC} = \left(\frac{C_- \cdot C_+}{C_- + C_+}\right) \cdot (V_{max}^{EDLC})^2$$

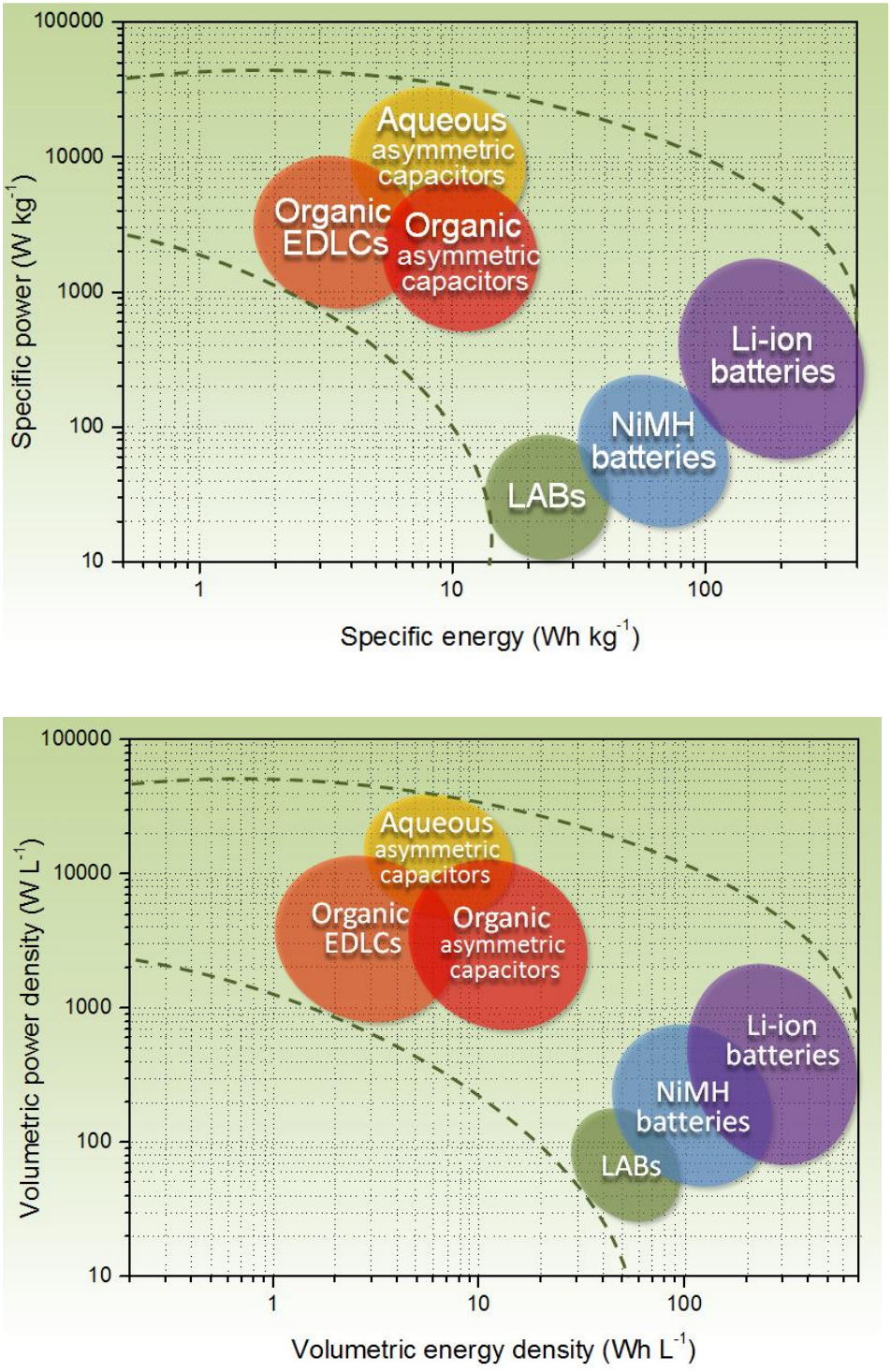

Figure 2.1 Schematic energy characteristics of various types of commercially available electrochemical capacitors in comparison with lead-acid, nickel metal hydride and Li-ion batteries as a simplified Ragone plot: (a) specific (mass-normalized) power vs. specific energy and (b) volumetric power vs. energy density.

where E is the energy, V_{max} is the maximum voltage difference between two electrodes, C_+ and C_- are the capacitances of the positive and negative electrodes, respectively. The energy of an EDLC is maximized when C_+ and C_- are identical:

$$E^{EDLC} = \frac{1}{2} C \cdot (V_{max}^{EDLC})^2$$

In a symmetric EDLC, the specific capacitance of each electrode (capacitance per unit mass of the electrode material) could be identified by a galvanostatic (constant current) charge–discharge test, where the specific capacitance is calculated using the following equation:

$$C = Idt/dV$$

where C is the specific (normalized by an electrode mass) capacitance, I is the specific current, and dV/dt is the changing rate of the voltage. In an ideal EDLC, the voltage slope, dV/dt, is constant for a fixed current. The calculation of a pseudocapacitance (or a total capacitance, which includes both pseudocapacitors and a double-layer capacitance) could be similar to that of a pure double-layer capacitance, in case when dv/dt stays constant, in spite of the additional Faradic reactions. If dv/dt varies with time, one may approximate the capacitance by using an average value of the voltage slope.

2.1.2 Highly porous activated carbon as electrode for supercapacitors

By now, high-surface-area carbon materials are utilized in EDLCs, with activated carbons (ACs) taking nearly all of the current market. The large specific surface area (SSA) of ACs, their relatively high chemical stability, somewhat reasonable cost,

abundance, and diversity of AC precursors, biocompatibility, scalable synthesis, and other useful properties make ACs the choice of the device manufacturers. ACs could be produced in various shapes and forms, such as powders and fibers of various size and pore size distributions, mats, monoliths, films, foils. Many raw materials, natural and artificial, have been utilized as precursors for AC synthesis. The pore size of ACs can be partially controllable by selecting particular precursor chemistry, activation method, and conditions. Still, commercial ACs for use in EDLCs suffer from some limitations, such as the presence of bottle neck pores, high resistance to ion diffusion and limited volumetric and gravimetric capacitance, to name a few.

2.1.3 Key parameters of porous carbon based EDLCs

The electrochemical performance of porous carbon based supercapacitors is dependent on several key parameters. Independent contributions of each factor could be challenging to separate, because most of these factors are strongly correlated. In this section, some of the most critical parameters that affect the performance of porous carbon based EDLCs are presented and discussed.

2.1.3.1 Pore size and pore size distribution

According to the simplified equation for the capacitance calculation,

$$C = \frac{\varepsilon_0 \varepsilon_r A}{d}$$

the specific capacitance provided by carbons should be proportional to their specific surface area (SSA), often approximated as Brunauer–Emmett–Teller (BET) SSA. This linear dependence was indeed suggested in early studies for small S_{BET} values[8,9], but

the capacitance was found to be almost constant for S_{BET} at 1200–3000 m^2 g^{-1}. To explain this nonlinear behavior, the complicated pore structures of activated carbons need to be carefully characterized for better understanding of their electrochemical performance. Activated carbons are highly porous materials with different types of pores, which are classified on the basis of their diameters: micropores (50 nm)[10]. Micropores play an essential role in the formation of electrical double layers. Shi[11] studied the relation between SSAs of microbeads and carbon fibers and their specific capacitances. It was suggested that the micropore surface is the most efficient in capacitance contribution (15–20 μF cm^{-2}), while capacitance from external (meso- and macropore) surface is dependent on the morphology of pores and surface functionalization. Since then, many works have confirmed the outstanding capacitive performance of micropores, especially ones with diameters < 1 nm[12,13]. Because electrolyte ions are generally shielded with solvent molecules, one may hypothesize that electrode pores that contribute capacitance should be at least larger than solvated ions. This theory was soon challenged by experimental observations[12]. It was reported that pores that are smaller than solvated ions could still contribute capacitance (Figure 2.2)[12]. In this case, the ion adsorption is realized by distortion of the solvation shell. This process provides a closer approach of the ion center to the electrode surface, which may result in anomalous increase in capacitance. The follow-up report applied solvent-free ionic liquid and revealed that the pore size leading to the maximum double-layer capacitance is very close to the ion size.

However, determination of the true SSA of porous activated carbon with irregular shape of pores, reduction of SSA during electrode processing, and the difference between the electrolyte ion accessible SSA and the SSA determined using gas sorption studies

may induce significant discrepancies. Some of the smallest micropores accessible by gas molecules may not be accessible by ions and thus may not contribute to double-layer capacitance. Similarly, ion intercalation might open some surface areas, which were previously inaccessible by gas molecules.

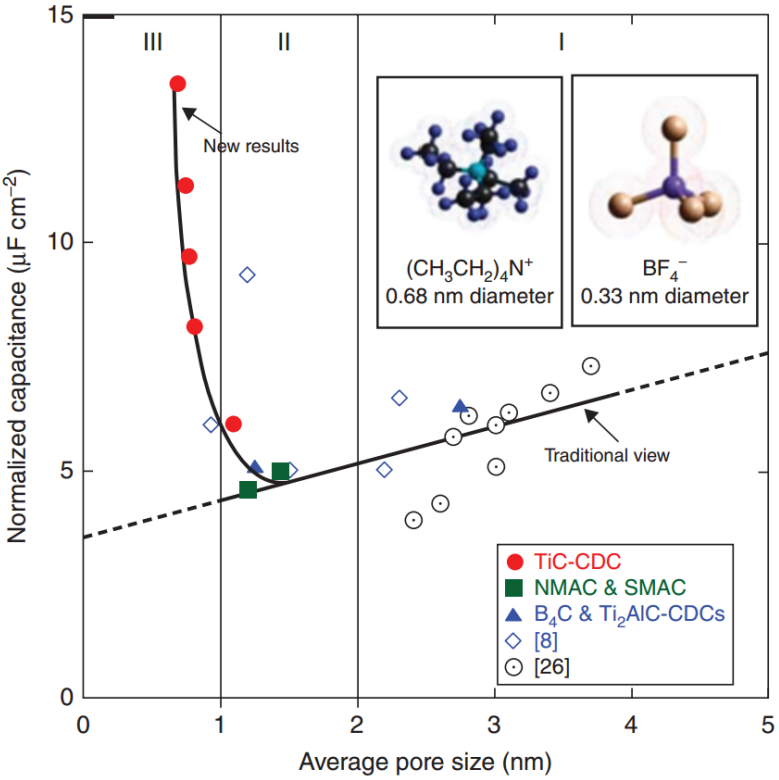

Figure 2.2 Carbon capacitance normalized by a BET specific surface area S_{BET} [12]. Anomalous capacitance increase happens when the pore size is reduced to less than 1 nm. (Reproduced with permission. Copyright © 2006 AAAS.)

The use of simplistic BET model may induce significant inaccuracies in SSA determination; and more advanced models for SSA and pore size distribution measurements are constantly being developed. For example, Ravikovitch and Neimark[14] developed a method for pore size distribution calculation on the basis of nonlocal density functional theory (NLDFT) of capillary condensation hysteresis in cylindrical pores. Chmiola et al. [13] compared the correlation of the specific capacitance of microporous

carbide-derived carbons (CDCs) with their SSAs calculated on the basis of both BET and NLDFT, respectively. The researchers found a better correlation between the specific capacitance and DFT (density functional theory) SSA (SSA_{DFT}) than between the specific capacitance and BET SSA (SSA_{BET}) (Figure 2.3). Compared to BET method, DFT method allows a further comparison of double-layer capacitance with ultra-small micropores (<1 nm). On the basis of the analysis of pore size distribution, they found that the specific double layer cpacitance of CDC is mostly dependent on the surface area of the pores < 2 nm (Figure 2.4).

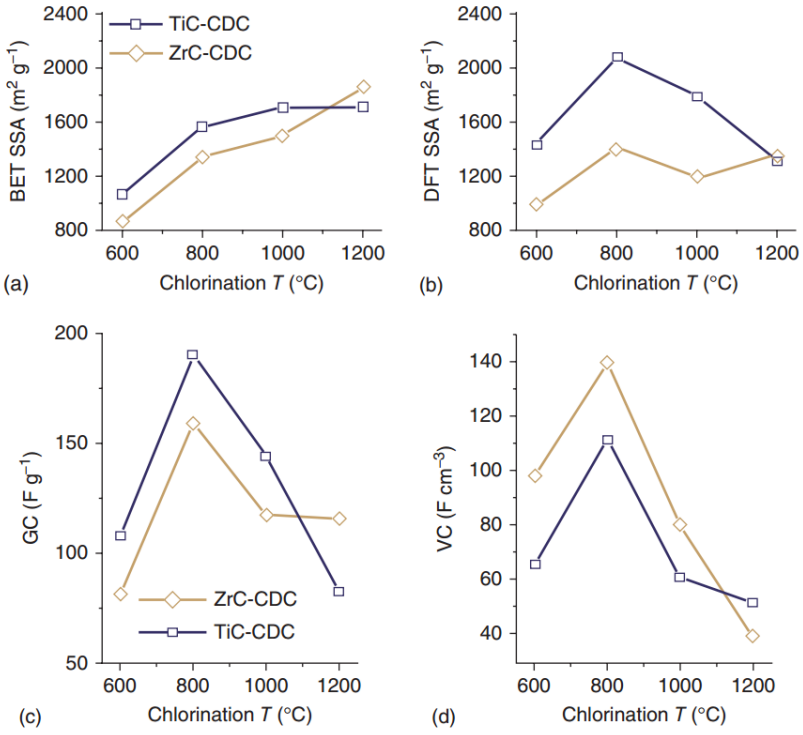

Figure 2.3 The evolution of (a) SSA_{BET}; (b) SSA_{DFT}; (c) gravimetric capacitance; and (d) volumetric capacitance of ZrC-CDC and TiC-CDC with chlorination temperature[13]. (Figure reproduced with permission. Copyright © 2006 Elsevier.)

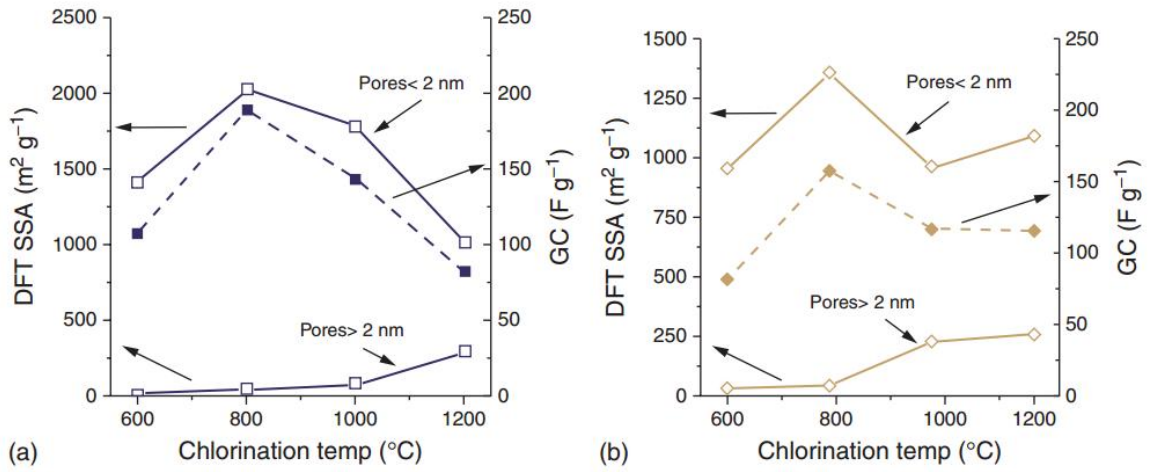

Figure 2.4 Micropore (2 nm) surface area in comparison with gravimetric specific capacitance for (a) TiC-CDC and (b) ZrC-CDC[13]. A direct correlation between the micropore surface area and specific capacitance is evident. (Figure reproduced with permission. Copyright © 2006 Elsevier.)

While micropores lead to a higher volumetric and gravimetric capacitance than mesopores, electrodes with only micropores may suffer from the slow ion transport and the resulting high ionic resistance even under moderate current densities. Conversely, mesopores allow smooth entry for electrolyte ions and therefore enhance the capacitance and the power density of devices[15-18]. Frackowiak et al. studied the coal-based ACs as electrode material for EDLC and found the optimized range of mesopore content within 20–50%[17]. This result, although still qualitative, shows that one needs to consider the balance in the pore size distribution of ACs for optimal EDLC performance in a given application. Chen et al. synthesized a series of micro- and mesoporous carbon materials with different SSA and pore size distribution by using different carbon sources and preparation methods. On the basis of the capacitive performance of these materials, they developed a general model for the estimation of capacitance, which is linearly proportional to "effective SSA," as determined by both the measured SSA and pore size distribution[19]. Further detailed models have been developed by taking pore curvature into

consideration. Meunier et al. developed separate models for the calculation of micropore, mesopore, and macropore capacitances, respectively[20].

2.1.3.2 Pore alignment

A recent study revealed the significant effect of pore alignment on the transport of ions within carbon nanopores[20]. In that work, zeolite-templated carbons were synthesized using low-pressure chemical vapor deposition (CVD). Identical micropore (Electrochemical impedance spectroscopy measurements and cyclic voltammetry studies showed up to three orders of magnitude enhancements in the ion transport and frequency response accompanying the micropore alignment and a decrease in the concentration of obstacles for ion diffusion. This finding proves that other than introduction of mesopores as conducting paths, designing porous activated carbons with straight pores and low concentration of defects might be an alternative strategy for achieving rapid ion diffusion within individual electrode particles. In response to the discovery of the essential role of pore alignment and optimization of pore size distribution for fast electrolyte diffusion and high power output of carbon EDLCs, researchers proposed various strategies to control the pore size and alignment of carbon-based electrode materials. In order to achieve a higher SSA and eliminate bottle-neck pores, while uniformly enlarging the smallest micropores produced in the course of carbonization of organic precursors, several promising routes were proposed. According to one method, an equilibrium content of oxygen-containing functional groups is uniformly formed on the porous carbon surface during room temperature treatment in acids[21]. These groups together with the carbon atoms are later removed via heat treatment at 900 °C. Repetition of the process of uniform formation of chemisorbed oxygen functional groups, and subsequently removing

them, allows for the uniform pore broadening needed to achieve the optimum pore size distribution[21]. In another study, an environmentally friendly low-temperature hydrothermal carbonization was utilized in order to introduce a network of uniformly distributed oxygen within the carbon structure in one step[22]. This material, produced from natural precursors (such as wood dust and potato starch), was then transformed into microporous carbons with high SSA of 2100–2450 m^2 g^{-1} via simultaneous heat treatment (and thus uniform removal of the oxygen-containing functional groups from the internal material surface) and opening of closed and bottle-neck pores by activation. A very high specific capacitance of 140–210 F g^{-1} was demonstrated in a TEATFB-based organic electrolyte[22]. Another efficient method for synthesis of carbons with controlled pore size distribution and alignment is the template method. In this method, highly ordered porous oxides, such as mesoporous silica are used as sacrificial template materials. Carbon precursors (sucrose solution, propylene, pitch, resin, etc.) are deposited inside the pores of the template and then carbonized. Then, the template is removed by dissolution in the hydrofluoric acid. The detailed discussion on highly ordered porous carbon is beyond the scope of this review, but readers are encouraged to refer to the representative works[23-27] on this important category of carbons.

2.1.3.3 Surface functionalizations

A variable amount of heteroatoms (oxygen, nitrogen, sulfur, etc.) can be added into the structure of carbon materials and functionalize their surfaces. Functionalized carbons can be synthesized by applying precursors containing heteroatoms[28-30] or posttreatment of carbons in heteroatom-enriched atmosphere[31,32]. The resulted functional groups can considerably enhance the gravimetric capacitance of electrodes by

contributing additional pseudocapacitance, which involves rapid charge transfer reactions between the electrolyte and the functional moieties. The usually denser functionalized carbons, although with smaller SSA, provide a higher volumetric capacitance than highly porous intrinsic activated carbons.

2.1.3.4 Electrical conductivity of the electrode

To achieve high power output, charge carriers must move quickly and smoothly through electrodes, which requires high electrical conductivity. The electrical conductivity of carbon-based electrodes strongly depends on the thermal treatment in the synthesis process, porous texture of the electrodes, and the content of heteroatoms[24]. Most carbon precursors are good insulators with a high content of σ- or sp^3- bonded carbon structures. During the thermal treatment at elevated temperatures, conductivity of the material is rapidly increased with the increasing content of sp^2-bonded conjugated carbon, because electrons associated with π-bonds are delocalized and become available as charge carriers[33]. The structural disorders and defects are healed to various extents, depending on the temperature applied for this process. Conductivity of carbon begins to increase at 600–700 °C, which corresponds to the range where loss of surface functionalities happens, until the formation of perfect crystalline graphite structure at over 2500 °C. Generally, higher porosity leads to poorer electrical conductivity because of higher content of insulating voids. To enhance the electrical conductivity of highly porous activated carbons, several strategies could be applied, such as adding conductive agents, high-pressure packing of activated carbon particles, and additional bonding network connecting particles. In the previous section, we have discussed the enhancement of the capacitive performance of porous carbon-based electrodes by surface

functionalization. However, the effect of surface functionalization on the electric conductivity of the carbon-based electrodes is largely negative. However, exceptions exist. For example, some functionalized carbons have higher density and, therefore, better electrical conductivity than porous intrinsic activated carbons[34]. Considering different categories of functionalities, oxygen functionalities, which preferentially form at the edge sites of graphite-like microcrystallites, increase the local barrier for electrons to transfer in between neighboring crystallite elements[35,36]. Conversely, nitrogen functionalities are often grafted on basal planes of graphite crystallites, with an increase in local free electrons. As a result, proper amount of nitrogen doping increases the electrical conductivity of carbons. However, previous works also reported aggravation of the capacitive performance of carbon materials from excess amount of nitrogen doping[37]. In summary, an optimized content of functionality is necessary for enhancement in capacitive performance of carbon-based supercapacitors.

2.1.3.5 Electrolyte selection

Electrolytes used in EDLCs may be divided into three classes: (i) aqueous (solutions of acids, bases, and salts), (ii) organic, and (iii) ionic liquids. Each electrolyte has been intensively studied and widely acknowledged for its pros and cons[38]. Ionic liquids are nonflammable, are nontoxic, and offer a higher operating voltage than their counterparts. Serious shortcomings of ionic liquids are their very high (often prohibitively high) current cost and relatively low ionic mobility at room temperature and below, which limits the charge/discharge rate of ionic liquid-based EDLCs. The advantages of using aqueous electrolytes include their very low cost, safety, and high ionic conductivity. Their disadvantages, however, include their low narrow

electrochemical window and corrosion of EDLC electrodes observed at higher temperatures and voltages (particularly for acid-based electrolytes, such as H_2SO_4 solutions), which limits the cycle life of the EDLCs and contributes to self-discharge. Organic electrolytes are somewhat in between aqueous ones and ILs in terms of the price, voltage, and charge–discharge time. Organic electrolyte-based EDLCs offer cycle life in excess of 500,000 and are used in the majority of commercial EDLCs. In addition, EDLCs with organic electrolytes are much less flammable than Li-ion batteries. Besides the selection of the electrolyte solvent, it is important to properly match the size of the electrolyte ions and the electrode pores of activated carbons. Aurbach et al. demonstrated that it was possible to selectively electroadsorb ions based on size[21,39,40]. They applied CVD of carbon on active porous carbon fibers to reduce the average pore size to 0.5–0.6 nm, which is in between the size of solvated monovalent (Na^+, ~0.4 nm) and bivalent cations (Ca^{2+}; Mg^{2+}, 0.6–0.7 nm) in the aqueous electrolytes applied. Electrodes with various average pore sizes were tested with different electrolytes in the three-electrode cyclic voltammograms (CVs). As a result (Figure 2.5), with $MgSO_4$ electrolyte, for larger pore sizes, which match the size of bivalent ions, rectangular shape of CV diagram was obtained; while for smaller pore sizes, negligible current was recorded in all potential ranges. Then, they replaced the cation and anion, respectively, with monovalent ions (Na^+ and Cl^-) and obtained asymmetric or even triangular CV diagrams, where the adsorption of much smaller monovalent ions contributes to much higher current than the opposite polarization. This result confirms the necessity of pores with proper size for the ion electroadsorption and insertion. Therefore, in manufacturing of carbon-based

supercapacitors, ion-sieving effect needs to be avoided for efficient access of electroadsorption sites to electrolyte ions.

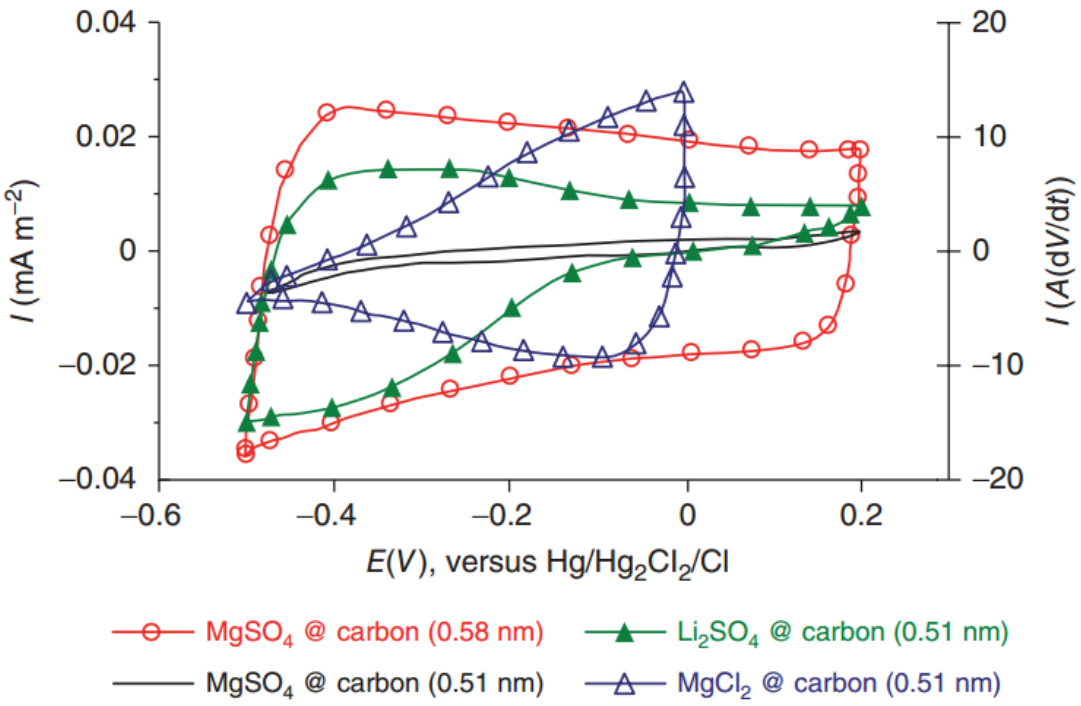

Figure 2.5 Cyclic voltammograms of activated carbon electrodes with an average pore size of 0.58 and 0.51 nm obtained in 0.1 M $MgSO_4$, Li_2SO_4, and $MgCl_2$ solutions[21,39,40]. The current is normalized by S_{BET}. (All data reproduced with permission[39]. Copyright © 2008 ACS Publications; [21]Copyright © 2006 Springer; [40]Copyright © 2009 ACS Publications.)

2.1.3.6 Self-discharge of porous carbon-based supercapacitors

For some of the supercapacitors applications, such as alternative and emergency power supply, long shelf-life and low self-discharge of supercapacitors are required. Unfortunately, activated carbon-based supercapacitors are prone to a gradual decrease in voltage during long-term storage. This spontaneous (thermodynamically favored) process is named "self-discharge" and is known to depend on the initial voltage, purity of carbon, and electrolyte as well as on electrolyte acidity. There are several possible reasons for

self-discharge. First, when the electrode is polarized to a potential that exceeds the electrochemical window of the electrolyte, the decomposition of the electrolyte happens at the electrode/electrolyte interface. This Faradic process reduces the cell potential continuously until the electrode potential falls into the electrochemical window of the electrolyte or the electrolyte is totally consumed. Besides, this process usually produces gases, which may block the pores of the electrodes and the separator and even induce a separation of individual particles within the electrode. This, in turn, may result in the capacitance fading (due to the reduction of accessible SSA of the electrodes) and in the reduction of power performance (due to the increased separator resistance). Second, some redoxactive impurities on the surface of the electrodes or in the electrolytes (such as O_2, H_2O, H_2O_2, metal ions, and others) may be involved in undesirable (parasitic) Faradic processes, which may consume the charge stored in an EDLC or lead to electrolyte degradation. Other than impurities, the intentionally grafted surface functionalities on carbon electrodes are also claimed to be responsible for the capacitance fading[9,41]. Although these surface functionalities contribute to pseudocapacitance, they are often thermodynamically unstable within the potential range and either readily decompose themselves or induce electrolyte decomposition, thus producing various gases (such as NO_2, SO_2, SO_3)[24]. Some researchers speculate that selected functional groups on carbon may possibly be stable in the operating potential range. Unfortunately, selective functionalization of carbon surface only with some particular functional groups is a challenging task. Furthermore, commonly available surface chemistry characterization tools (Fourier transform infrared spectroscopy (FTIR), X-ray photoelectron spectroscopy (XPS), chemical titration, etc.) have difficulties to unambiguously interpret the presence

of particular functional groups because the peaks corresponding to different groups are relatively broad and their position may be sufficiently close. Currently, no comprehensive understanding exists on the specific contributions of various functional groups to either the desirable or undesirable performance characteristics of EDLCs in various organic and aqueous electrolytes. So far, the feasibility of the concept to induce pseudocapacitance on carbon without penalties in leakage and degradation is unclear[42]. Successful formation of stable functional groups on carbon that do not induce leakage has not been achieved in commercial devices. Carbon electrodes utilized in commercial EDLCs are nonfunctionalized and purified to a high degree. Historically, improvements in the purification procedures allowed commercial devices to increase their cycle life from tens of thousands to several million cycles. In addition, such improvements in the purification of carbons and electrolytes allowed EDLC manufacturers to reduce the characteristic self-discharge time constant from a few hours to months (at room temperature). Finally, besides surface impurities and functionalities, self-discharge may also be attributed to Ohmic leakage from unintended interelectrode contacts or leaky bipolar electrodes. Several theories have been developed to distinguish the mechanism that causes self-discharge of a supercapacitor via electrochemical characterizations. According to Conway's model[43,44], self-discharge processes that follow different mechanisms would perform different potential fading rate. Other than this work, studies on proper modeling and simulation of self-discharge have been performed by many[45-48], including some supplement to Conway's model. For example, Kaus et al.[46] suggested that charge distribution at an open circuit may contribute to self-discharge.

2.2 Operation of Li-ion battery

Li-ion battery is a major category of electrochemical energy storage device, which achieves charge and discharge via lithium ions shuttling between positive and negative electrodes. Li-ion technology stems from primary batteries with metallic lithium negatives. To avoid the poor cycling characteristics and safety issues associated with metallic lithium as anode, Sony in 1990 announced the prototype of first Li-ion battery, which replaced metallic lithium with carbon anodes.

Conventional Li-ion battery contains cathode and anode on opposite sides of the device. The positive and negative materials usually have a layered structure to facilitate intercalation of Li ions. The net effect of the charge and discharge reaction is the movement of Li-ions back and forth between the electrodes, matched by a corresponding flow of electrons in the external circuit, which does work to the connected loadings. The Li ion and electron flows are driven by respective electrode voltages.

2.3 Various conventional cathode materials for Li-ion battery

As previously discussed, intercalation type cathode material is currently the most mature solution to commercial Li-ion batteries. An intercalation cathode is a solid host network, which stores Li ions in the interstitial sites of its crystal structure. In a Li-ion battery, Li ion is the guest ion and is inserted into and extracted from the host network of the cathode material during discharge/charge processes, respectively. These intercalation compounds can be divided into several crystal structures, such as layered, spinel, olivine and tavorite.

2.4 Highly porous carbon as conductive scaffold for transition metal fluoride cathode materials

2.4.1 Application of carbon materials as conductive additive to Li-ion battery electrodes

Due to the poor electric conductivity of many high capacity electrode materials, various forms of conductive carbon has been added in the electrode recipe to increase the conductivity of the electrodes. The most commonly applied conductive additive is carbon black particles with small particle size of ~10 nm[49-51]. The widespread application of carbon black as conductive additive is enabled by its facile and scalable production, easy dispersion in common solvents and facile adoption in electrode assembly process. However, because of the usually smaller size of carbon black additives compared to the active material particles, the carbon particles attach on the surface of active materials or independently agglomerate in the interstitials of active particles, which may results in unnecessary increase of the electrode. Besides, in cases where large volume change of the active material happens (such as Si as anode), the scattered carbon black particles cannot restrain the volume change or suppress the crack of the active material.

Besides the shortcomings mentioned above about carbon black particles as conductive additive, another essential limitation would be the fact that carbon black particles depend on unstable point-to-point contact to build up conductive paths for electron charge transfer throughout the electrode. Most of the commercial electrode materials are assembled into batteries by being casted on high density metal current collectors. To minimize the inactive dead weight contributed by the current collector, industries prefer thick electrodes and therefore large areal mass loadings of the electrode

for achievement of high energy density on the electrode level[52]. The requirement of thick electrode renders carbon black no longer qualified as conductive additive, due to the intermittent connection of the carbon particles throughout the thickness. To enable continuous, stable and mechanically flexible electronically conductive network throughout the thickness of the electrodes, 1-D and 2-D carbon nanomaterials, such as carbon nanotubes (CNTs) and graphene, have been applied as conductive additives. For example, Peng et al. applied CNT fibers as template for homogeneous deposition of MnO_2, which twisted around metal lithium bar to assemble micro-batteries[53] (Figure 2.6). Yushin et al. fabricated ultra-thick Si-based electrode via CVD deposition of silane on vertically aligned CNT array and post thermal treatment[52]. The aligned structure brings multiple benefits, including straight and aligned pores for rapid ion transport, high 1-D electrical conductivity for high stability and long cycle life, high structure uniformity, and the absence of polymeric and insulating binders.

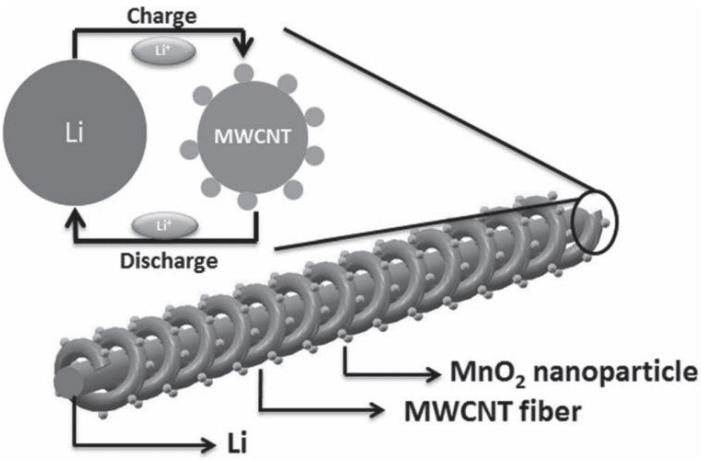

Figure 2.6 Schematic illustration to the wire-shaped lithium ion battery fabricated by twisting an aligned MWCNT/MnO_2 composite fiber and Li wire as positive and negative electrodes, respectively. The inserted top left image shows the charge-discharge process. Reproduced from Advanced Materials with permission.

Graphene has also been applied as carbon-based conductive additive, thanks to its large surface area and high conductivity. Dai et al. reported graphene-wrapped sulfur particles as cathode materials for lithium-sulfur batteries[54], in which graphene not only provides electron-conducting paths but also protects sulfur as active material from dissolving into the electrolyte and shuttle to the anode side in the form of polysulfide intermediates. Cheng et al. developed graphene-wrapped Fe_3O_4 anode material via in-situ reduction of iron hydroxide between graphene nanosheets[55]. Similarly, various common electrode materials such as $LiFePO_4$[56], Li_3VO_4[57], SnO_2[58] and Si[59], etc. have also been packaged with graphene nanosheets for higher reversibility, higher conductivity and longer cycle life.

Despite of the benefits brought along by nanostructured 1-D and 2-D nanocarbons, there are several challenging issues about practical adoption of these materials. First, due to the strong Van de Waals force at the interface of neighboring CNTs or graphene nanosheets, these materials are difficult to be dispersed homogeneously in polar solvents. The addition of surfactants may relieve this pain, but it would also introduce extra impurities to the electrode which may lead to unpredictable behaviors. Surface functionalization of these materials with polar functional groups such as hydroxyl, carboxyl and carbonyl groups is another viable way. However, the extent of functionalization needs to be strictly monitored, because heavy functionalization may deteriorate the conductive conjugated sp^2 arrangement of carbon atoms and lead to degradation of the conductivity of electrode. Furthermore, it may result in undesired redox reactions at the vicinity of electrode/electrolyte interface, which contributes to leakage current. Second, except for synthesized core-shell structures, without chemical

bonds between nanostructured carbon and active materials, the active materials tend to detach from the carbon scaffold when in direct contact with liquid electrolyte during battery operation.

Chemical vapor deposition (CVD) of homogeneous carbon coating on active electrode materials is also an effective solution to introduction of conductive additives. Pyrolysis of carbon sources such as acetylene, methanol, toluene, isopropyl alcohol etc. is enabled at elevated temperatures (400-1000 ℃), which produces carbon deposition on the surface of active electrode materials (Figure 2.7). The advantage of conductive carbon coating compared to carbon black particles is its intimate face-to-face contact with the active materials, which guarantees efficient charge transfer. Besides, researchers found considerable mechanical strength of well-prepared carbon coatings which sustain the large strain caused by the volume change of the active materials packaged inside. For example, Liu et al. synthesized Si/C composite via pyrolysis of pitch[60]. Cui et al. developed a yolk-shell design of Si/C nanocomposite[61]. This unique structure brings high capacity, long cycle life and high Coulombic efficiency of the electrode. Pristine Si nanoparticles are included in carbon shells with bigger size. The free space serves as buffer zone to accommodate the volume increase of Si particles during lithiation. Yushin et al. synthesized porous particles containing large internal porosity, with hierarchical structure of Si/C nanocomposite via Si CVD deposition on annealed carbon black scaffold followed by CVD carbon coating[62]. Large Si volume changes are accommodated by the particle's internal porosity.

Like other forms of carbon additives, carbon CVD also has its own limitations. First, carbon CVD needs to be operated at high temperatures (commonly >400 ℃), which

is not compatible with active materials that melt or decompose at lower temperatures. Carbon depositions obtained from low temperatures (<300 ℃) are consisted of complicated compositions, including various stages aromatic intermediates and polymeric substances. The conductivity of the resulted carbon deposition is also not satisfying as electron conducting paths for the electrodes. Second, instead of homogeneous carbon coatings, carbon CVD may result in growth of carbon fibers or nanotubes on catalytic sites, such as on the surface of transition metal and metal oxides.

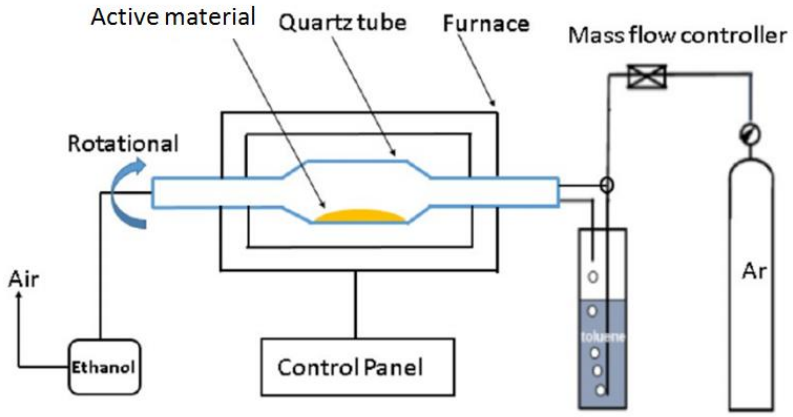

Figure 2.7 Schematics of typical CVD system for carbon coating on active electrode materials. Reproduced with the permission of Electrochemical Acta.

2.4.2 Conversion type cathode materials for Li-ion battery

Conversion reaction depicts a process in which lithium replaces transition metal ions from transition metal based compounds (oxides, sulfides, fluorides, etc.), producing elementary transition metal phase and the corresponding lithium salt (Figure 2.8), generalized as the following reversible reaction[63]:

$$M_aX_b + (b \cdot n)Li = aM + bLi_nX$$

where M = transition metal, X = anion (commonly O, S and F), and n = formal oxidation state of X.

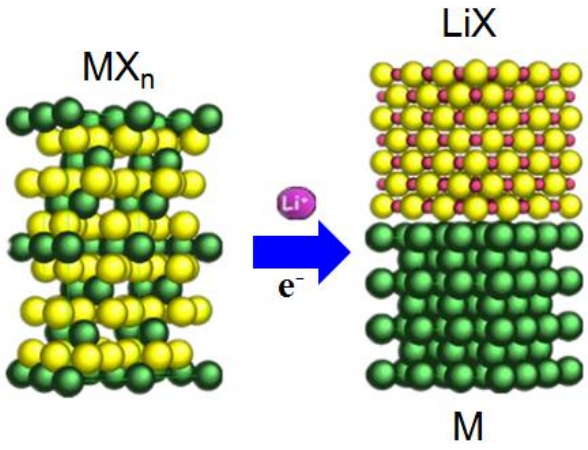

Figure 2.8 Schematic of the mechanism of a typical conversion reaction.

Because of poor conductivity, lacking of crystal interstitials for Li-ion intercalation, and poorer reversibility compared to conventional intercalation compounds, conversion type materials was not considered as practical candidates for cathode materials. These materials was then re-considered as promising alternatives in rechargeable batteries, after Tarascon et al. demonstrated that several transition metal oxides, including Co_3O_4, CoO, NiO and FeO, can exhibit high specific capacities and good cycle life[64,65]. Since then, a large category of new cathode candidates has been scrutinized, which majorly falls in the structure of binary M-X compounds with X = O, N, F, S, and P.

The theoretical cell voltage, or electromotive force (emf) of conversion reactions can be calculated from the Nernst equation as following:

$$\Delta G = n \cdot \Delta G_f \left(LiX_{\frac{m}{n}} \right) - \Delta G_f (MX_m) = -nFE$$

where n = formal oxidation state of M, n/m = formal oxidation state of X, E = emf of conversion reaction.

The theoretical cell voltages and gravimetric capacities of representative conversion-type materials are listed in tables 2.1 and 2.2, respectively:

Table 2.1 Theoretical cell voltages of conversion type materials vs. Li/Li^+

Material	Emf (V)	Material	Emf (V)	Material	Emf (V)
TiF_3	1.396	TiO_2	0.608	TiS_2	1.233
VF_3	1.863	V_2O_3	0.945		
MnF_3	2.647	Mn_2O_3	1.431	MnS	1.144
FeF_3	2.742	Fe_2O_3	1.631	FeS_2	1.861
CoF_2	2.854	CoO	1.802	CoS_2	1.898
NiF_2	2.964	NiO	1.954		
CuF_2	3.553	CuO	2.248	CuS	1.998

Table 2.2 Theoretical gravimetric capacity of conversion type materials

Material	Capacity (mAh g^{-1})	Material	Capacity (mAh g^{-1})	Material	Capacity (mAh g^{-1})
TiF_3	767	TiO_2	1342	TiS_2	957
VF_3	745	V_2O_3	1073		
MnF_3	719	Mn_2O_3	1018	MnS	616
FeF_3	712	Fe_2O_3	1007	FeS_2	893
NiF_2	554	CoO	715	CoS_2	871
CuF_2	528	NiO	718		
CoF_3	694	CuO	674	CuS	561

A parallel comparison of the theoretical cell voltage of transition metal fluorides, oxides and sulfides reveals that, due to the stronger electronegativity of fluorine, fluoride based conversion materials have higher theoretical cell voltage compared to oxides and sulfides counterparts. Actually, fluoride based materials are the most popular category of conversion type materials as cathode for Li-ion batteries. Meanwhile, due to the proper low emf, some of the transition metal oxides are also exploited as anode materials.

A comparison between the experimental cell voltages and the gravimetric capacities of conventional intercalation-type materials and conversion-type materials reveals that, although intercalation-type materials take advantage of higher theoretical voltage, the higher gravimetric capacity of conversion-type materials make up for the difference in voltage, which leads to similar gravimetric energy of these two categories of materials[4] (Figure 2.9). However, there are still more reasons to seriously consider the application of conversion-type cathode materials as alternative to the intercalation-type ones. First, the much higher mass density of conversion-type materials enables them with higher volumetric energy densities, which is important for space confined applications such as aerospace, portable electronics, etc. Second, the market price of some of the conversion type materials is also much lower than the well exploited intercalation compounds, which would bring down the cost of batteries. Third, some of the intercalation-type cathodes have been reported to be toxic, while most of the conversion-type materials are stable, safe and environmentally-friendly.

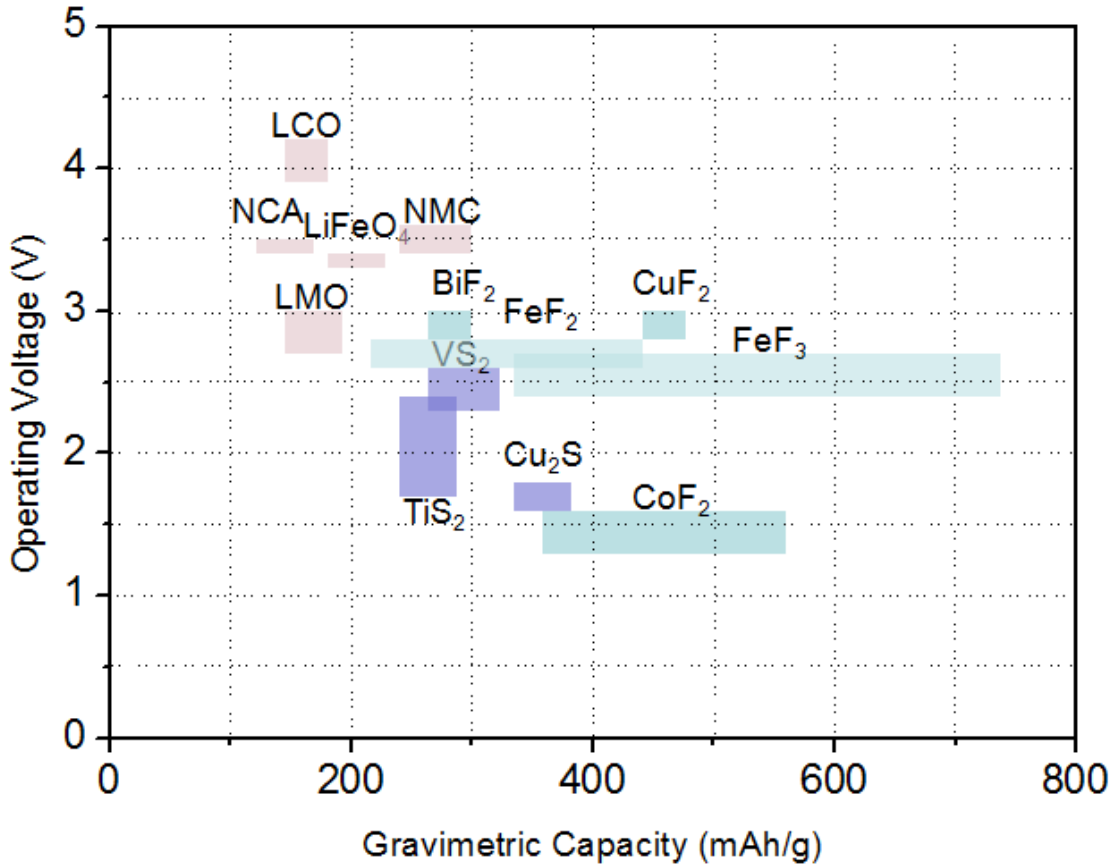

Figure 2.9 Experimental gravimetric capacity and operating voltage of representative intercalation-type cathode materials and conversion-type cathode materials. Some of the data included in the diagram reproduced[4] with the permission of *Chemistry of Materials*.

2.4.3 Transition metal fluoride materials as cathode

The first trial of applying transition metal fluoride as cathode for Li-ion battery dates back to 1997, when Arai et al. reported a capacity of 80 mAh g^{-1} from FeF_3 in the voltage rang of 2-4.5 V, taking advantage of the Fe^{3+} to Fe^{2+} redox transition[66]. The poor electronic conductivity due to the large bandgap of metal fluorides and the questionable ionic conductivity results in the disparity between the experimental specific capacity of 80 mAh g^{-1} and the theoretical value of 237 mAh g^{-1}. Since then, transition metal

fluorides have been long ignored as cathode materials for Li-ion batteries. In 2002, Amatucci et al. reconsidered the application of FeF_3 by solving the poor electronic conductivity issue via reducing the size of FeF_3 particles and addition of conductive carbon[67]. They claimed the improved reversibility and conductivity of the electrode was attributed to the fact that nanosized crystals have a high total material volume on the surface, which contains a number of defects which can contribute substantially to enhanced electronic and ionic activity. Besides, the nanosized FeF_3 grains were critically connected with highly conductive carbons. Within the voltage range of 2-4.5V, Amatucci et al. obtained a higher capacity of ~200 mAh g^{-1} under heavily modified conditions of 70 ℃ and 7.58 mA g^{-1}. The smaller discrepancy between experimental capacity and the theoretical value (237 mAh g^{-1} for single electron transfer at 2-4.5V) confirmed the possibility of applying fluoride based cathodes with kinetics properly enhanced. Even higher capacity of 660 mAh g^{-1} was obtained when expanding the voltage window to 1.5-4.5V, which included both the conversion reactions from Fe^{3+} to Fe^{2+} and from Fe^{2+} to Fe^0. However, the cycling test result was not presented. In the followed-up research, the same group presented preliminary data of other types of fluoride materials, including FeF_2, NiF_2 and CoF_2[68]. The comparison between the voltage profile of FeF_3 and FeF_2 revealed that after the first charge-discharge cycle, the material was not fully reconverted back to Fe^{3+}; instead, after the first cycle, the cycling profile of FeF_3 was quite similar to that of FeF_2, indicating a stable intermediate phase of Fe^{2+}. Following the works of Amatucci et al., many researchers have further developed novel synthesis of FeF_3 or FeF_2 phases and studied the mechanism of FeF_3 and FeF_2 based conversion reactions. FeF_3 and FeF_2 thin films have been synthesized by pulsed laser deposition[69], molecular beam

epitaxy[70], oxidation/fluorination of Fe surface[71,72], etc. Kang et al. synthesized FeF_3 nanoflowers hybridized with CNTs for enhanced cycle life at the voltage range of 2-4.5V[73], which achieved decent capacity of 150 mAh g^{-1} at high current densities of 500 mA g^{-1}. Jin et al. synthesized interwoven FeF_3 nanowires as cathode materials for Li-ion batteries. Under TEM characterization, interconnected Fe nanodomains were observed in fully lithiated FeF_3 nanowires, which were believed to provide the electron conducting paths throughout the FeF_3 based electrode.

Besides FeF_3 and FeF_2 as the most intensively studied fluoride based cathode materials, researchers also studied other fluoride materials, such as CoF_2[74], NiF_2[75-77], BiF_3[78,79] and CuF_2[80], with the attempt of higher operating voltage or higher charge capacity. Specifically, the validation of CuF_2 is of great interest, because of its much higher operating voltage at roughly 3.5V compared to other fluoride based materials, the experimentally observed operating voltages of which lie in the low range of 2-2.5V. However, experimental results showed that without specific structural design, CuF_2 based electrode can only last for the first several cycles. To explain this unexpected failed performance of CuF_2, Graetz et al. compared the nanostructure of lithiated FeF_2 and CuF_2 under high resolution TEM[81]. As the result, interconnected Fe nanodomains were found throughout the lithiated FeF_2 particles, which accorded well with the findings of other works. In contrast, Cu metal particles produced from the lithiation of CuF_2 were found to agglomerate into a larger domain, clearly separated from the insulating LiF phase. They therefore concluded that the irreversible performance of CuF_2 stems from the lack of local electron transport paths through the insulating LiF phase. To solve this problem, researchers are working on various possible surface coatings on nanosized CuF_2 particles

for suppression of phase separation of CuF_2 upon lithiation. Another strategy is the doping of Fe into CuF_2 phase, which can serve as extra electron conductive paths during electrode lithiation, while the material still enjoys the high operating voltage contributed by the conversion reaction from Cu^{2+} to Cu^0 (Figure 2.10)[82].

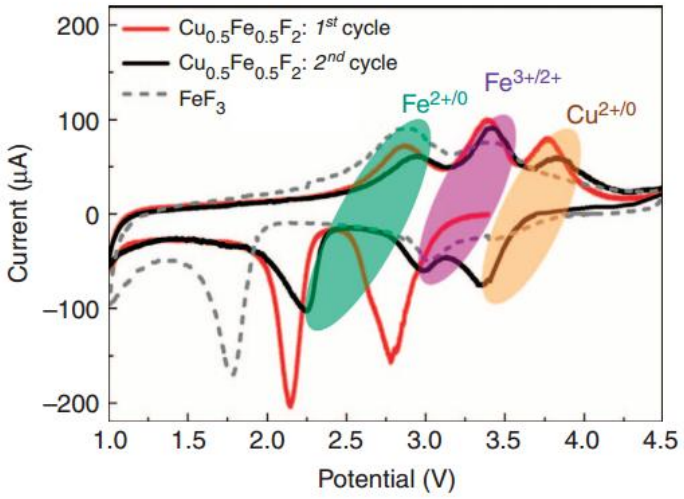

Figure 2.10 Cyclic voltammetry (CV) curves for the first (red) and second (black) cycles at a rate of C/40, in comparison to that of FeF_3.

Besides direct exploitation of transition metal fluorides as cathode materials for Li-ion batteries, researchers also proposed the application of LiF and elementary metal mixture as alternative cathode with similar operating mechanism. The studies on this type of composite started with the work of Amatucci et al., which demonstrated that Li could be extracted from LiF/Bi/C nanocomposites and subsequently reinserted. Since then, Fichtner et al. reported the synthesis of Co/LiF/C nanocomposite and its application as cathode in lithium-ion batteries[83]. The nanocomposite was synthesized by pyrolysis of cobaltocene/LiF mixture at 700 ℃ in Ar flow. Fu et al. reported the synthesis of Co/LiF[84] and Ni/LiF[85] nanocomposites via pulsed laser deposition, but obtained limited capacity

compared to the theoretical values. Liao et al. prepared Ni/LiF by combinatorial sputtering, which enhanced the capacity and reversibility of this composite[86].

2.4.4 The reason for the poor reversibility of transition metal fluoride cathodes

There are manifold reasons for the poor reversibility of transition metal fluoride cathodes. First, the low conductivity of these materials results in inefficient electron transfer and therefore low usage of the materials. Second, as illustrated previously in the case of CuF_2 phase separation of transition metal phase and LiF phase leads to incomplete re-conversion and therefore capacity fading. Third, as some researchers claimed, with the existence of acidic matters arise from impurities in the electrolyte, metals from metal fluoride lithiation products could be dissolved into the electrolyte and shuttled to the anode surface[87]. Last but not least, surface passivation of metal nanoparticles from decomposition of electrolyte solvents has been reported[88,89]. The insulating polymeric depositions on the surface of metal nanoparticles have prevent them from re-conversion reactions.

CHAPTER 3

HIGHLY POROUS CARBONS AS ELECTRODES IN LITHIUM ION CAPACITORS

3.1 Introduction & Motivation

In Chapter 2, we have reviewed the previous works on application of highly porous carbon as electrode material for EDLCs. The advantages of using porous carbon electrodes in conjunction with a double layer energy storage mechanism include very high charge–discharge rates performance in combination with ultra-long electrode cycle life, which may exceed 500,000 cycles [90]. Indeed, the adsorption/desorption of ions on the electrode–electrolyte interface does not require diffusion through a solid phase, and is not accompanied with any destruction of the electrode structure. Not surprisingly, the use of porous carbon cathodes in Li-ion batteries (or, more conventionally speaking, in asymmetric Li-ion electrochemical capacitors) have been proposed[91,92]. The serious limitation of this technology, however, is significantly lower gravimetric and volumetric capacity compared with traditional metal oxide based cathodes. In order to increase the specific capacity (and specific capacitance) of porous carbon electrodes, their surface can be functionalized to induce a reversible pseudocapacitive reactions as an additional charge storage mechanism[1,3]. At the same time, many functional groups are unstable and

have adverse effects on the reliability of capacitors, causing self-discharge, leakage current, degradation and other negative contributions[24]. Unfortunately no comprehensive understanding exists on the specific contributions of various functional groups to both the desirable and undesirable performance characteristics of double layer capacitors in various electrolytes. The successful formation of only stable (yet redox-active in organic electrolytes) functional groups on carbon has not been achieved in commercial devices and the feasibility of this concept is still unclear.

In this study I aim to form an independent opinion on the potential of functionalized carbon electrodes to replace traditional oxide-based cathodes in Li-ion batteries. I am also interested to reveal the impact of the specific surface area and pore size distribution of porous carbon electrodes on their Li ion storage ability. Finally, I aimed to reveal if capacitance similar or higher than what was observed in[93,94] (in a similar configuration vs. a Li foil counter electrode and in similar electrolytes) could be achieved in functionalized porous carbon electrodes having significantly higher thickness (>150 μm) and mass loadings (44 ± 8 mg cm^2), which would be more comparable to that observed in commercial devices and which could be measured more precisely.

3.2 Materials & Methods

In contrast to the previous studies on CNTs[93,94], nanodiamond (ND) soot – derived carbon nanoparticles and micro-/mesoporous activated carbon have been selected as model materials for this project. The selected samples can be processed into thick uniform electrodes easier than CNTs. ND soot was supplied by NanoBlox, Inc., USA (UD50 grade). ND soot contains nanodiamond powder, disordered carbon, carbon onions

and graphitic layers on the surface of the diamond nanoparticles. Its microstructure has been explicitly characterized in previous publications[95-97]. Carbon onions with little (if any) functional groups on their surface were obtained by annealing as-received ND soot at 1800 ℃ for 2 h under Ar atmosphere. A portion of the carbon onion sample was then treated for 1 h in a concentrated solution of sulfuric and nitric acids (H_2SO_4/HNO_3, 3:1 v/v, 96% and 70%, respectively) at 80 ℃ to prepare surface oxidized carbon onions (noted as ox-onions in the following discussions). Such processing allowed us to better elucidate the role of functional groups in enhancing the capacitance of carbon-based electrodes. It could be noted that ND soot is produced on a large scale by a controlled detonation of carbon-containing explosives[95]. Selective oxidation of sp^2 carbon in detonation ND soot by treatments with acids[95] or annealing in an oxygen-containing gaseous environment[97,98] allows for the fabrication of high sp^3-content ND powder. Annealing of ND powder in an inert atmosphere at temperatures around 1800 C leads to their graphitization and formation of carbon onion-like structures[95,96,99,100]. Due to their high surface area, good mechanical properties, low cost and relatively high conductivity of as-produced ND soot and carbon onions, they offer attractive properties for energy storage applications, such as electrochemical capacitors[95,96,99,101]. The specific capacitance of ND is lower than that of micro-/mesoporous carbons due to the higher specific surface area of the later. Therefore, commercially available mesoporous activated carbon supplied by CECA (Arkema Group, grade 4S) was used as a benchmark material for this study. The morphology of all the samples were characterized using a scanning electron microscope (SEM) (LEO, Germany). The ND soot and carbon onion samples were additionally studied under a transmission electron microscope (TEM) (JEOL,

Japan). Energy-dispersive X-ray spectra (EDS) was performed to characterize the chemical composition. X-ray photoemission spectroscopy (XPS) measurements were performed with Thermo K-Alpha XPS instrument to analyze the surface chemistry of the materials involved in this study. Curve fitting of the photoemission spectra was performed following a Smart-type background subtraction. C 1s peak contributed from sp^2 hybridized carbons at 284.5 eV was set as a reference. All other peaks were fitted by the Gaussian– Lorentzian function. Nitrogen sorption–desorption isotherms have been collected at 77 K using a Tristar porosimeter (Micromeritics, USA) in order to determine the surface area and pore size distribution of the samples. The BET surface area was calculated from the isotherms in the range from 0.02 to 0.3 of relative pressures (P/P_0). All electrochemical measurements performed in this study were assembled in two-electrode coin cells with a diameter of 3/4 inch in a glove box with a water content < 1ppm (Innovative Technologies, USA). Lithium foil (Alfa Aesar, USA) was used as a counter & reference electrode in all the cells. Carbon coated aluminum current collectors were used as current collector. The following electrolyte solutions have been selected for the study – 1 M lithium hexafluorophosphate ($LiPF_6$) in a 1:1:1 mixture of dimethyl carbonate (DMC), diethyl carbonate (DEC) and ethylene carbonate (EC) and 1 M $LiPF_6$ in a propylene carbonate (PC) solution(battery grade, Novolyte, USA). In order to prevent the blockage of the electrochemically active surface area by the electrode binder solution observed previously[94] we have avoided the use of a more traditional carboxymethyl cellulose (CMC) and Polyvinylidene fluoride (PVDF) binder solutions. Instead we used a suspension of the Polytetrafluoroethylene (PTFE) (Aldrich, 60 wt.% in water) as a fibrous binder that is known not to block the inner surface area of the porous

particles. The total amount of the binder in electrodes was kept at 10 wt.%. The thickness of the electrodes made was controlled within a narrow range (150–200 μm). Two kinds of porous separators, Celgard 2325 (from Celgard) and glass microfiber (from Whatman), were used to isolate the electrodes for DMC/ DEC/EC and PC solutions, respectively. The glass microfiber is more hydrophilic than commercial separators and can be wetted by PC more easily. Cyclic voltammetry measurements were performed using a 1250 Galvanostat/Potentiostat (Solartron Instruments, USA) at different constant scan rate (1–100 mV s^{-1}) between 1.5 and 4.5 V vs Li/Li^{+} . The capacitance was deduced from the loop area by the relation $C = A/(2\Delta V)$, where C is the cell capacitance, A is the loop area and ΔV the potential window. In this approximation the capacitance of the Li foil is considered to be significantly larger than that of the carbon within the scan rate range investigated.

Charge–discharge measurements were performed using a SCTS supercapacitor testing system (Arbin Instruments, USA) in the range of constant current densities (50–2000mA g^{-1}) between 1.5 and 4.5V. The capacitance was deduced from the charge–discharge curves by the relation C = I/ (dV/dt), where C is the cell capacitance, I is the current, dV/dt is the average slope of the discharge curve.

3.3 Results & Discussion

The SEM images in Figure 3.1 show the morphology of the electrodes made from the test materials and the high resolution images of the carbon particles. The morphology of the ND soot and carbon onion – based electrodes is very similar. The majority of individual particles are less than 10 nm and the pores between the closely arranged

nanoparticles are commonly less than 100 nm, with the majority of visible pores being smaller than 15 nm (Figure 3.1a and b). This result shows that the thermal and chemical oxidation treatments of ND soot do not cause a significant change in either the particle or electrode morphology. The SEM analysis of an activated carbon sample showed a broad particle size distribution, from as little as less than 1 micron to over 30 micron in characteristic dimensions. In addition, nanoparticles were observed on the rough surface of the micron-size particles (Figure 3.1d). The previously studied and presented[99] differences in the structures of ND soot and carbon onion are illustrated in TEM micrographs (Figure 3.2). At low resolution, both samples are composed of 4–10 nm particles (Figure 3.2a), but at high resolution the major difference become apparent (Figure 3.2b and c). Electrically conductive ND soot is composed contains sp^3 diamond core particles (0.205 nm distance between the (1 1 1) planes), coated either with sp^2 amorphous carbon or graphitic shells, having an interlayer spacing of 0.34 nm (Figure 3.2b). High temperature annealing of either the ND soot or the purified ND particles leads to the formation of nanocarbon onion-like powders with highly ordered graphitic walls and no residual sp^3 carbons (Figure 3.2c). The low concentration of defects in carbon onion walls was evident in the high resolution TEM micrographs. Nitrogen sorption measurements (Figure 3.3a) were taken to analyze the specific surface area (SSA) and pore size distribution of the samples. All investigated samples exhibit type-IV isotherms with a characteristic hysteresis between the adsorption and desorption graphs, characteristic for the samples containing mesopores. The total BET (Brunauer Emmett Teller) SSA of the nanoparticle samples was found to range from 400 $m^2\ g^{-1}$ for carbon onions (annealed ND) to 600 $m^2\ g^{-1}$ for ND soot and oxidized carbon onions, which is

still nearly twice smaller than that of the activated carbon sample (Table 3.1). Noticeably smaller SSA of carbon onions may be related to both the regular graphitic structure and low concentration of defects (pores) on their surface and closing some of the pores during the high temperature graphitization process.

The shape of the isotherms provides us insights about the porosity of the samples. The height of the plateaus observed at low (<0.1) relative pressures indicates the relative volume of the micropores (Figure 3.3a). Therefore, one would expect the smallest volume of micropores in a carbon onion sample and the largest volume in an activated carbon. The rapid increase in the sorption curves near the hysteresis region (relative pressure>0.5) is indicative of the volume of mesopores. Indeed, according to non-local density functional theory (NLDFT) calculations (Figure 3.3b), the ND soot exhibits the largest volume of mesopores and the largest average mesopore size (~9 nm). The activated carbon sample shows the lowest volume of mesopores and the smallest average size of mesopores (~4.5 nm). This sample, however, has the highest volume of micropores.

XPS measurements were applied to reveal the existence of oxygen containing functional groups on the surface of carbon particles. A special powder-friendly sample holder was utilized in these measurements. The survey spectra of all the samples (Figure 3.4a) show the presence of a strong O 1s peak in all the samples except the as-produced carbon onions. This peak was attributed largely to the presence of oxygen containing functional groups on the particles. The O peak was absent in the spectra of carbon onions, which indicates the thorough removal of oxygen containing functional groups during the annealing process. According to the performed semi-quanitative analysis, the acid

treatment introduced over 16 at.% of O onto the surface of carbon onions via formation of various functional groups (Figure 3.4a).

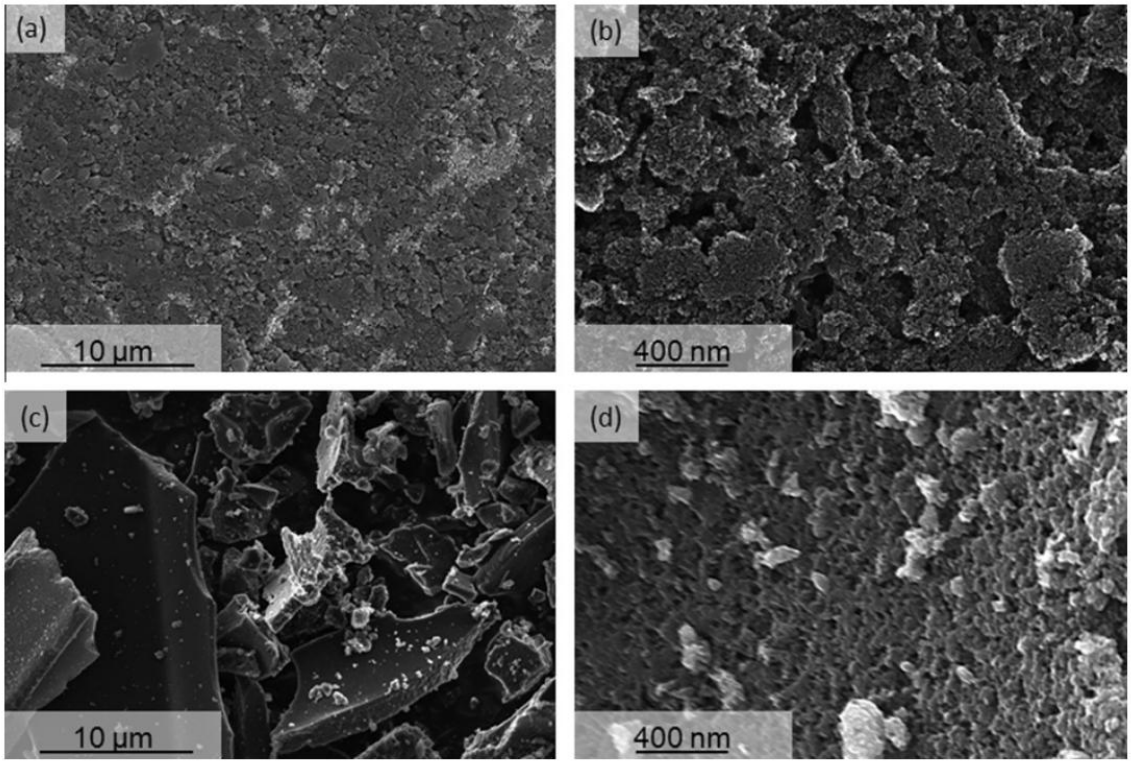

Figure 3.1 SEM images of ND soot (a and b) and 4S activated carbon (c and d).

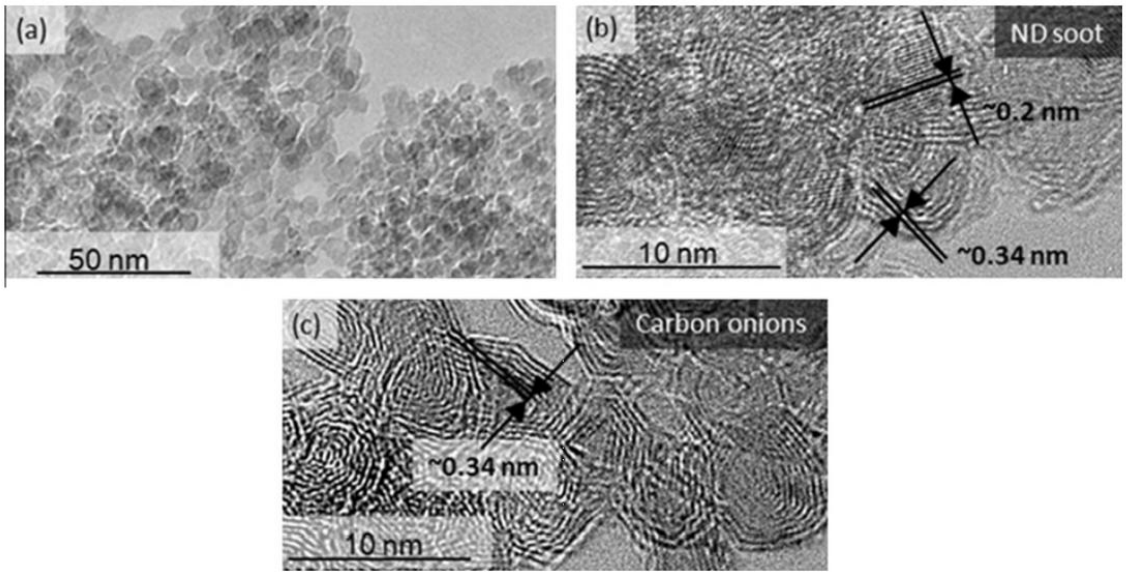

Figure 3.2 Low-mag (a) and high-mag TEM images of ND soot (b) and carbon onions (c).

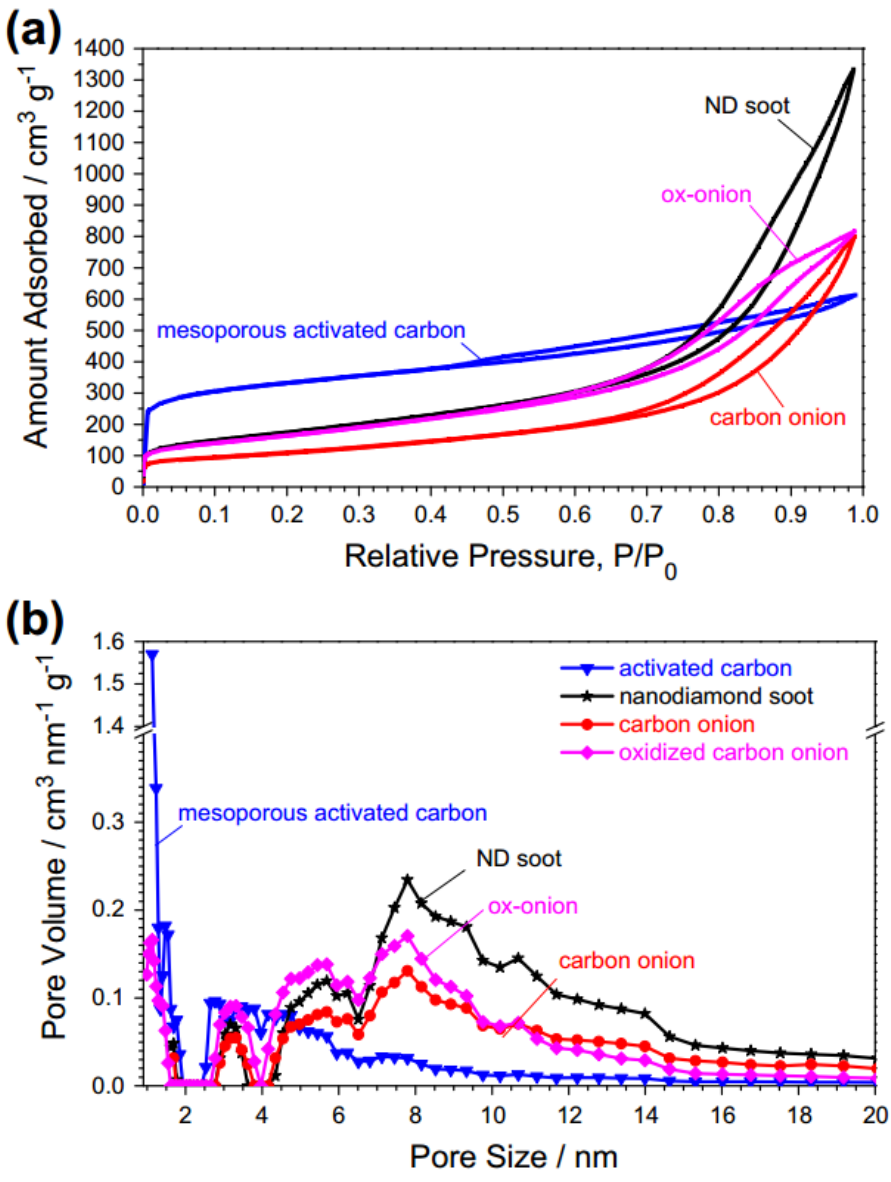

Figure 3.3 Isotherm curves and pore size distribution of ND soot, carbon onion, oxidized carbon onion and mesoporous activated carbon.

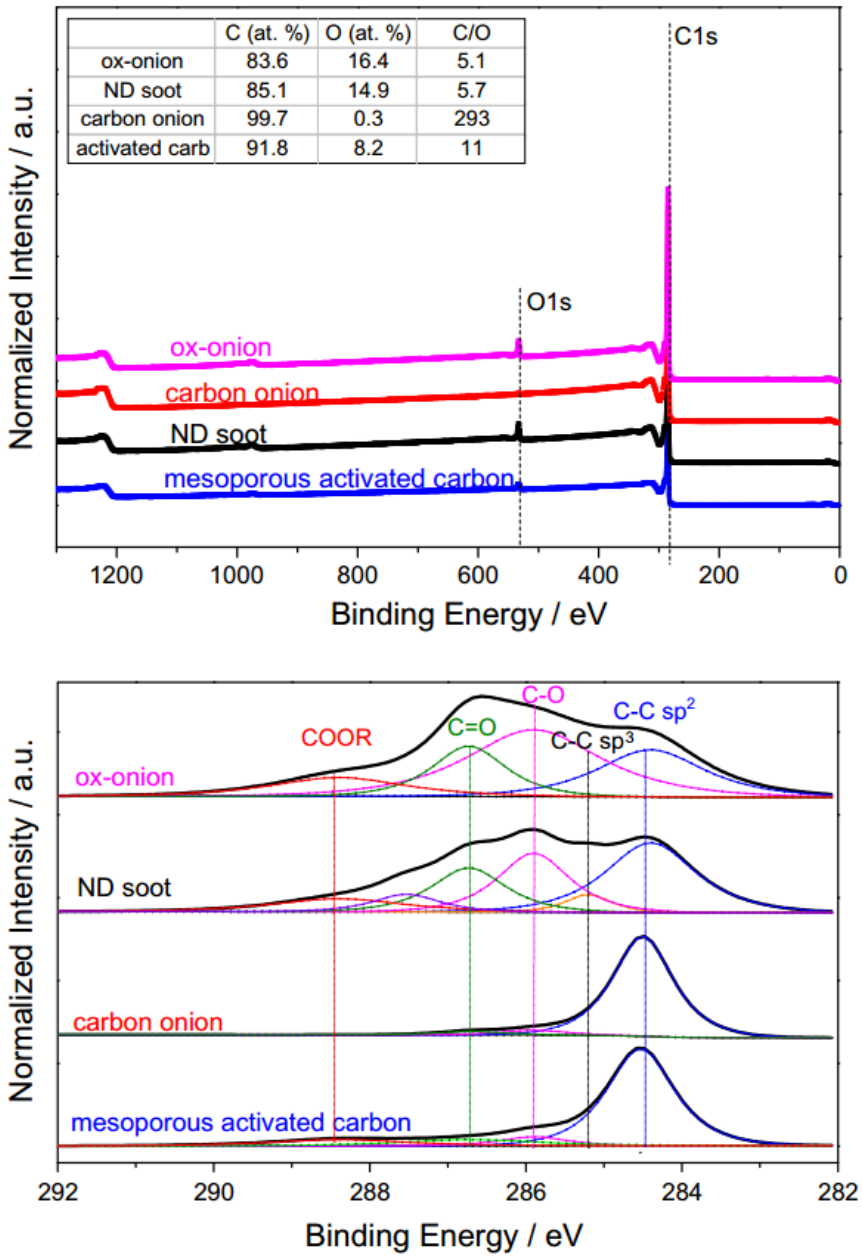

Figure 3.4 XPS analysis of all tested samples (a) and peak fitting of C 1s at high resolution (b). The inset table shows the atomic percentage of carbon, oxygen and their ratio, respectively.

Table 3.1 The surface areas of ND soot, carbon onion, oxidized carbon onion and 4S

Material	Surface area (m^2 g^{-1})
ND soot	617
Carbon onion	384
Oxidized carbon onion	578
4S (activated carbon)	1183

Further analysis on the high resolution C-1s peaks revealed that the oxidized carbon onion contains a mixture of carboxyl groups (COOR), hydroxyl groups (C–O), and carbonyl groups (C=O). ND soot, another sample containing high O content, showed mostly the presence of hydroxyl and carbonyl groups. This sample also demonstrated the presence of the sp^3 carbon on the surface, suggesting that not all the diamond nanoparticles are completely coated with sp^2 carbon. Interestingly, in contrast to the high O content initially detected in activated carbon sample, the C peak analysis revealed a very small content of functional groups, suggesting that the majority of O observed in the survey was physisorbed within the activated carbon micropores, most likely as moisture or CO_2.

To examine the bulk chemical composition, we characterized the carbon samples by energy dispersive spectroscopy (EDS) (Figure 3.5). In this case, however, we used electrodes that contained 10 wt.% fluorine-containing PTFE binder in addition to carbon. This approach prevented individual powder particles from leaving the sample holder during pumping and purging of the SEM microscope. While no oxygen could be detected in carbon onion sample, oxidized ox-onion sample showed 18 at.% O, supporting XPS results (Figure 3.5). The slightly higher O content detected by EDS in oxidized carbon onions and in activated carbon samples could be related to both the experimental error

and to the small differences in the amount of physisorbed oxygen on the surface of the powder (XPS measurements) and in the bulk of the electrodes (EDS measurements). One may expect the largest amount of physisorbed moisture to be present in oxidized carbon onions and in activated carbon samples. In the former one - due to the strong hydrogen bonding between the carboxylic functional groups on their surface (Figure 3.4b) and polar H_2O molecules. In activated carbon we expect strong adsorption of H_2O due to the presence of micropores, which are known to result in the significantly larger interaction energy than mesopores or external surface of the particles because of the overlap of the interaction potentials from the closely spaced pore walls.

In order to investigate the possible presence of quasi-reversible Faradaic reactions between the functional groups on carbon surface and Li, while avoiding the undesirable reaction of Li with moisture, we have thoroughly dried the produced electrodes in vacuum at 100 ℃ for over 10 h. The drying procedure was performed within the glovebox oven and all the electrodes were never exposed to air prior to assembling them into electrochemical cells. Two types of electrolyte solvents have been explored – a EC:DMC:DEC mixture and PC. Between these two electrolytes, 1M $LiPF_6$/ (EC:DMC:DEC) solution is more stable because the organic solvents involved are more resistive to PF_6^- which formed during lithiation. On the other hand, the more hydrophilic 1M $LiPF_6$/PC solution may have better wetting properties on hydrophilic surfaces of oxidized carbon and show lower viscosity, higher mobility of Li and thus higher conductivity of electrolyte.

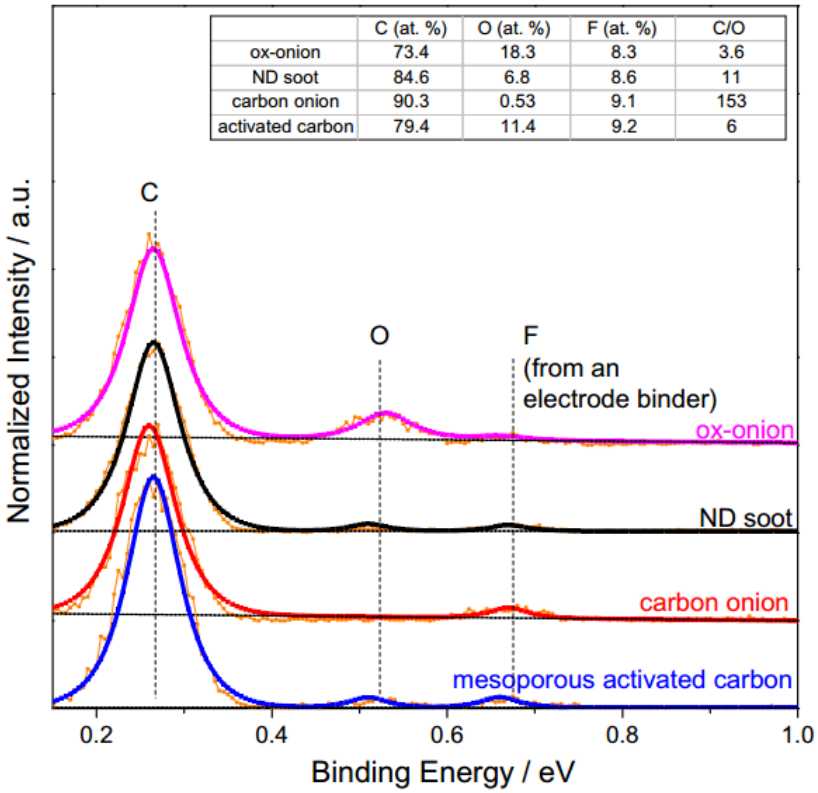

Figure 3.5 EDS analysis of all tested samples. The inset table shows the atomic percentage of each element in the tested samples.

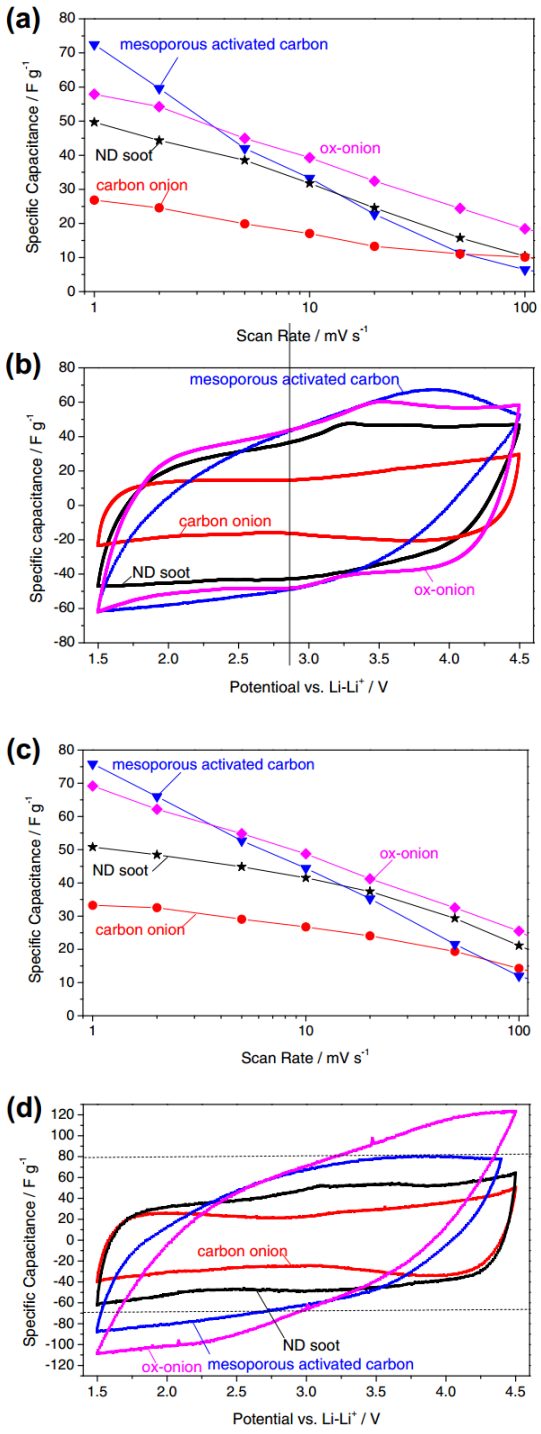

Figure 3.6 Capacitance of all tested samples at scan rates at 1-100mV s^{-1} in (a) DEC:EC:DMC; (c) PC electrolytes. (b and d) The CV loops of all tested samples at 10mV s^{-1}. Dash lines in (d) shows the scale of axis in (b).

Before discussing the results of our electrochemical evaluations of porous carbon electrodes with Li foil counter electrodes we would like to clarify that the key assumption utilized in our calculations is based on Li foil having significantly larger capacity (capacitance) for Li ions than that of the porous carbon. In this case the measured device capacitance is approximately equal to the capacitance of the working carbon electrode. At low current densities (<5 mA cm^2, in the units of the total current normalized by the surface area of each current collector) of charge–discharge tests or at the slow scan rates of cyclic voltammetry measurements (corresponding to a similar current value) this is a valid assumption. However, at higher current densities the rate of Li plating (dissolution) onto (from) Li foil may start limiting the overall device performance. Therefore, when considering the mass loading of 44 mg cm^{-2}, the results presented below may underestimate the actual capacitance (capacity) of carbon electrodes at the current densities above 100 mA g^{-1}, in the units of the total current normalized by the carbon electrode mass. However, since we utilized the same mass of various electrodes, the observed differences in the relative changes in the carbon capacitance at increasing current densities are real and are related to the differences in the porosity and surface chemistries of carbon electrodes under study.

We additionally like to clarify that in contrast to traditional Li-ion battery cathodes, porous carbon electrodes provides surface sites for electro-adsorption of both Li^+ cations and PF_6^{-1} anions and the measured capacitance accounts for the coordinated transport and adsorption/desorption of both of these species.

Figure 3.6 shows the changes in the capacitance of various carbon electrode in two types of electrolyte solvents when measured in the cyclic voltammetry tests in the

voltage range from 1.5 to 4.5 V vs. Li/Li^+. The specific capacitance of carbon onions in both types of electrolyte increases by over 2 times after oxidation (Figure 3.6a and c). Even when the capacitance is normalized by the BET SSA (Table 3.1), the oxidation increases the normalized capacitance from 8.5 to 11.9 μF cm^{-2} in a PC solvent and from 6.9 to 10.0 μF cm^{-2} in a EC:DMC:DEC solvent at a slow (1 mV s^{-1}) sweep rate, suggesting the pseudocapacitive contribution to the ion storage. The ND soot (with the highest BET SSA among the nanopowders studied) exhibited a higher capacitance than annealed carbon onion powder. However, its normalized capacitance of 8–8.2 μF cm^{-2} at 1 mV s^{-1} sweep rate is comparable to that of carbon onion powder. As expected, the specific capacitance of activated carbon electrode at low sweep rates (1–5 mV s^{-1}) is the highest among all the tested samples. However, the BET SSA (Table 3.1) normalized capacitance is only 6.1 and 6.4 μF cm^{-2} in EC:DMC:DEC and PC solvents, respectively. This is a very typical value for mesoporous activated carbons in conventional organic electrolytes (based on 1 M solution of tetraethylammonium tetrafluoroborate (TEATFB) salt in either PC or acetonitrile solvents) used in double layer capacitors, but up to two times smaller than that of the oxidized carbon onions. Both smaller average pore size (Figure 3.3b) and the small amount of chemisorbed (and possibly electrochemically active) oxygen (Figure 3.4b) could be responsible for smaller area-normalized capacitance of this sample. Furthermore, at higher scan rates (>10 mV s^{-1}), the capacitance of 4S decreases faster than that of carbon onion-based electrodes (Figure 3.6a and c). This indicates a slower ion transport in smaller pores of an activated carbon, particularly when functional groups interact with electrolyte solvent. It might be appropriate to note that the ion mobility and ionic conductivity of Li-free electrolytes

utilized in commercial electrochemical capacitors is nearly an order of magnitude higher than that of the Li-ion battery electrolytes used in our study, which likely contributes to the reduced rate capability of activated carbons we observed.

Compared to EC:DMC:DEC, all tested samples showed slightly larger capacitance at all scan rates in the PC solution. This could be due to a higher ionic conductivity of the PC solution combined with its higher polarity and thus higher dielectric constant (double layer capacitance is proportional to the effective dielectric constant of the electrolyte) and possibly better wetting, particularly on the oxidized carbon, ND soot and activated carbon surface, which contain polar functional groups and defects. We were slightly surprised by the higher capacitance of surface defects - free (and thus rather hydrophobic) surface of carbon onion in a polar PC solvent. This result may suggest that the contribution of higher ionic conductivity and dielectric constant of PC overshadows the difference in wetting properties of two type of solvents. The cyclic voltammetry (CV) loops (Figure 3.6b and d) provide additional insights into origin of the different behavior of carbon electrodes. Among the studied samples, only carbon onion powder shows a near rectangular shape in both electrolytes with no Faradic peak visible, which indicates that electric double layer capacitance dominates ion storage in this sample. The ‘‘butterfly’’ or ‘‘dumbbell’’ shape of its CV curve with a minimum capacitance at an open circuit voltage (OCV, 3 V vs Li/Li^+) is often observed in EDLC electrodes[102-105] and may arguably be related to ‘‘in-operando carbon doping’’, to the changes in the carrier density within carbon and to the distortion of the solvation shells at potentials further away from the OCV.

Several types of the distortions of the theoretical rectangular CV shape were observed in oxidized carbon, ND soot and activated carbon electrodes. First, ND soot, oxidized carbon onion and to a less extent activated carbon show Faradic peak couples during the cathodic/anodic scan (3.3 V/2.7 V for ND soot, 3.5 V/2.9 V for ox-onion), which could be seen particularly clearly in DEC:EC:DMC-based electrolyte (Figure 3.6b) and are related to the redox reactions of surface functional groups which provide pseudocapacitance. Due to the relatively slow rate of the redox reactions, the large deviations in the position of the anodic and cathodic peaks are visible even at a moderate (for EDLC devices) scan rate of 10 mV s^{-1} . At higher sweep rates the Faradic peaks on the loops of ND soot and ox-onion are significantly reduced, which causes a loss in their capacitance. Second, the kinetic limitations – related curvature of the CV semi-vertical curves after changing the current direction is quite significant for activated carbon electrode in both electrolytes (Figure 3.6b and d) and for ox-carbon sample in a PC-based electrolyte (Figure 3.6d). This is the major cause of capacitance reduction of the activated carbon sample (Figure 3.6a and c) at higher sweep rates, when the diffusion of ions in smaller pores becomes insufficiently fast. Finally, the CV curves for all the samples (except the carbon onion one) show a constant slope (a higher current at a higher potential). The value of the slope is the highest for the ox-onion sample. The equivalent circuit of the slope could be represented by the addition of the resistive leak current parallel to the electrode (Figure 3.7). We speculate that the leak current is largely related to the undesirable side reactions of the electrolyte with the functional groups present in the samples. The value of the slope and thus the leak current density is evidently dependent on a solvent (the slope is higher in a PC based electrolyte) and, therefore,

could possibly be minimized by further electrolyte optimization. Table 3.2 shows leakage resistance values calculated at different potential sweep rates. Carbon onion's CV diagrams do not show any clear slope. The highest leakage (smallest leakage resistance) was observed in samples with higher content of functional groups (such as, ox-onion), suggesting that side reactions between electrolyte and functional groups contribute to the leakage current. The observed leakage clearly emphasizes a significant obstacle for the implementation of functionalized porous carbon electrodes in Li-ion electrochemical energy storage devices.

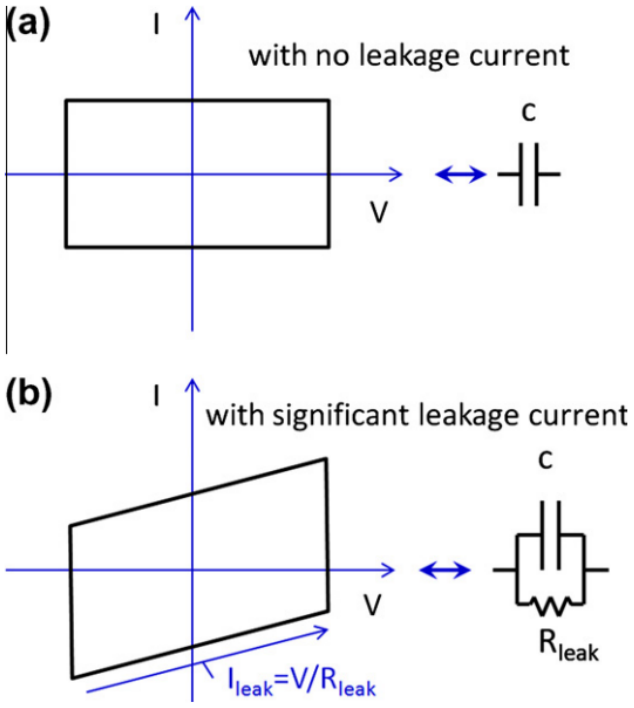

Figure 3.7 Schematic cyclic voltammograms and their equivalent circuits of in ideal capacitor with infinitely fast response: (a) without a leakage resistance, (b) with a leakage resistance.

Table 3.2 Leakage resistance of all tested samples in DEC:EC:DMC and PC

Electrolyte solvent	Sweep rate	Estimated leakage resistance R_{leak} (kOhm cm^2)			
		Carbon onion	ND soot	Activated carbon	Ox-onion
DEC:EC:DMC	1 mV s^{-1}	N/A	15	3	3
	5 mV s^{-1}	N/A	15	3	3
	10 mV s^{-1}	N/A	15	3	3
PC	1 mV s^{-1}	N/A	12	1.3	2
	5 mV s^{-1}	N/A	12	1.3	0.7
	10 mV s^{-1}	N/A	10	1.2	0.7

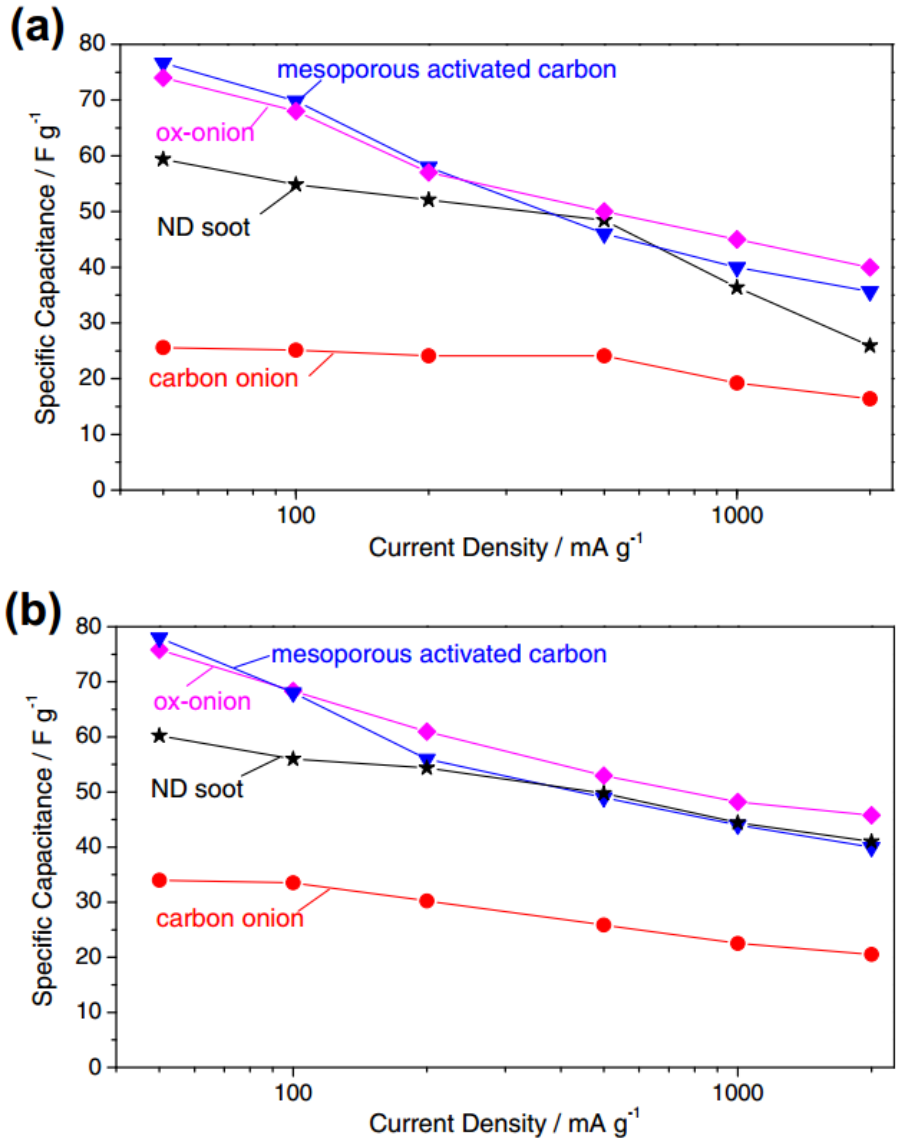

Figure 3.8 The capacitance variance of all tested cells with current density

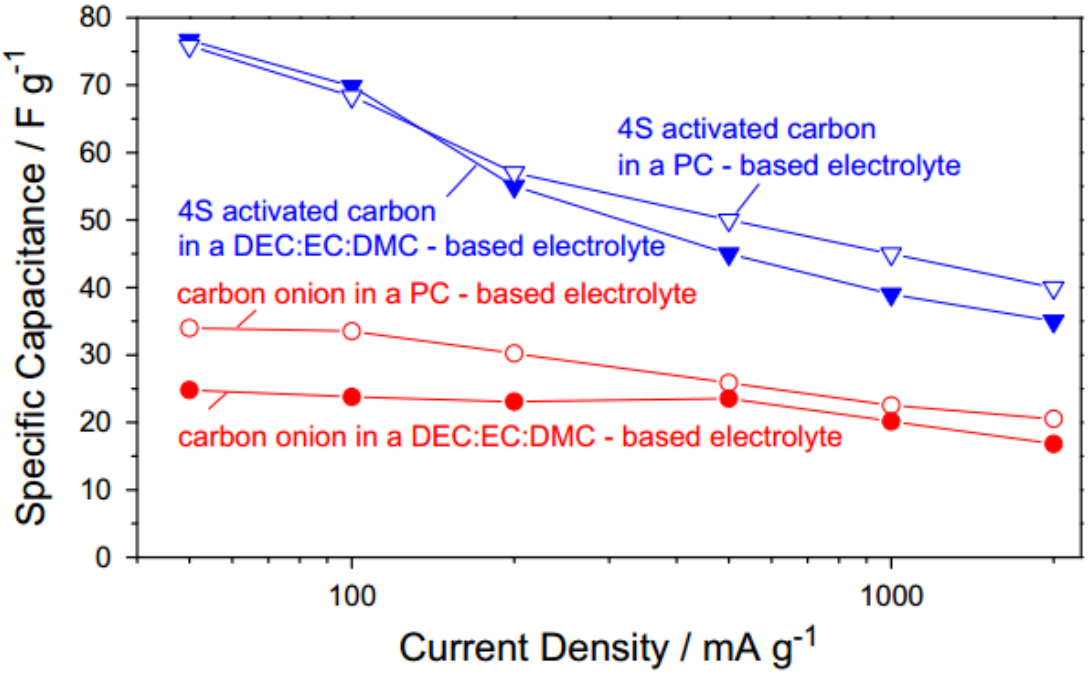

Figure 3.9 A comparison between the capacitances of materials in DEC:EC:DMC- and PC- based electrolytes.

Constant current charge–discharge (C–D) test is the most common route to evaluate both the capacitance and capacity of materials at different current densities. The results of C–D tests (Figure 3.8) follow the dependences observed in CV measurements (Figure 3.6): capacitance of carbon onion increases drastically after oxidation; 4S activated carbon shows the highest capacitance and the lowest capacitance retention at increasing current densities. The effect of electrolyte solvent on the capacitance of cells is illustrated more clearly in a separate graph (Figure 3.9). The capacitance of carbon onion is higher in PC-based electrolyte than in DEC:EC:DMC-based electrolyte, similarly to the previously discussed CV data (Figure 3.6). However, activated carbon, ND soot and ox-onion samples show similar capacitance in both electrolytes in C–D tests performed at a relatively low current densities (<200 mA g^{-1}). At higher current densities, activated

carbon in the PC-based electrolyte exhibits higher capacitance (Figure 3.9), likely due to the higher conductivity needed to maintain fast ion transport. The similarly observed improved capacitance retention of ND soot and ox-onion samples in a PC-based electrolyte (Figure 3.8) is consistent with the CV measurements' results (Figure 3.6).

When compared to previous studies, our results show significantly smaller capacitance of a wide variety of functionalized mesoporous carbons (Figure 3.9), in spite of their higher specific surface area (Table 3.1, Figure 3.3), similar content and type of the functional groups present, similar electrolyte and electrochemical testing regime. Since specific capacitance of mesoporous carbon with no closed porosity should not depend on the electrode mass in the regime where kinetics of the ion adsorption is not a limiting factor, we expect similar value of capacitance in electrodes with smaller mass loadings. The origin of the very high capacitance previously observed in layer-by-layer assembled electrodes remains unclear.

In order to compare the performance of porous carbon electrodes with that of commercial cathodes we have additionally calculated gravimetric and volumetric capacity in the voltage range 1.5–3.5 V vs. Li/Li^+. The low density (<0.35 g cm^{-3}) and moderate ion storage capability of the studies porous carbon electrodes resulted in a very small volumetric capacity of less than 23 mAh cm^{-3}, compared to 450 – 700 mAh cm^{-3} offered by conventional high-density cathodes used in commercial Li-ion batteries. In the view of the authors, even if the electrode density could approach 1 g cm^{-3} (which exceeds that of the investigated electrodes by over three times and is likely the upper limit for porous carbons), if the leakage current can be virtually eliminated (and this could be quite a challenging task), if the gravimetric capacity of thick electrodes may approach 150

mAh g^{-1} (which corresponds to the capacitance of 180 F g^{-1} , nearly three times higher than what is observed in our experiments), the volumetric capacity of functionalized porous carbon cathodes would unlikely exceed 20–25% of the state of the art intercalation-type cathodes (700 mAh cm^{-3}). In combination with lower average voltage of 2.5 V vs. Li/Li^+ in our study (and 3 V if the voltage range was extended to 1.5–4.5 V vs. Li/ Li^+) porous carbon cathodes will unlikely be able to offer more than 15% of the energy density of traditional cathodes, which represents a significant energy loss penalty for this cathode technology in Li ion batteries and thus may severely limit its applications.

3.4 Summary

With the goal of assessing the potential of high mass loading functionalized porous carbon cathodes in Li-containing electrolytes, we have investigated electrochemical performance of 5–10 nm carbon onion nanoparticles with and without functional groups present in their surface as well as nanodiamond soot having similar particle morphology and mesoporous activated carbon. Particle size and morphology of all the samples were studied using electron microscopy while their specific surface areas were evaluated using a N_2 sorption technique. The chemistries of their surfaces were evaluated using XPS and EDS measurements. Oxidation of carbon onions lead to the increase in their specific surface area and even high increase in their specific capacitance observed in both cyclic voltammetry and charge–discharge tests, due to the evident presence of pseudocapacitive reaction. In spite of the significantly smaller surface area, carbon nanoparticles with carboxylic functional groups showed specific capacitance similar to that of the activated carbon (up to 70 F g^{-1}). In addition, the larger average pore size and the absence of micropores in carbon nanoparticles's based electrodes resulted in

improved ion transport during charging and discharging processes and better capacity retention at higher current densities. When comparing two types of electrolyte solvents, a DEC:EC:DMC mixture and a PC, a more polar and less viscous PC often resulted in both slightly higher specific capacitance and better rate capability of the electrodes. On a negative note, undesirable reactions between the functional groups of the surface functionalized carbon onions and electrolyte resulted in noticeable and highly undesired leakage currents, which were found to be solvent-depend. Furthermore, the relatively low density (<0.35 g cm^{-3}) and moderate ion storage capability of all the studies porous carbon electrodes resulted in a volumetric capacity of less than 23 mAh cm^{-3}, which is 30 times lower than that offered by state-of-the art high-density cathodes used in commercial Li-ion batteries. The lower average voltage of porous carbon cathodes further lowers their energy density. Even with further improvements, we find it unlikely that porous carbon cathodes may be able to offer more than 15% of the energy density of traditional cathodes. Therefore, in our view both the significant energy loss penalty for this cathode technology and challenges minimizing the self-discharge may severely limit its applications.

CHAPTER 4

SULFUR-CONTAINING ACTIVATED CARBONS WITH OPTIMIZED PORE STRUCTURES FOR EDLCs

4.1 Introduction & Motivations

In the field of electrical energy storage, electrochemical capacitors (ECs) technology offering a combination of high specific power, and stable operation under short term high current pulses even in the case of full discharge [106,107] is an indispensible complement to Li-ion batteries. Potential applications of ECs range from power supplies for memories in micro-computers to rapid heating devices in copiers and industrial printers to power for on-demand lighting on roads to electrical motors in hybrid electric vehicles and industrial equipment to power sources in lasers, to name a few. The majority of commercial ECs are believed to function as electrical double layer capacitors (EDLCs), where the energy storage is purely electrostatic and virtually no charge transfer takes place across the electrode-electrolyte interface. Micro- and meso-porous carbons utilized in EC/EDLC electrodes have shown steady developments during the last decade and demonstrated increased specific and volumetric capacitance [108-110] and longer EC cycle life. [111-113] The contribution of reduction/oxidation (redox) pseudocapacitance reactions

to the double layer capacitance of porous carbons may potentially enhance their energy storage ability [114,115], but could also lead to undesirable leakage currents and device degradation [115,116] with cycling and/or storage, particularly at elevated temperatures. Unfortunately, the detection of pseudocapacitance contributions, required for systematic studies and material optimization, is not a trivial task since cyclic voltammetry (CV) curves may exhibit no evident peaks. This is because the enthalpies of various ion-electrode interactions on the surface of electrode materials may exhibit a very broad distribution. In fact, even the "classical" pseudocapacitance materials, such as hydrous ruthenium oxide, may show no characteristic peaks and exhibit a rectangular shape of the CV curves. [117,118]

Desirable properties of porous carbons for the majority of EC applications include high volumetric capacity (and therefore high particle density and high particle packing factor), the lack of uncontrolled side reactions with electrolyte (to achieve low self-discharge and long cycle life), scalable low-cost synthesis and consistent properties (such as pore size distribution, density, impurity content and surface functionalities). While several interesting methods have recently been explored for the microporous carbon synthesis, such as zeolite- [42,119-125] and/or mesoporous silica [26,104,126,127] templating, soft templating [128,129], and the use of inorganic carbide precursors for carbide-derived carbon synthesis [13,26,104,126,129-141], to mention a few, activated carbons (AC) will likely to dominate commercial EC applications due to their comparable and often superior performance combined with well-established manufacturing. [142-144] The recent advancements in AC synthesis from organic natural [34,142,145-149] or synthetic [143,145,150,151] precursors show rapid progress. To further advance the performance of ACs one needs to

fine-tune synthesis techniques to optimize carbon pore size distribution and to maximize the surface area accessible by electrolyte ions. Both too large [13,133,148,152,153] and too small [21,148,153-155] pores are known to offer inferior capacitance. During AC synthesis very small pores (not accessible by electrolyte ions in ECs) are formed by the shrinkage of the material during carbonization of organic precursors at high temperatures. [156]

To depress the pore shrinkage of micropores and therefore better match the pore size with charge carriers in the electrolyte, Hasegawa et al. [157] proposed sulfonation of carbon precursor by intensive acid treatment. Sulfur-containing functional groups were proposed to support the larger pores and avoid their collapse or shrinkage at high temperatures. However, acidic treatments offer rather poor control over the uniformity and distribution of S-containing functional groups in ACs. In addition, the pseudocapacitive reactions in EC induced by acid oxidations may, in principle, lead to undesirable self-discharge and device degradation. [115]

In this chapter, I will discuss how the intrinsic sulfur (S) - doping of activated carbon may reduce the content of the smallest bottleneck micropores and enhance the rate capability of EDLC electrodes. In the course of our study we systematically investigate how synthesis conditions of S-doped ACs influence their pore size distribution, specific surface area, microstructure and chemistry. I will also reveal how the physical and chemical properties of these AC affect their electrochemical performance in different aqueous electrolytes. More importantly, by using some of such carbons, we demonstrate that simple kinetic studies of cyclic voltammograms allow one to distinguish between slow pseudocapacitive reactions and faster double layer adsorption within microporous carbon electrodes.

4.2 Materials & Methods

For the synthesis of S-doped carbon, 2-thiophenemethanol (Aldrich) in CH_3CN was slowly added to $FeCl_3$ solution in CH_3CN. After kept under stirring for 15h, the mixture was filtered and PTh was separated. The obtained polythiophene (PTh) was then washed with distilled water and then acetone. The clean PTh was dried at 120 ℃ for several hours. The PTh was activated by heating up at 600, 800 and 850 ℃ with KOH for 1 hour. The KOH/PTh ratio is 2 for all the samples. To remove any residual inorganic salts, the activated samples were washed with 10 wt. % HCl and then distilled water until a neutral pH was achieved. Finally, the samples were dried at 120 ℃ overnight to remove all the remaining solvents and moisture. [158] The samples were labeled according to the annealing temperature as AC-600, AC-800 and AC-850 for 600, 800 and 850 ℃ respectively. Mesoporous activated carbon (CECA, 4S) was used for comparison purposes.

The morphology of all the samples was characterized using a scanning electron microscope (SEM) (LEO, Germany). All the samples were additionally studied under a transmission electron microscope (TEM) (JEOL, Japan). A LECO Tru Spec microanalyzer was used to calculate the (C, H, O) composition of the materials. The sulfur content of the samples was determined by means of a LECO S-632 analyzer. The surface analysis of the samples was completed by Thermal K-Alpha X-ray photoelectron spectroscopy (XPS). The structural characterization of tested samples was additionally performed by using Raman spectroscopy. Nitrogen sorption-desorption isotherms have been collected at 77K using a ASAP 2020 (Micromeritics, USA) in order to determine the surface area and pore size distribution of the samples. The BET surface area was

calculated from the isotherms in the range from 0.02 to 0.2 of relative pressures (P/P_0). Non-local density functional theory (NLDFT) calculations utilized for pore size distribution measurements assumed slit shape of the carbon pores.

All electrochemical measurements in this study were performed in symmetric beaker cells. Gold thin foils were used as current collector. Celgard 2325 membrane was used as separator. We used a suspension of the Polytetrafluoroethylene (PTFE) (Aldrich, 60 wt. % in water) as a fibrous binder. The total amount of the binder in electrodes was kept at 15 wt. %. The electrodes were thoroughly dried overnight and then assembled in beaker cells. The thickness of the electrodes was controlled at around 200 μm. The following electrolyte solutions have been selected for the study: 6M lithium chloride (LiCl), 1M hydrochloride (HCl) and 0.5M sulfuric acid (H_2SO_4) aqueous solutions. Cyclic voltammetry (CV) measurements were performed using a 1250 Galvanostat/Potentiostat (Solartron Instruments, USA) at different constant scan rate (1 - 500 mV s^{-1}) between -0.6V and 0.6 V. The capacitance of a symmetric cell was deduced from the loop area by the relation $C=A/(2\Delta V)$, where C is the cell capacitance, A is the loop area and ΔV the potential window. With the assumption that two electrodes assembled together are equal in capacitance, the capacitance of each electrode is double the value of the whole cell. Charge-discharge measurements were performed using a SCTS supercapacitor testing system (Arbin Instruments, USA) in the range of constant current densities (50 - 10000 mA g^{-1}) between -0.6 and 0.6 V. The capacitance was deduced from the charge-discharge curves by the relation $C=I/(dV/dt)$, where C is the cell capacitance, I is the current, dV/dt is the average slope of the discharge curve. Electrochemical impedance spectra (EIS) was performed by Gamry Reference 600

Potentiostat. Nyquist plots and Bode plots are recorded for characterization of impedance of tested samples. The EIS was performed within 10^{-2} - 10^{6} Hz frequency range.

4.3 Results & Discussion

4.3.1 Structural and chemical properties of the as-prepared S-doped activated carbons

The SEM studies revealed the average particle size of the produced ACs to range from 10 to 100 μm (Figure 4.1**)**. Although the micrograph of only one sample is shown, the morphology and particle size distribution of all materials are very similar. According to elemental analysis, the amount of S in the samples varied from as high as ~8.5 wt. % (~3 at. %) in the AC-600 sample to 3.4 wt% (~1.3 at. %) in the AC-800 sample and 2.5 wt. % (~1 at. %) AC-850 sample. The S % in pure PTh is 28.2 wt. % (~ 9 at. %), which is much higher than that in any material produced because part of S is lost in the form of SO_2 and CS_2 during carbonization and activation steps.

TEM characterization provided more insights into the effect of synthesis (activation) temperature on the microstructure of the produced ACs. While all the produced samples demonstrated uniform and highly disordered microstructure, higher synthesis temperature resulted in slightly larger and less curved graphene segments (Figure 4.2), suggesting a lower concentration of structural defects. This can be more clearly seen near the outer surface of the particles, where smaller sample thickness resulted in less overlap between the randomly oriented graphene layers. The variations in the TEM sample thickness combined with the lack of an order (alignment) within the carbon pores and the resulting pore overlap in the transmission imaging mode does not allow one to use TEM for visualizing variations in the pore size. Therefore, gas sorption

measurements were utilized to get a precise evaluation of specific surface area (SSA) and pore size distributions (PSD) of the produced AC samples.

The shape of nitrogen (N_2) sorption isotherms (Figure 4.3a) provides us insights about the porosity of the samples. The N_2 uptake at low relative pressures ($P/P_0 < 0.1$)) indicates the relative volume of the micropores.[159] Therefore, one would expect the smallest volume of micropores (pores < 2 nm) in the sample produced at the lowest synthesis temperature, i.e. 600 ℃, whereas for higher activation temperatures, 800-850 ℃, the volume of micropores would be larger and similar. The increase in the N_2 uptake with the activation temperature up to P/P_0 ~ 0.5-0.6 for 850 ℃ is indicative of the generation of mesopores.[159] Indeed, as the activation temperature raises, an enlargement of the size and population of mesopores is observed (see Figure 4.3b). The sample produced at 600 ℃ exhibits the lowest volume of micropores (with a size centred at ~ 1.1 nm) and virtually no mesopores. In contrast, the samples produced at higher activation temperatures show similar pore size distributions (PSDs) below 2 nm, but increasing volume of mesopores (> 2 nm) with the activation temperature. The pore volume of the samples increases steadily with the synthesis temperature, whereas the SSA reaches its highest value for 800 ℃ (i.e. 3000 m^2 g^{-1}) (inset in Figure 4.3a). Remarkably, all the samples possess large SSA in the range between 1800 and 3000 m^2 g^{-1}, which is important for EC applications.

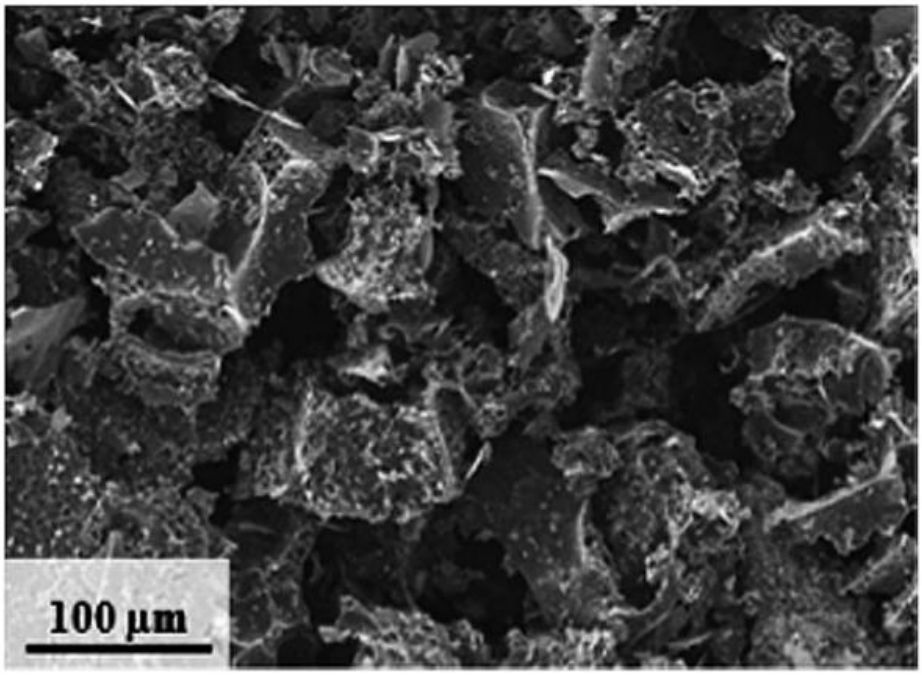

Figure 4.1 SEM micrograph of activated carbon sample synthesized at 800 ℃ (AC-800).

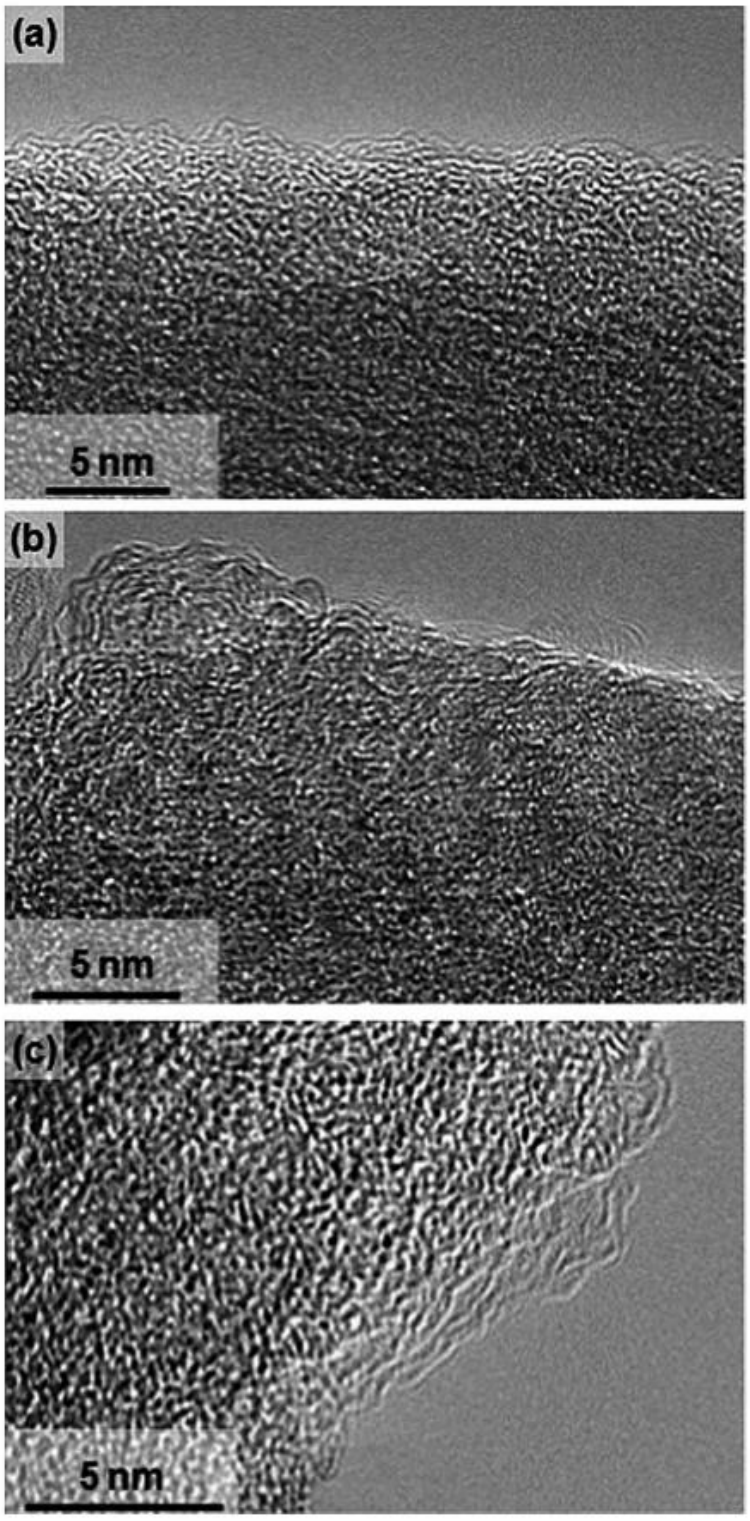

Figure 4.2 High-magnification TEM micrographs of activated carbon synthesized at (a) 600 ℃ ; (b) 800 ℃ and (c) 850 ℃.

The surface chemical properties of the produced materials were examined by X-ray Photoelectron Spectroscopy (XPS). Interestingly, in comparison to the elemental analysis measurements, XPS studies showed similar S contents for AC-800 and AC-850 but nearly 1.5 times higher S content in AC-600 sample. This suggests a uniform distribution of S along the particles for the samples synthesized at higher temperatures, whereas for the lowest activation temperature, the amount of S is higher in the surface than in the core of the particles. Figure 4.4 shows the C_{1s} and S_{2p} core level spectra of all tested samples. Two regions can be identified in the C 1s spectrum: (a) a region at 282 - 286 eV, which can be de-convoluted into two peaks at 284.3 eV and 285.1 eV, attributed by sp^2 and C-H bonding, respectively; and (b) a broad shoulder at 286-292 eV. This region represents an overlap of several peaks with similar intensities, including 286.5 eV (C=O), 287.2 eV (C-O and C-S), 289.1 eV (-CO_2-) and 291.2 eV (shape-up satellite due to π-π^* transition in aromatic rings). Because of the relatively low intensity of this shoulder, high full width at half maximum (FWHM) of all the potentially contributing peaks and possible variations in the position of each of these peaks, the quantitative analysis of the contributions of various functional groups to the XPS spectra becomes challenging and prone to errors. In contrast, analysis of the S_{2p} spectra is more straightforward. It consists of two doublets: a lower energy doublet at 164.0 and 165.3 eV, attributed to sulfide groups (such as -C-S-C- bridges), and a higher energy doublet at 168.6 and 170.1 eV, which can be assigned to sulfone bridges (-C-SO_2-C-). The doublet profiles in S_{2p} spectra is due to the spin-orbit splitting effect. It can be seen that the contribution of sulfone bridges increases with the decrease of the activation temperature (Figure 4b). Those sulfone bridges form as a consequence of the oxidizing conditions

present during the chemical activation process.[18] The area ratio of the doublets representing sulfide and sulfone groups slightly varies in different samples, indicating the existence of other minor functional groups.

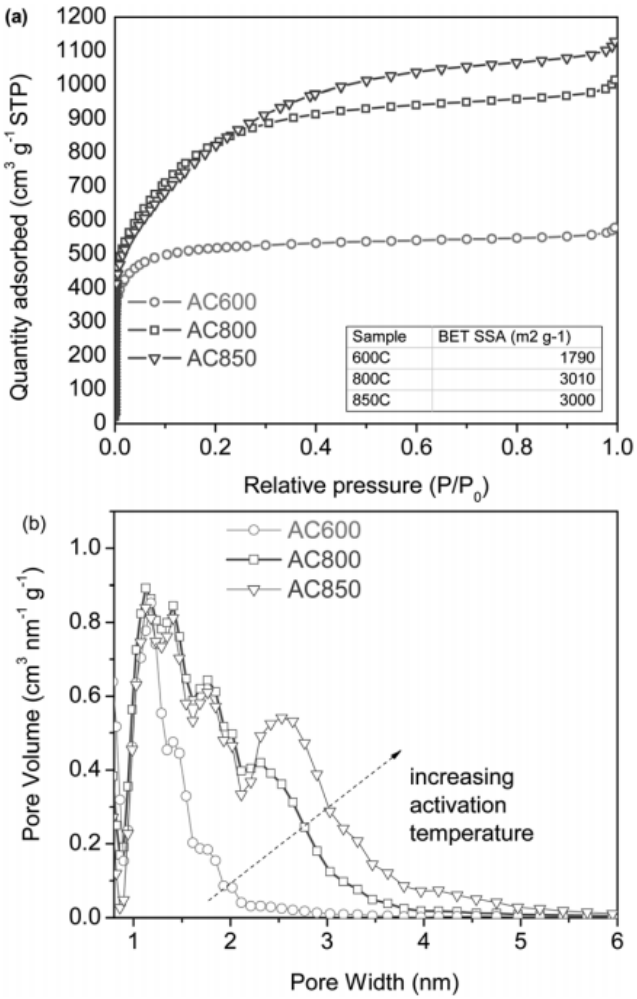

Figure 4.3 Porosity characterization of the S-containing activated carbon samples produced at four different temperatures: (a) N_2 sorption isotherms collected at 77K and (b) DFT pore size distributions.

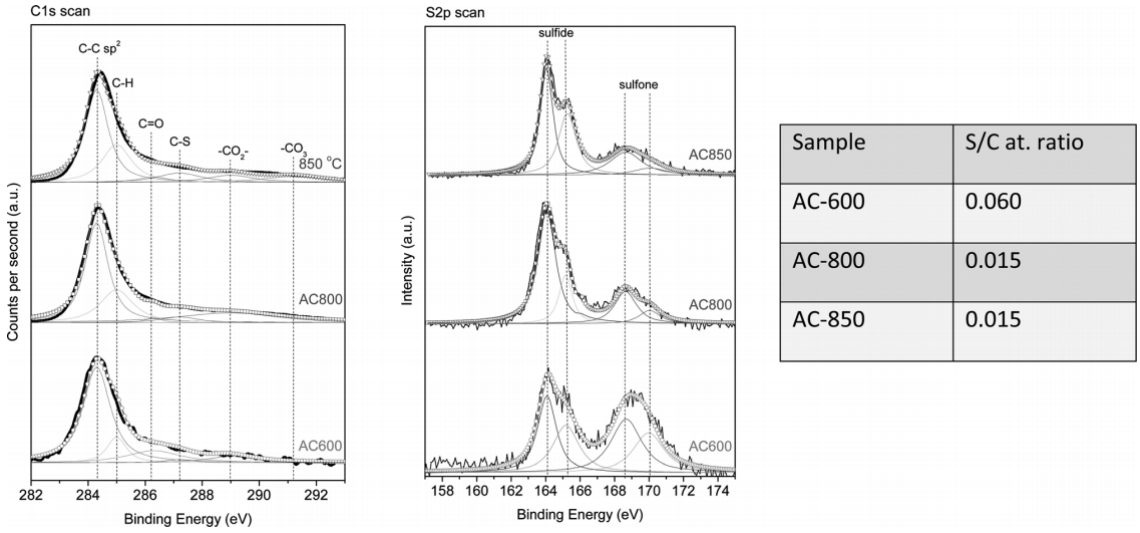

Sample	S/C at. ratio
AC-600	0.060
AC-800	0.015
AC-850	0.015

Figure 4.4 XPS analysis of S-doped activated carbon materials: (a) C1s and (b) S2p core level spectra.

Raman spectroscopy reveals the effect of synthesis conditions on the changes in the average microstructure of the produced ACs. In Raman spectra of carbon based materials (Figure 4.5), G band located at 1583 cm^{-1} is attributed to in-plane sp^2 C-C bond vibrations, as in planar graphite. The additional disorder-induced D band, forbidden in a perfect graphite by its symmetry and located at around ~1350 cm^{-1}, is currently believed to be linked to a double-resonance Raman process [160,161], when any phonon mode irrespective of the symmetry can give rise to this peak if the wave vector of the phonon is twice as large as the wave vector of the electronic transition excited by the incident phonon. The ratio of the integrated intensities of a disorder-induced D band and a graphite G band (I_D/I_G) is related to the number of defects in the structure [160,161]. Figure 4.5b shows decrease of I_D/I_G ratio monotonically with synthesis temperature, suggesting that faster atomic diffusion at elevated temperatures allows for the local re-structuring of carbon atoms and formation of larger graphitic segments and the reduced number of

defects. A slow decrease of the full-width at half-maximum (FWHM) of the D-band at higher temperatures (Figure 4.5c) similarly suggests an increase in C ordering within the AC samples. These results correlate well with previously discussed high-resolution TEM observations (Figure 4.2).

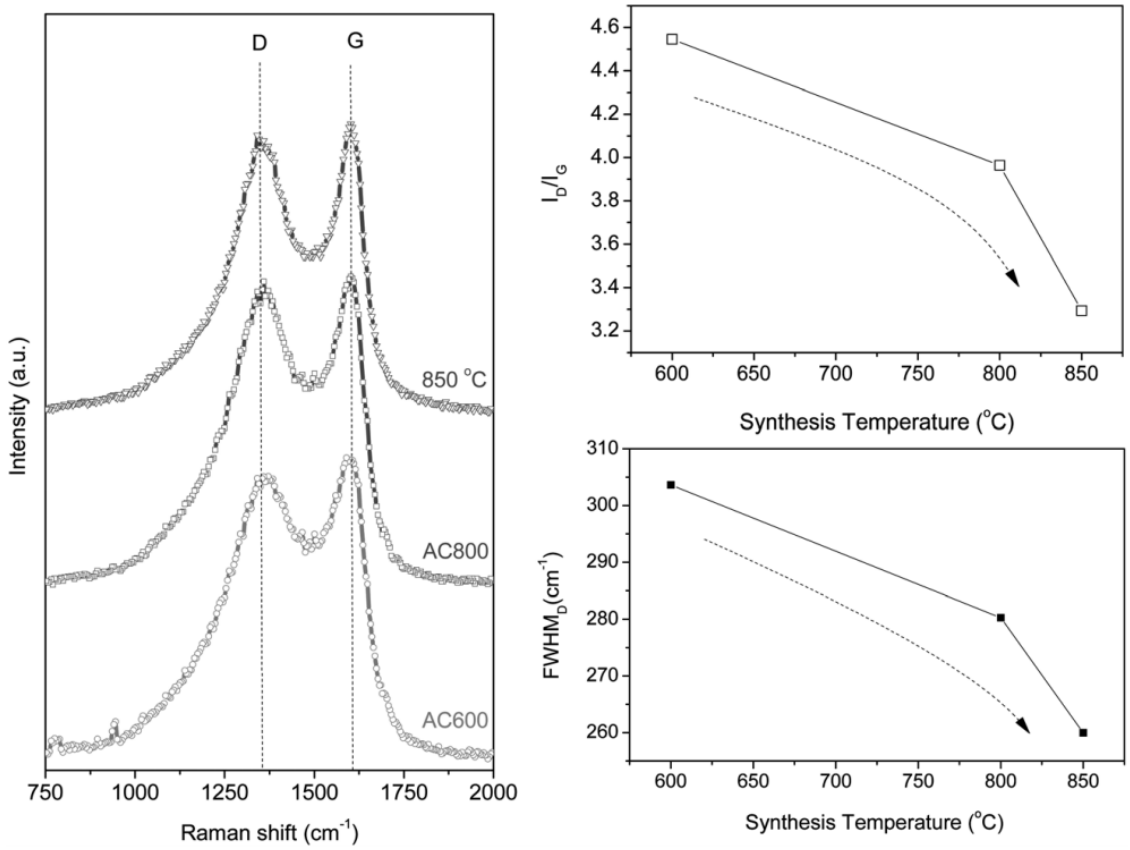

Figure 4.5 Raman spectroscopy of S-doped activated carbon materials: (a) Raman spectra, (b) the evolution of I_D/I_G ratio and (c) FWHM of a D-band, respectively, with synthesis temperature.

4.3.2 Electrochemical performance of S-doped activated carbons

Cyclic voltammetry (CV) studies performed on AC samples in different electrolytes reveal both the electrolyte ions - carbon interactions as well as the impact of the pore structure, ion chemistry and ion size on the transport and adsorption of ions

within the carbon micro- and small meso- pores. We have selected three different electrolytes for our studies: LiCl (6M), HCl (1M) and H_2SO_4 (0.5M) aqueous solutions. The use of LiCl was motivated by its pH neutrality. The employ of HCl allows the examination of the impact of the substitution of Li^+ by H^+. The lower molar concentration of the HCl solution was selected to mitigate the potential AC oxidation at higher applied potentials. The 0.5M H_2SO_4 electrolyte was selected due to its common industrial applications. In addition, we were interested in revealing the effect that bulky anions(such as HSO_4^- and SO_4^{2-}, in a simplistic case) may have on the ion transport rate in our carbon materials, in which we aimed to eliminate the smallest micropores.

Figure 4.6 shows representative CV behavior of AC-800 sample in these electrolyte solutions in a symmetric cell. The CV curves of this carbon materials in a pH-neutral LiCl electrolyte exhibits a perfect rectangular shape with no pseudocapacitive peaks visible and with nearly constant capacitance for the range of sweep rates (Figure 4.6a). Increasing the sweep rates from 1 to over 50 mV s^{-1} only affected the transient regions where the current direction was abruptly inversed (top left and bottom right portion of the curves) and high ionic fluxes within both the very thick (>200 μm) electrodes and the very large (10-100 μm) individual porous carbon particles were necessitated. However, after this transient period the specific capacitance was nearly unaffected by increasing the sweep rate. This suggests that the accessibility of the internal micropores to electrolyte ions was excellent and that little-to-no bottle-neck pores could obstruct the ions from reaching all the inner surface area even at such a high (for thick electrodes / large particles) sweep rates.

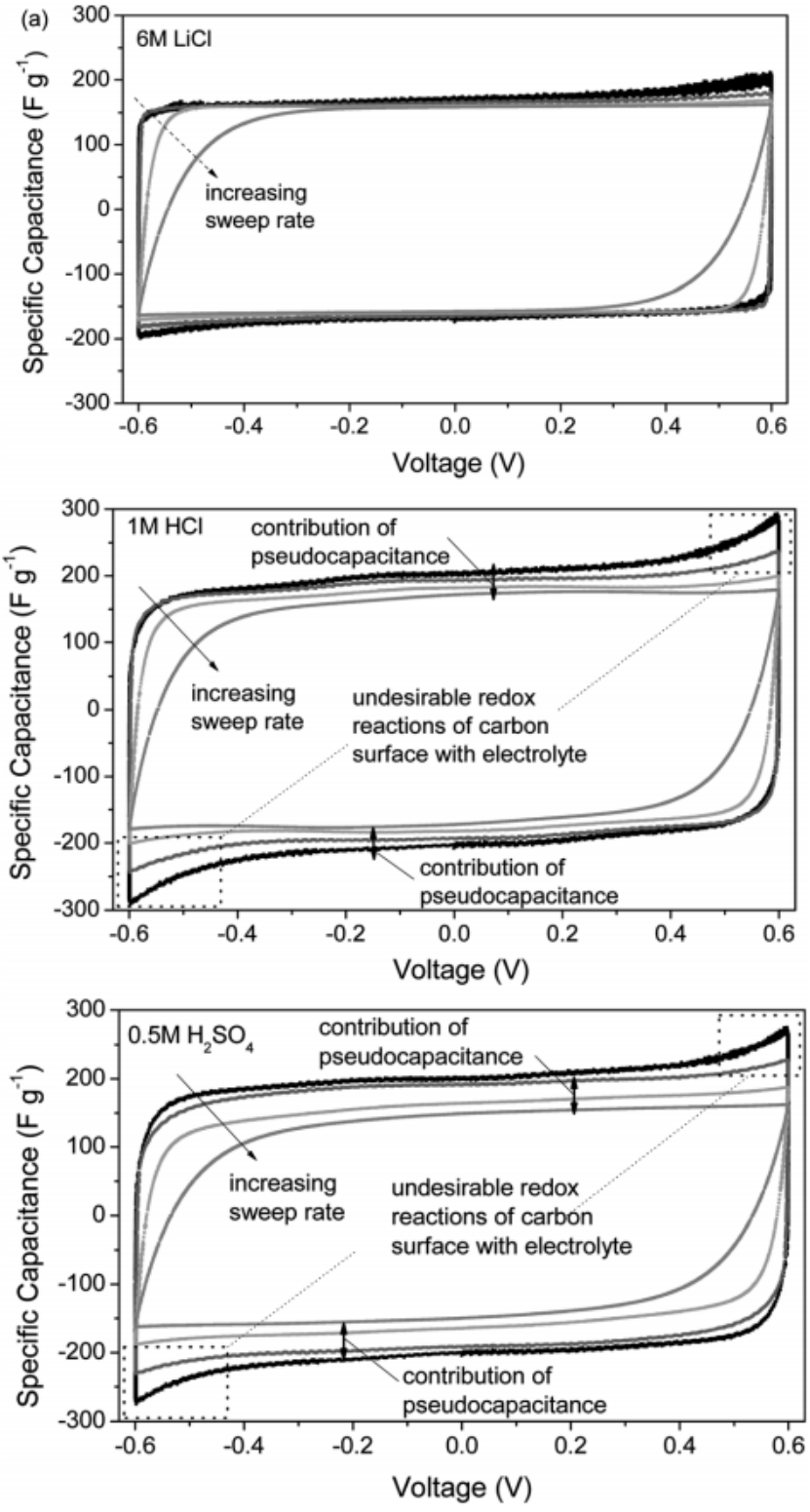

Figure 4.6 Cyclic voltammetry of AC-800 sample at the scan rates of 1, 5, 10 and 50 mV s^{-1} in three different aqueous electrolytes: (a) 6M LiCl; (b) 1M HCl; and (c) 0.5M H_2SO_4.

Interestingly, when switching to an HCl solution the CV curves changed markedly (Figure 4.6b). First, we observe an abrupt increase of the current when approaching higher voltages (near $\pm$ 0.6V), suggesting oxidation reactions and possibly some electrolyte decomposition. This can be seen particularly clearly at the slowest sweep rate of 1 mV s^{-1}. Second, we observe noticeably smaller capacitance (continuous decrease in current in the linear region from -0.3 V to 0.3 V) at higher sweep rates. Since the size of the H^+ ions in both the de-solvated state (0.035 and 0.09 nm, respectively) and the solvated state is smaller than that of the Li^+ (0.28 and 0.34 nm, respectively), the total device capacitance cannot be negatively affected by the replacement of Li^+ by smaller H^+. Furthermore, since the size of the solvated H^+ is much smaller than Li^+, we shall expect ionic accessibility of the internal micropores to be better for H^+. In contrast, we clearly observe lowering capacitance at faster sweep rates in the case of 1M HCl electrolyte, as deduced by comparing Figures 4.6a and b**.** Higher molarities of HCl results in even stronger sweep-rate dependence. The above results suggest that the inferior capacitance retention with increasing sweep rates of 1M HCl electrolyte is largely related to the slower pseudocapacitance redox reactions between the carbon functional groups and acidic electrolyte. The interactions of the ion solvated shells with polar functional groups may, in principle, further slow down the ion transport within porous carbon. [116] However, we observe similar capacitance decrease at higher sweep rates in the transient regions (after abruptly inversed current direction, compare Figure 4.6a and b), suggesting that the resistance faced by electrolyte ions traveling within the carbon pores remained similar. The addition of pseudocapacitance shall result in the increase in the maximum-achievable total capacitance, which we indeed observe. At the same time, at a higher rate (50 mV s^{-1})

(when redox reactions have insufficient time to proceed) the capacitance in both electrolytes is very similar. The combined effect of slightly larger anion size and slightly higher strength of the 0.5M H_2SO_4 electrolyte solution results in marginally slower rate capability and slightly higher pseudocapacitance contribution (compare **Figure 4.6c** and **b**). In both cases, however, we propose that the degree of the decrease in the specific capacitance with increasing sweep rates may serve as simple tool for the rough estimation of the pseudocapacitance contribution. We shall note, though, that such capacitance shall be measured at a voltage (in the case of a symmetric cell) sufficiently far away from the transient current range (in our case, away from -0.6V for the positive current loop of the CV or away from the +0.6V for the negative current loop of the CV) so that the ion transport rate within the carbon micro- and meso- pores is sufficiently fast to allow the double-layer to be established and the current/capacitance plateau to be reached at the highest sweep rate. A similar strategy can be used for the pseudocapacitance estimation from the differential capacity curves of the charge-discharge tests, when recorded at different current densities.

In order to assess the effect of the AC synthesis conditions on the EC performance we compare the CV graphs of AC-600 and AC-850 in 6M LiCl (Figure 4.7a and b). The pH neutral electrolyte minimizes oxidation reactions at higher voltages, which could mask the AC properties. The AC-600 synthesized at the lowest temperature and containing sulfone groups (Figure 4.4) exhibits quite poor performance. It has a distinguished redox peak near 0V and a visible oxidation process when EC is approaching 0.6 V (Figure 4.7a). In spite of its high specific surface area (Figure 4.3a), the value of the specific capacitance is rather small and indicates that a portion of the

surface area was not accessible by electrolyte ions even at the slowest rate. More importantly, the CV curves for this sample show a high slope (a higher current at higher voltage), which indicates a significant leakage current (Figure 4.8). Increasing the temperature to 800 (Figure 4.6a) or 850 ℃ (Figure 4.7b) virtually eliminates both the pseudocapacitance contributions and the leakage current (Figure 4.8c). Both samples perform almost as an ideal EDLC for all the sweep rates under study). This indicates that the sulfur present in these high temperature carbons (~1-1.3 at. %) is electrochemically inactive in LiCl and does not induce leakage, which is an important finding for this S-containing AC technology. To further illustrate the role of sulfide bridges in improving ion transport and increasing the electrochemically accessible surface area, a typical non-S-doped activated carbon with ~40 % lower surface area and broad pore size distribution (some pores up to 3 nm) was made into electrodes with the same thickness and mass loading and then characterized by CV. We observe that its capacitance is over 4 times smaller and its rate capability is inferior (compare Figure 4.7c with 4.6a and 4.7b). Such electrochemical tests indicate that introduction of sulfide bridges may serve as an effective route to depress the shrinkage of the smallest pores to afford rapid ion transport without inducing unwanted redox reactions.

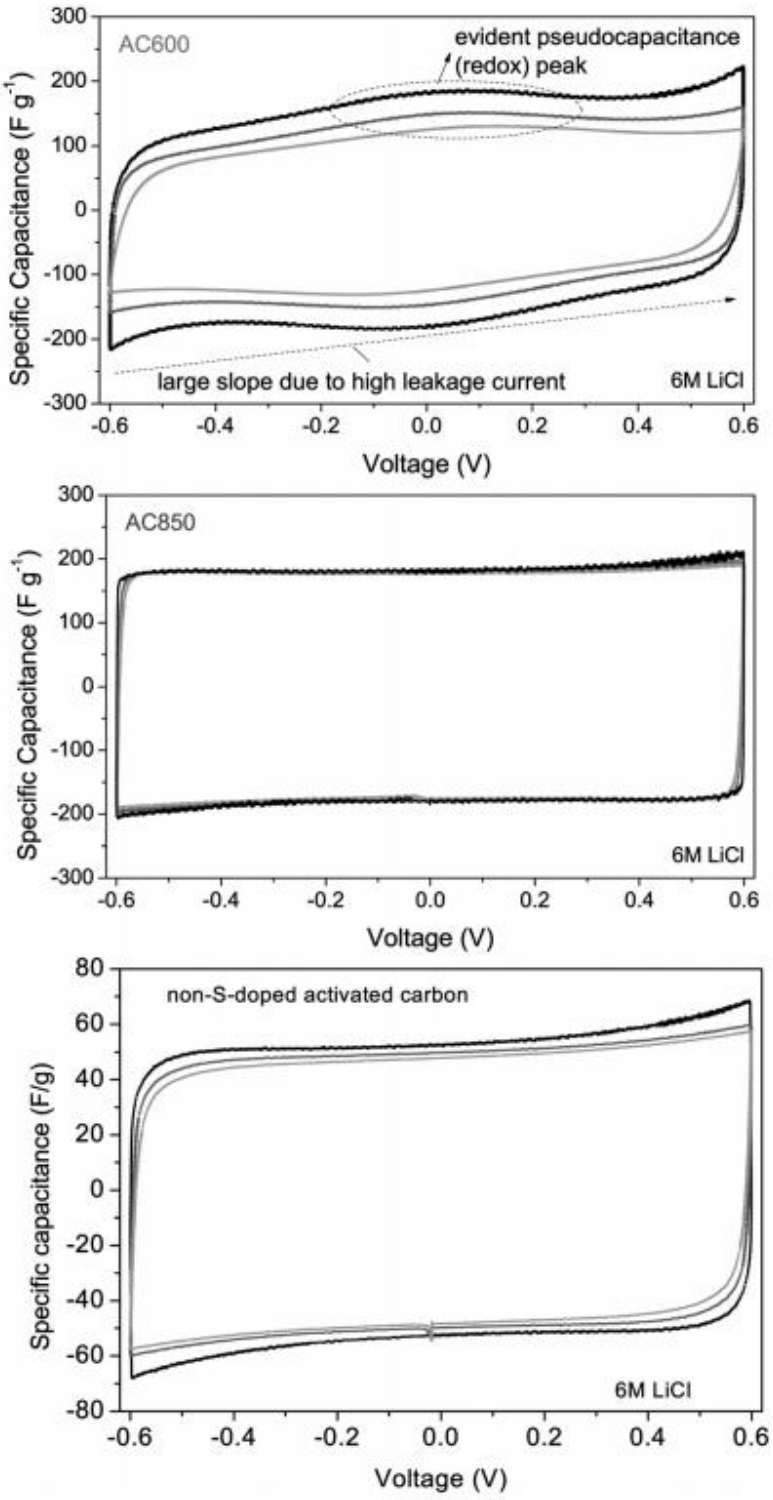

Figure 4.7 Cyclic voltammetry of AC samples synthesized at three different temperatures: (a) AC600 and (b) AC850; and (c) mesoporous activated carbon with pores in the range of 0.5–4 nm but no S doping. Beaker cells have been operated in 6 M LiCl aqueous solution. Presented data correspond to the sweep rates of 1, 5 and 10 mV s^{-1}.

Another important observation is that for almost all the tested samples equivalent leakage resistance was the highest in a pH neutral LiCl electrolyte (this corresponds to the lowest leakage current) and the lowest (highest leakage current) in a strong acidic H_2SO_4 electrolyte (Figure 4.8). Furthermore, we found a positive correlation between the parasitic leakage currents observed in some devices (see Figure 4.8c) and the pseudocapacitance contribution estimated from the capacitance retention measurements (Figure 4.9). This result serves as evidence that many redox-active functional groups contribute to the self-discharge of EDLCs and shall be avoided.

We propose that the presence of acidic functional groups participating in the pseudocapacitive reactions reduce the local *pH* in their proximity. This should trigger hydrogen generation at a negative electrode even at the potentials, where H_2O is thermodynamically stable in a neutral (e.g. LiCl) electrolyte solution. The use of acidic electrolytes (HCl and H_2SO_4 solutions) further enhances the hydrogen generation at the anode. Indeed, according to a Pourbaix diagram, water is prone to decomposition and hydrogen generation at a low pH according to:

$$2H_2O + 2e^- \rightarrow H_2 \uparrow + 2OH^- \qquad (1)$$

The electrons needed to sustain such reactions are taken from the charge stored within the carbon negative electrode. This decrease in the total charge leads to the release of a portion of the adsorbed ions constituting the double layer of this electrode in order to maintain the local charge equilibrium. This, in turn, raises the potential of the negative electrode and contributes to the self-discharge. A possible presence of basic functional groups on the carbon surface of a positive electrode may similarly induce the generation

of oxygen in their facility, consuming holes and lowering the cathode potential during storage. Oxidation of carbon cathode in the proximity of defects and functional groups may additionally lead to the generation of CO and CO_2. All of the described reactions may contribute to a leakage current and self-discharge of an EDLC.

The sulfur functionalities may contribute to pseudocapacitance by redox reactions involving sulphone groups. The proposed reactions are listed below. As the first step, some of the sulphone groups are reduced into sulfoxide groups (reaction 2). Sulfoxide groups are then reduced into sulfenic acid, which is reversible (reaction 3). A fraction of sulfenic acid can be ionized and adsorb positively charged protons or Li^+ (reactions 4 and 5).

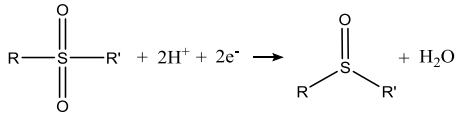

(2)

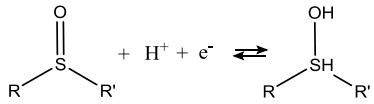

(3)

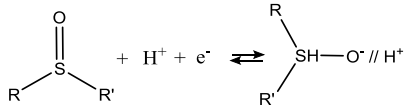

(4)

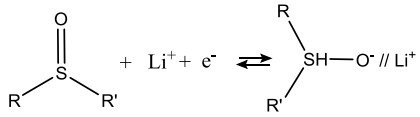

(5)

In addition to S, the tested materials, particularly those synthesized at a low temperature, contain different oxygen functionalities. Furthermore acidic electrolytes, especially H_2SO_4, tend to slightly oxidize the carbon electrode and induce oxygen-containing functional groups. Such functionalities are known to be involved in redox

reactions and contribute to pseudocapacitance. In an example of a quinone functional group, the redox reaction may proceed as following (Reaction 6):

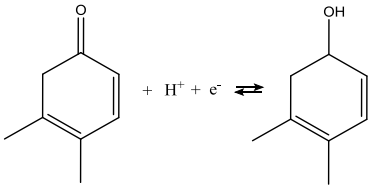

(6)

Figure 4.10 summarizes the changes in the integrated capacitance of S-doped AC electrodes in three types of electrolytes. All tested materials show higher capacitances in acid solutions due to the pseudocapacitance contribution. On the other hand, the capacitance retentions are better in a pH neutral LiCl solution since the redox reactions contributing to pseudocapacitance are slower than double layer formation. The rapid ion transport in AC-800 and AC-850 samples due to their relatively large pore size (Figure 4.3) and the lack of slow redox reactions leads to excellent capacitance retention. The strongly improved performance of AC-600 in acidic solution may be also result of its in-situ surface chemistry modification and thus improved electrolyte wetting (compare its performance in Figure 4.10a with that in Figure 4.10b and c).

Galvanic charge-discharge (C-D) tests performed at different current densities compliments CV tests and reveal largely similar trends (Figure 4.11): AC-800 and AC-850 possess both higher capacitances and higher capacitance retention than AC-600 sample. All electrodes show the highest capacitances in acidic electrolytes and the highest capacitance retention in a pH-neutral 6M LiCl solution, except for AC-600. This behavior can be explained by restricted accessibility to the porosity, slow redox reactions and high leakage current in 6M LiCl electrolyte.

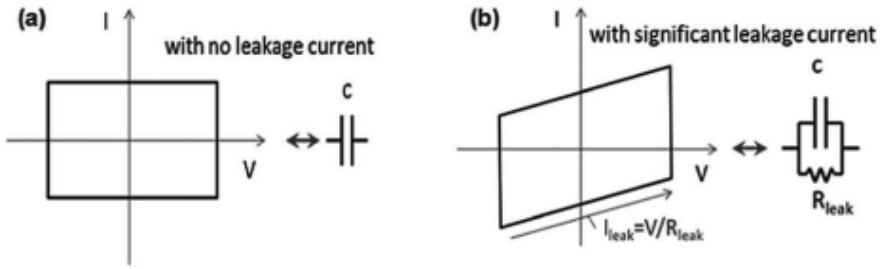

(c)

	AC-600	AC-800	AC-850
6M LiCl	4 kOhm·cm^2	N/A	N/A
1M HCl	3.6 kOhm·cm^2	23 kOhm·cm^2	N/A
0.5M H_2SO_4	0.7 kOhm·cm^2	12 kOhm·cm^2	15 kOhm·cm^2

Figure 4.8 Leak rate estimations. Schematic showing the cyclic voltammetry diagrams of idealized (infinitely fast with stable electrolyte) electrochemical capacitors (a) with no leakage current and (b) with significant leakage current and the equivalent circuits for these two conditions. (c) A table summarizing the leakage resistance measurements for each electrolyte and synthesized ACs.

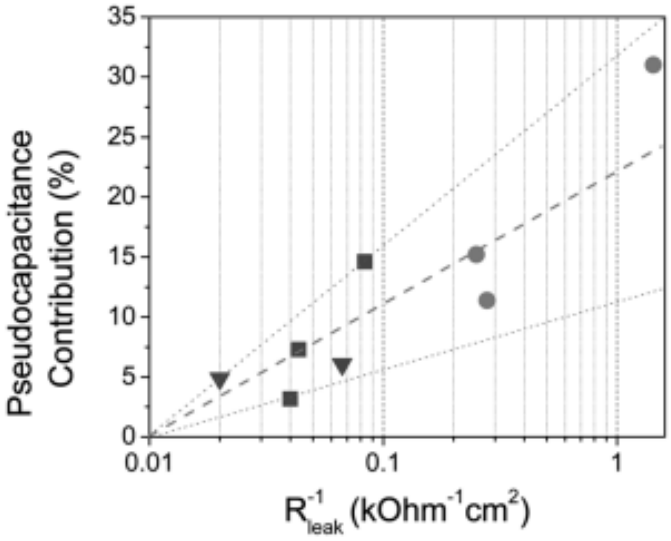

Figure 4.9 Pseudocapacitance of S-doped activated carbons AC600, AC800 and AC850 as a function of leakage conductance in different electrolytes. The pseudocapacitance was estimated from the difference between the currents measured at the potential sweeping rates of 1mV s^{-1} and 10mV s^{-1}. The rate was sufficiently slow to allow the double layer to be established.

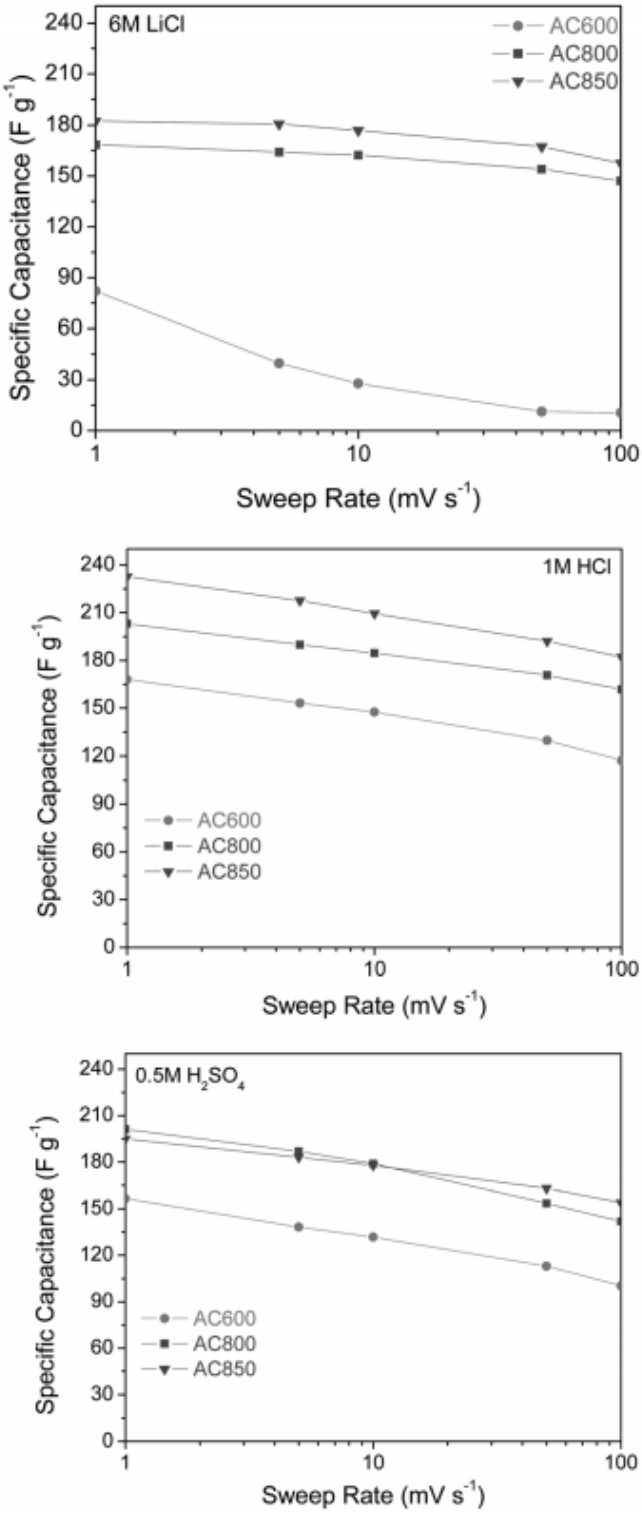

Figure 4.10 Specific capacitance retention of activated carbon samples produced at 600, 800 and 850 ℃ as a function of sweep rate in three aqueous electrolytes: (a) 6 M LiCl; (b) 1 M HCl; and (c) 0.5 M H_2SO_4.

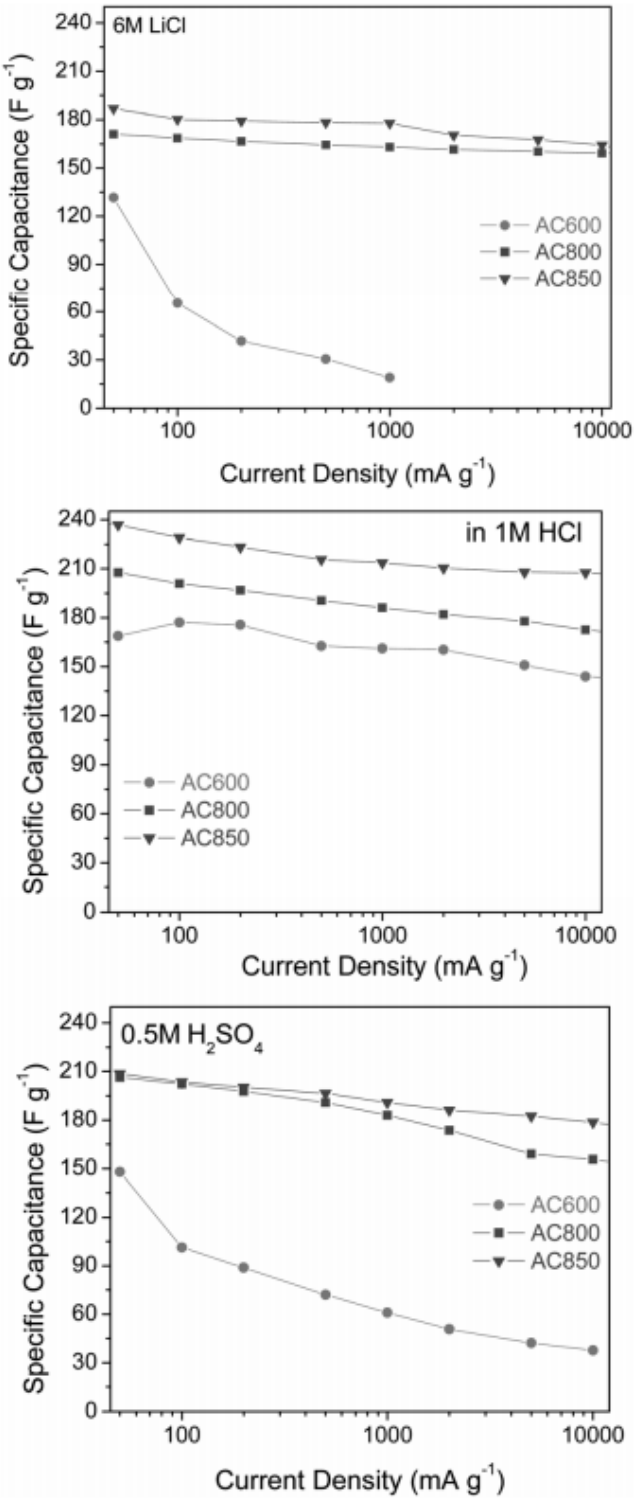

Figure 4.11 Specific capacitance retention of activated carbon samples produced at 600, 800 and 850 ℃ as a function of current density in three aqueous electrolytes: (a) 6 M LiCl; (b) 1 M HCl; and (c) 0.5 M H_2SO_4.

The voltage profiles of a AC-850 sample in 6M LiCl and 0.5M H_2SO_4 in C-D test are shown in Figure 4.12a-c. The constant slopes of most of the graphs are the typical for double layer capacitors, but cannot guarantee the lack of pseudocapacitance contributions, as previously discussed. The deviations from the linear curves, however, indicate redox activity (Figure 4.12c and d). The lack of IR drop in the AC-850 sample demonstrates a low device resistance. The AC-600 sample, in contrast, exhibits both severe distortions from the linearity of the curves (likely related to the pseudocapacitance reactions previously discussed) and high IR drop even at a very moderate current density of 50 mA g^{-1} (likely related to the slow electrolyte transport caused by the interaction of its original functional groups with electrolyte solvent).

To further investigate the presence of pseudocapacitance in highly functionalized samples, EIS characterization was performed. Shown in Figure 4.13 are the Nyquist plots of sample AC-850 (Figure 4.13a) and AC-600 (Figure 4.13b) respectively in 6M LiCl, 1M HCl and 0.5M H_2SO_4. Nyquist plots of AC-850 do not show any semicircles in electrolytes. On the contrary, plots of AC-600 show clear semicircles associated with the charge transfer processes, and these semicircles are larger for samples with higher pseudocapacitance.

The changes in the phase angle vs. frequency are shown in Figure 4.14. While the AC-850 sample shows the angle close to -90 ° (phase change = 0 °) for low frequency as an ideal capacitor, the AC-600 sample shows significant deviations from the ideal behavior. When comparing performance of AC-850 in different electrolytes, we observe that H_2SO_4 electrolyte, which introduces some pseudocapacitance, shows slower frequency response and larger time constant. In a pH neutral HCl electrolyte the time

constant is the smallest in both samples. In case of the AC-600 sample, this may indicate favorable interactions of the initially present functional groups in AC-600 with this electrolyte that favors better access of electrolyte ions to the carbon surface.

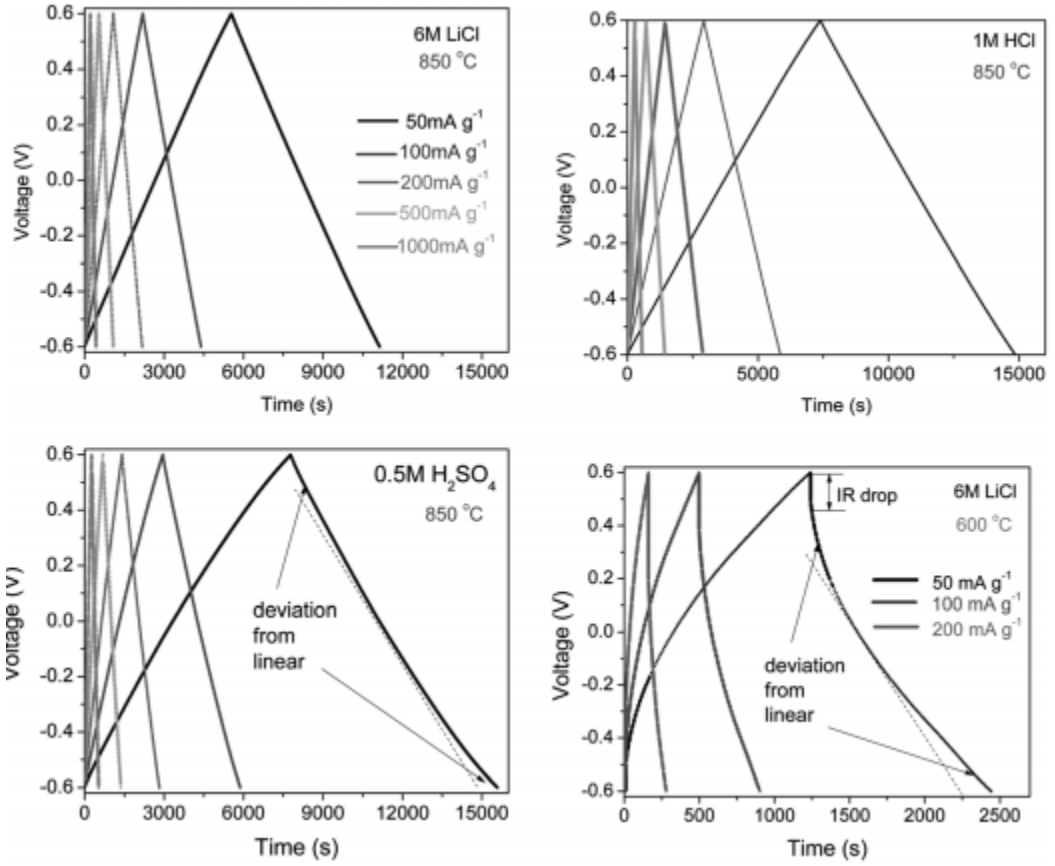

Figure 4.12 Charge–discharge characterization. Voltage profile of activated carbon synthesized at 850 ℃ at different current densities (50, 100, 200, 500 and 1000 mA g^{-1}) in (a) 6 M LiCl, (b) 1 M HCl and (c) 0.5 M H_2SO_4. (d) Voltage profile of activated carbon synthesized at 600 ℃ at different current densities (50, 100 and 200 mA g^{-1}) in 6M LiCl.

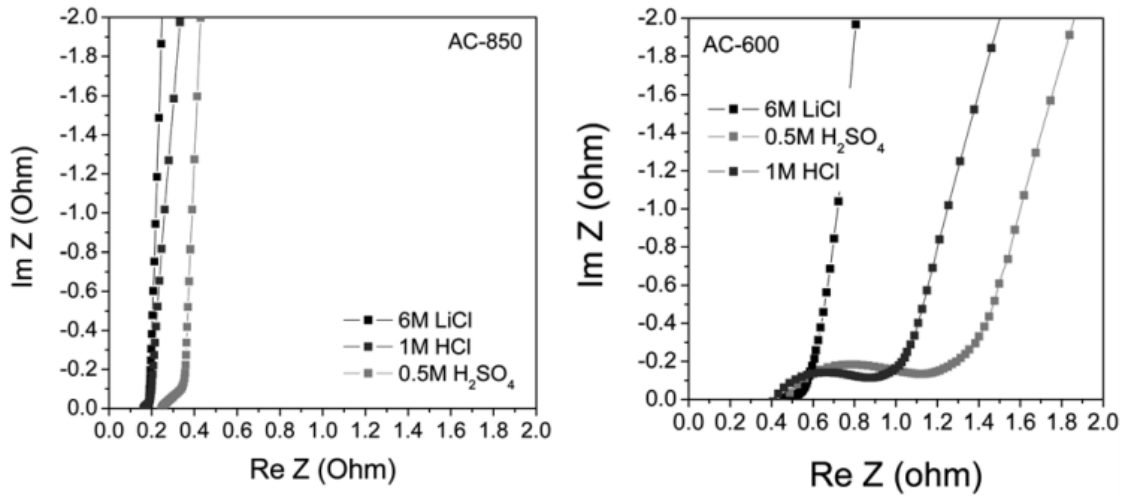

Figure 4.13 Nyquist plot of (a) AC-850 and (b) AC-600 in different electrolytes.

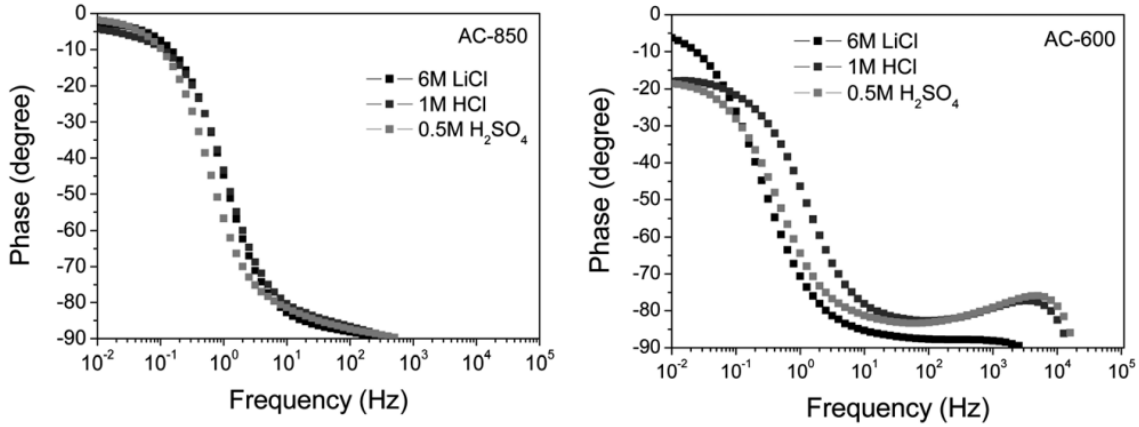

Figure 4.14 Bode plot of (a) AC-850 and (b) AC-600 in different electrolytes.

4.4 Summary

The intrinsic sulfur (S) - doping of activated carbon (AC) by carbonization of S-based polymers may be an efficient route to synthesize porous carbon for applications in EDLC electrodes with high rate capability and low leakage. The sulfide bridges present in the polymer precursors are proposed to resist the pore shrinkage during activation and reduce the amount of bottle-neck pores.

The ACs produced by carbonization and simultaneous activation of polythiophene show disordered carbon microstructure and specific surface area in the range ~1800-3000 m^2g^{-1}. Increasing synthesis temperature results in the enlargement of the pore size, as well as the reduction in the concentration of defects and sulfone functional groups. Synthesis temperatures of ~800 ℃ or higher were found to be required to achieve the desired S-doped AC characteristics in EDLC applications. In spite of the sulfur remaining in the samples produced at 800-850 ℃, they demonstrated little, if any, pseudocapacitance, excellent rate capabilities and low leakage currents when tested in symmetric EDLC devices with neutral aqueous electrolytes. In contrast, acidic aqueous electrolytes induced both the active redox reactions and significant leakage currents in EDLC devices.

We described the contribution of various functional groups to pseudocapacitance and observed a strong correlation between the carbon pseudocapacitance and the strongly undesirable device self-discharge during its operation. We proposed that the presence of functional groups participating in the pseudocapacitive reactions changes the local *pH* in their proximity and triggers electrolyte decomposition. This emphasizes the need to develop experimental techniques capable of estimating the pseudocapacitance contribution, even when cyclic voltammetry does not reveal any characteristics peaks.

We proposed for the first time a simple route to detect such a pseudocapacitance by harnessing the difference between the characteristic times required to establish a double layer in mesoporous carbons and that of the slower pseudocapacitive redox reactions. According to our method we measure the difference in the total specific capacitances recorded at two sweep rates: (i) a sweep rate sufficiently slow for both double layer and pseudocapaciance to contribute to charge storage and (ii) a sweep rate too fast for the redox reactions to proceed, but still sufficiently slow for the double layer to be fully established. A similar strategy can be used for the pseudocapacitance estimation from the differential capacity curves of the charge-discharge tests, when recorded at different current densities. In spite of its only semi-qualitative nature, the simplicity of this method shall allow it to become a valuable tool for a more comprehensive evaluation of carbon electrode performance in ECs.

CHAPTER 5

HIGHLY POROUS CARBON AS CONDUCTIVE SCAFFOLD FOR TRANSITION METAL CATHODE MATERIALS

5.1 Introduction & Motivation

Li-ion rechargeable batteries have been adopted as the major energy storage technology in a wide range of applications, such as portable electronics, portable medical devices, power tools, energy efficient industrial equipment and environmental-friendly transportations, to name a few. However, the performance of conventional intercalation-type cathode materials, such as lithium cobalt oxide (LCO), lithium nickel manganese cobalt oxide (NMC), lithium nickel cobalt aluminum oxide (NCA) and other lithium transition metal oxides, is often limited by the low capacity and relatively low energy density of such cathodes[162] The capacity of such electrodes is contributed by the lattice interstitials in the crystal, which can accommodate the Li ions. Because it usually takes at least one transition metal atom to build up such an interstitial, without a major change in the lattice structure during charge/discharge, the maximum theoretical capacity of such cathode structures would be limited to one electron transfer (one Li) per transition metal. In addition, commercial cathodes contain significant content of Co, which is an expensive, toxic and rare metal.

To break through this limit, transition metal halides, especially fluoride-based materials, have been explored as conversion-type cathode materials. Such cathodes achieve much higher gravimetric and volumetric capacities via a conversion or displacement reaction, where more electropositive Li ions replace transition metals (M) in the M-F bonds during Li insertion forming LiF. Due to higher valence of M, multiple electron transfers (multiple Li ions) could be accommodated by a single transition metal ion. The relatively high discharge potential could be achieved in such material system, which stems from the very high electronegativity of fluorine. However, because of their highly insulating ionic and electronic characters, metal fluorides (MF) have to be prepared at a nanoscale in order to provide acceptable power density by minimizing the paths for both electron and ion transport to electrochemical reaction sites. The most common procedure to prepare MF-based cathodes with small size and at the same time ensure reasonably homogeneous mixing of MF and C additive involves high energy ball milling.

However, in addition to not being energy-efficient, mechanical ball milling suffers from multiple other limitations. These include: (i) poor control over the dimensions and distribution of both MF nanoparticles and the MF-based composite particles; (ii) largely point contacts between the particles and conductive additives within a composite (which could be prone to failure due to internal stresses during charge-discharge cycles and volume changes during phase transitions); (iii) poor control over distribution of pores needed to accommodate volume changes and over pore size (with some of the pores being too large, which reduces energy density and some – too small, which may lead to mechanical failure); (iv) tendency for coarsening of the fluoride

particles by the heat generated during ball milling process, to name a few. To mitigate the impact of such inefficiencies, a very large content of conductive fillers (~50% or more) is often employed to achieve reasonable stability and conductivity of MF electrodes, while preserving small grain size. [163] To induce formation of chemical bonds between MF and nanocarbons and thus improve mechanical stability of electrodes, ionic liquid (IL) assisted synthesis has recently been proposed. [164] Yet the high cost of IL and the delicate synthesis process may hinder this method from wide applications. In addition to the issues described above, MF cathode may suffer from grain coarsening during cycling and the growth of the isolative layer on the metal (M) surface due to catalyzed decomposition of common organic electrolytes. [88,165] Most of previous studies do not address such challenges.

To address some of the limitations described above, in this work we introduce a simple, low cost, low temperature, high yield method for the formation of easy to handle, micron-size MF/C nanocomposites, where high stability and high conductivity could be achieved even for a small fraction of C. According to our approach, MF nanoparticles are confined within nanopores of porous conductive carbon. In this novel (for MF) approach, porous carbon (i) structurally supports the MF, (ii) prevents MF grain growth, (iii) accommodates the changes in volume of the active material, (iv) prevents physical separation of the M and MF particles during cycling and (v) delivers electrons or holes to the electrochemical reaction sites, even when a portion of the active material becomes electrically isolative. In addition, the nano-confinement may reduce the MF cathode dissolution during cycling. In our proof of concept study, we successfully demonstrate very high uniformity of FeF_2 nanoparticles formed and homogeneously imbedded within

a porous carbon matrix. Thus synthesized FeF_2/C nanocomposites achieve quite remarkable (for this system) rate performance and capacity retention.

5.2 Materials & Methods

Fe powder (99.9%, Sigma Aldrich), Fluorosilicic acid (H_2SiF_6, 23 wt% aq. sol.), poly (vinylidene fluoride) (PVDF, Sigma Aldrich) and 1-Methyl-2-pyrrolidinone (NMP, anhydrous, 99.5%, Sigma Aldrich) were used without further treatment. Fe powder was slowly added to fluorosilicic acid:

$$Fe + H_2SiF_6 = FeSiF_6 + H_2\ (gas)$$

After removing excess Fe powder by filtering, clear, saturated aqueous solution of $FeSiF_6$ was obtained as precursor. The precursor solution was then added dropwise to the highly porous carbon. Vacuum was applied in between precursor drop-adding operations to ensure the effective impregnation of the precursor solution in the carbon matrix. The precursor-loaded composite material was then annealed at 200 ℃ in Argon atmosphere for 4 hrs to obtain FeF_2 nanoparticles:

$$FeSiF_6 = FeF_2 + SiF_4\ (gas)$$

The weight percentage of FeF_2 in the resulting nanocomposites can be easily controlled by manipulating the amount of precursor addition.

Ball milled mixture of commercially available FeF_2 (98%, Sigma Aldrich) and carbon black (Superior Graphite) was prepared as reference sample. The materials were grinded into fine powders before vigorous mixing via high energy ball mill (8000M, SPEX SamplePrep) for 4 hrs.

The morphology of FeF_2/C nanocomposite was observed by scanning electron microscopy (SEM, LEO 1530) and tunneling electron microscopy (TEM, JEOL 100CX). Element analysis characterizations were operated by energy dispersive X-ray spectroscopy (EDX). The crystal structures of materials at various polarization status were characterized by X-ray diffraction (XRD, X'Pert PRO Alpha-1). The porosity of the carbon matrix before and after loading of FeF_2 was characterized by Brunauer-Emmett-Teller method (BET, Tristar).

For electrochemical characterizations, the synthesized FeF_2/C nanocomposite was mixed with 15 wt% PVDF binder in NMP and vigorously stirred for 4 hrs before casting on Aluminum foil current collector. The thickness of the electrode was controlled to be ~100 μm. After casting, the electrode was dried in vacuum at 100℃ for 8 hrs to evaporate the solvent. The electrode was then assembled against metallic Li which was applied as counter electrode in type 2032 coin cells. Galvanostatic charge-discharge (Arbin potentiostat) and electrochemical impedance spectra (EIS, Gamry 800) tests were performed respectively.

5.3 Results & Discussion

The proposed formation protocol involves several simple steps, as illustrated by Figure 5.1a. First, a near-saturated aqueous solution of $FeSiF_6$ (precursor) is vacuum infiltrated into hydrophilic highly porous carbon particles (Figure 5.1a, step 1). The precursor is added slowly (drop by drop), with periodic vacuum drying steps to guarantee sufficient infiltration of the precursor solution in the micropores. The strong capillary forces ensure that $FeSiF_6$ nanoparticles are precipitated inside the carbon pores during

drying (Figure 5.1a, step 2), rather than on the external particle surface. The last step involves a low temperature (240 ℃) thermal decomposition of $FeSiF_6$ into FeF_2 nanoparticles and gaseous SiF_4 product, which is continuously removed from the synthesis system (Figure 5.1a, step 3). FeF_2 nanoparticles are thus formed inside a confined space, which is defined by the size of the carbon pores. More importantly, nanoscale FeF_2 particles homogeneously distributed inside the carbon matrix could be obtained. As discussed in the introduction section above, the reversibility of electrochemical reactions between FeF_2 and Li could be enhanced for FeF_2 nanoconfined within conductive carbon pores (Figure 5.1b). If needed to increase the total content of infiltrated FeF_2, either the whole procedure or the steps (1) and (2) could be repeated. For a possible large scale production, the infiltration procedure could be fully automated.

We have selected uniformly sized activated carbon (AC) spheres as porous carbon matrix for our experiments. Our main motivation for the selection of regularly sized particles was the ability to easily observe formation of undesirable defects or precipitates (e.g. precipitates of FeF_2 nanoparticles or cracks) on the smooth outer surface of carbon spheres. But for practical applications, spherical powder shape also provides unique advantages, including higher rate electrode performance (for a given density) and higher coating uniformity.

There are multiple processes suitable for the formation of porous carbon spheres (see e.g. [166-169]), out of which we selected carbonization and subsequent activation of polydivinylbenzene spheres produced by precipitation polymerization. [170,171] Our choice of the precursor and the synthesis procedure was motivated by the combination of a relative simplicity of the processing and tight control over the sphere dimensions. Prior to

carbonization, polymerized spherical polydivinylbenzene powder was stabilized in air at 300 ℃ for 3 h. Activation was conducted in a CO_2 gas at 950 ℃ for 5 hours, similar to the procedure previously used by our group and others. [172-174] Figure 2a shows a typical scanning electron microscopy (SEM) image of the obtained carbon powder. The micron-scale spheres exhibit high particle uniformity and smooth surface. Some of the spheres are lightly agglomerated, but the degree of such agglomeration is very moderate and the agglomerates could be easily broken by ultrasonication.

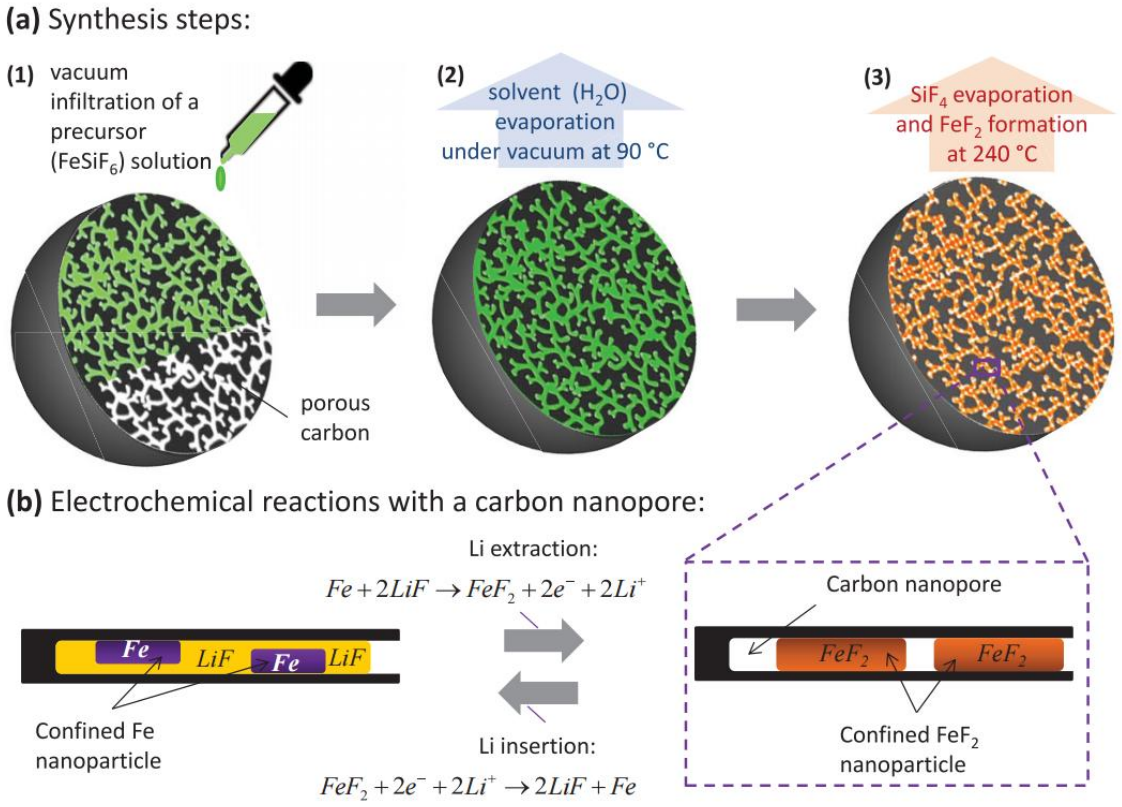

Figure 5.1 Synthesis and operation of nanoconfined FeF_2 : a) schematic showing the synthesis steps involved and b) reversible electrochemical reactions of FeF_2 with Li within a single carbon pore.

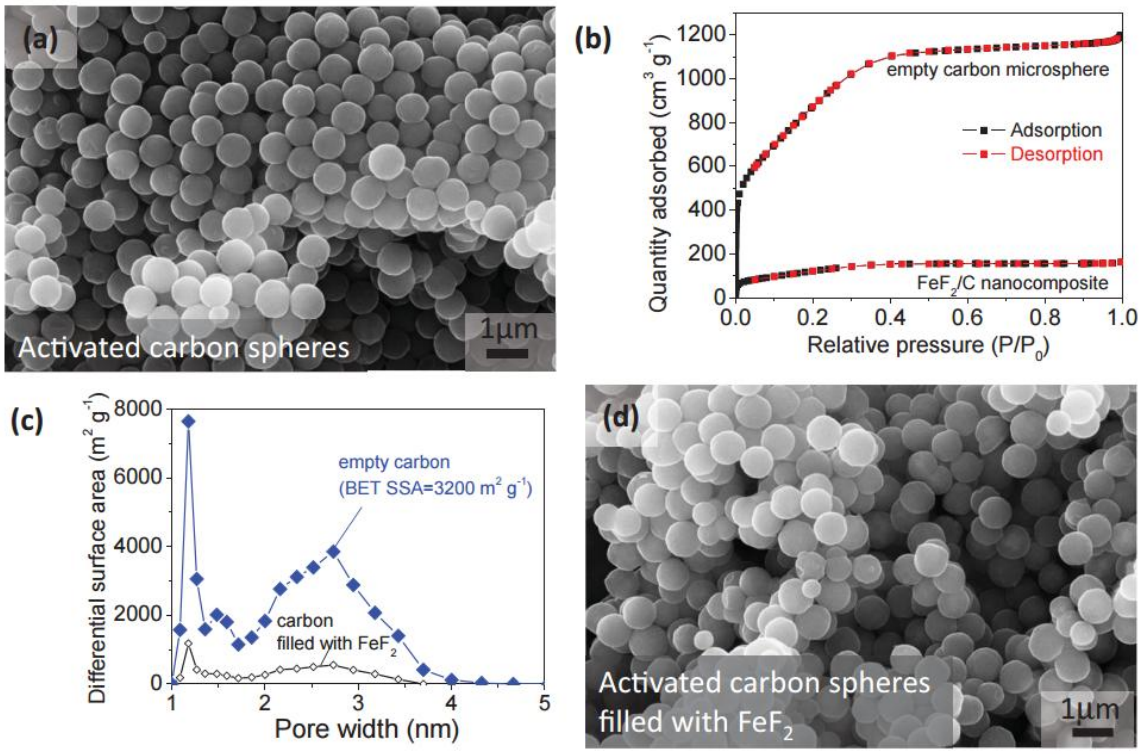

Figure 5.2 Microstructure characterization of AC spheres before and after infiltrating them with FeF_2 : a) SEM image of as-synthesized AC spheres; b) N_2 sorption-desorption isotherms of AC spheres with and without FeF_2 loading; c) pore size distribution of carbon spheres with and without FeF_2 loading; and d) microscopy image of AC spheres filled with FeF_2, thus forming FeF_2/C nanocomposite powder.

Nitrogen sorption measurements showed Type IV shape of the isotherm (Figure 5.2b) characteristic of porous carbons containing mesopores. [175] The lack of a significant hysteresis loop between the adsorption and desorption isotherms suggests that the size of the mesopores is smaller than around 10 nm. Non-local density functional (NLDFT) analysis [176]confirmed the pores in the range from 1-4 nm (Figure 5.2c), which are sufficiently small for electron tunneling from the conductive pore walls into FeF_2 reaction site (Figure 5.1b). Brunauer–Emmett–Teller (BET) specific surface area of the synthesized powder was rather large, ~ 3200 m^2 g^{-1}.

Infiltration of activated carbon spheres with FeF_2 was tuned by controlling the amount of precursor added to achieve the mass ratio of FeF_2:C to be 3:1. As expected, after FeF_2 loading, the porous space inside the carbon microspheres is greatly reduced (Figure 5.2b, c), indicating the successful material loading into the carbon pores. SEM micrographs of carbon microspheres after FeF_2 loading show very smooth surface and the absence of FeF_2 nanoparticles on the outer surface of the spheres (Figure 5.2d), suggesting high efficiency of the infiltration procedure, where all FeF_2 is confined inside the carbon nanopores.

Transmission electron microscopy (TEM) as well as results of the energy dispersive spectroscopy (EDS) scans across individual particles conducted in the scanning mode of the TEM (STEM) further indicate very uniform distribution of FeF_2 within individual spheres (Figure 5.3). Figure 5.3a shows the detailed morphology of a produced nanocomposite particle. STEM micrograph (Figure 5.3b) could be roughly approximated as the image of the projected density of the object (mass thickness contrast) and is often called Z-contrast imaging (where Z refers the atomic number and thus mass of the specimen atoms). The mass-thickness contrast is particularly useful for our study because the density is dominated by heavier Fe atoms of FeF_2 and thus their uniform distribution could be directly visualized. If less FeF_2 were in the center of each particle, the STEM micrograph would exhibit a donut-like shape. In contrast, we observe a projected density closely approaching a theoretical one for a uniformly dense sphere. EDS line scans (Figure 5.3c) fully confirm such observations and demonstrate that both Fe and F are uniformly distributed within the C spheres. The relative ratio of all elements detected in the EDS spectra further confirms the pre-defined mass ratio of FeF_2:C in the

nanocomposite (note that due to a significantly higher molecular mass of FeF_2 than that of C, the atomic ratio of C:Fe should approach 2.6:1 for C:FeF_2 mass ratio of 1:3).

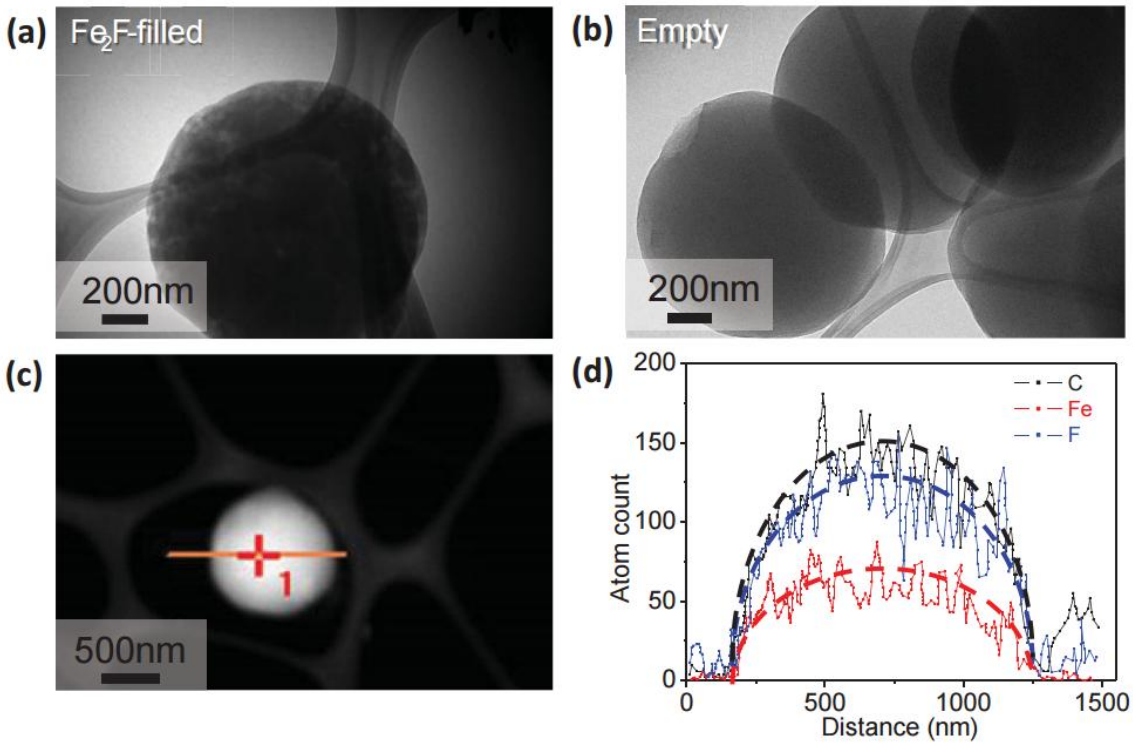

Figure 5.3 TEM characterization of FeF_2/C nanocomposites: TEM of a typical AC sphere a) filled with FeF_2 nanoparticles and b) empty. c) STEM images of AC sphere filled with FeF_2 nanoparticles. d) EDS line scan results, showing uniform distribution of Fe and F within a sphere. The line in (c) marks the trace of EDS detection. Note that (c) refers to an atomic count (not mass ratio).

The evolution of the crystal structure of FeF_2 with cell polarization in the first cycle was monitored *ex-situ* by X-ray diffraction (XRD) (Figure 5.4). The tested cells were polarized and kept at a series of voltages before opened for the XRD characterizations. A clear plateau is seen in the voltage profile of the first discharge (lithiation) process, which is located at around 1.6 V, (Figure 5.4a). The XRD spectra show a major change in the crystal structure of the electrode material below around 1.7 V. The major diffraction peaks occurred at 26.9 °, 33.1 °, 38.3 °, 51.5 ° and 55.2 °

corresponding to (110), (101), (111), (211) and (200) diffraction planes of FeF_2 diminish at this point, while the peak occurred at 45.2 ° and corresponding to $LiF_{(200)}$ and 45.0 ° for $Fe_{(110)}$ appear and their intensities continue to increase with deeper polarization (Figure 5.4b). Thus the observed plateau is assigned to the conversion type redox reaction between Li and FeF_2 into Fe and LiF. The overall intensity of all peaks, however, is low and the peak width is high due to very small size of the Fe and LiF crystal grains, as could be expected from prior studies. [163,177] We shall note that the overall discharge capacity of the nanoconfined FeF_2 (~500 mAh g^{-1}, Figure 5.4a) approaches 90% of a theoretical value, suggesting very high utilization of the active material enabled by its nanoconfinement within conductive carbon pores. Since we did not densify (calendar) the electrodes, slightly lower than theoretical value might be expected.

The capacity retention and rate stability of the nanoconfined FeF_2 was characterized by galvanostatic charge-discharge tests at room temperature (Figure 5.5). 1M $LiPF_6$/(DEC:DMC=1:1) with various amount of vinylene carbonate (VC) was used as the electrolyte. VC additives are known to assist in the formation of a stable SEI on anode surface. Since transition metal dissolution during cycling may negatively affect the SEI and since the overall cell performance is determined by both electrodes (FeF_2 cathode and Li anode), we were interested to observe its impact on the overall cell performance. High energy ball milled mixture of FeF_2 powders and carbon black (1:1) was used as a reference material. In the galvanostatic charge-discharge tests, all cells have been first polarized to 1.5 V in the initial cycle to complete the conversion reaction before the following tests.

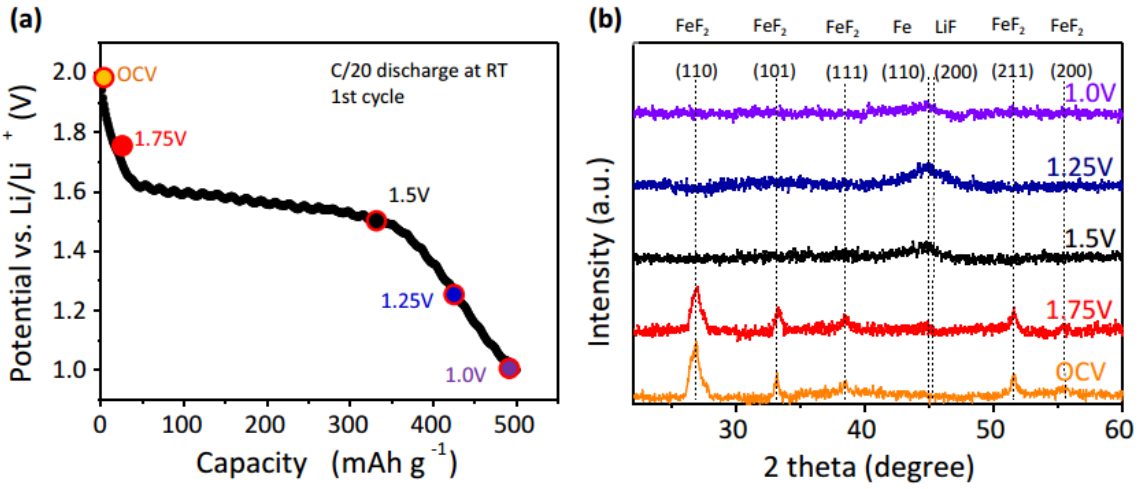

Figure 5.4 First cycle lithiation of nanoconfined FeF_2 : a) voltage profile of FeF_2/C nanocomposite electrode during discharge; b) *ex-situ* XRD spectra of FeF_2/C nanocomposite electrode at different voltage stages, corresponding to the points marked in (a) and showing structural changes.

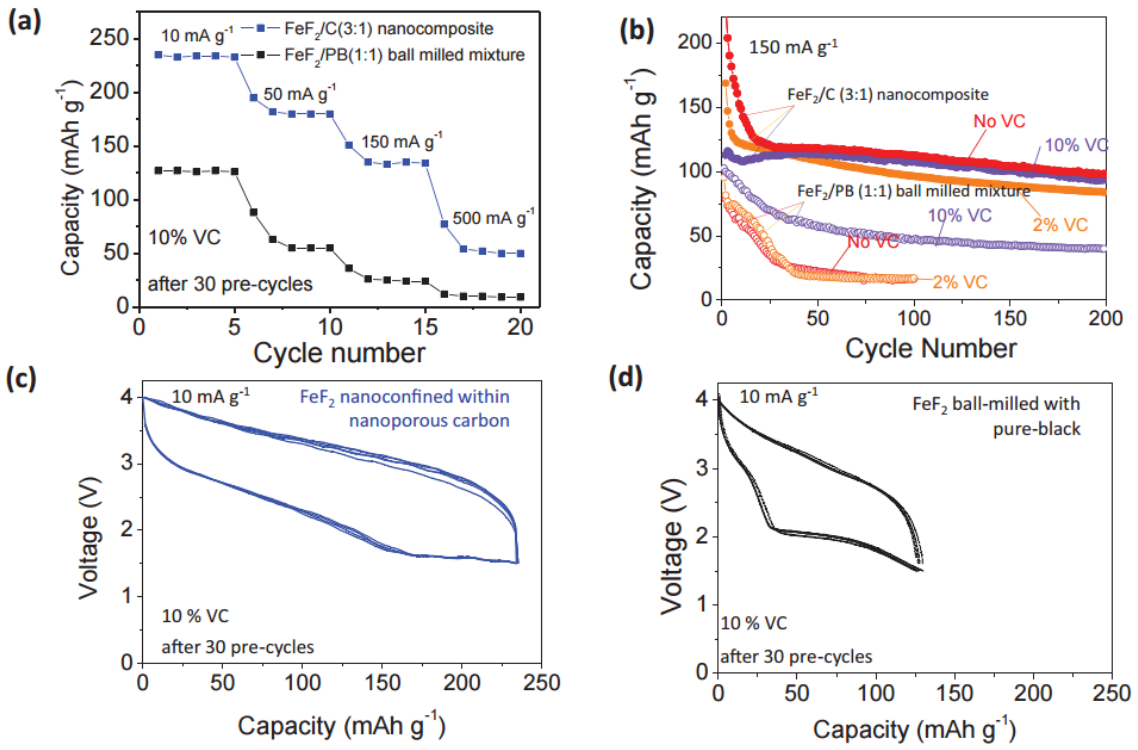

Figure 5.5 Electrochemical characterization of nanoconfi ned FeF_2 in comparison with a conventional ball-milled sample: a) rate stability tests; b) cycle stability tests of nanoconfi ned FeF_2 (solid marks) and ball milled FeF_2:PB (1:1) mixture (empty marks); and c,d) voltage profiles of the samples. Data in (a,c,d) are recorded after 30 cycles.

In order to reduce the impact of the initial capacity fading on the rate performance characterization of cells, all samples were pre-cycled for 30 cycles at 150 mA g^{-1} before cycling at different current densities. The electrodes are stable in this case and the effect of the current density can be de-coupled from the electrode fading. When compared to the ball milled sample, the nanoconfined FeF_2 maintains both a higher specific capacity and higher capacity retention at higher current densities, (Figure 5.5a). Specifically, increasing the current from 10 to 150 mA g^{-1} reduces specific capacity of the nanoconfined FeF_2 by ~ 40% in contrast to ~ 5 times reduction in the capacity of the ball milled sample. At such current the nanoconfined FeF_2 sample shows over 5 times higher capacity, which is quite remarkable because the ball milled sample contains 3 times more carbon in the electrode. While selected prior art studies in some cases showed higher capacities [177,178], these were achieved at significantly lower current densities and higher temperatures.

The cycle stability tests have been conducted at 150 mA g^{-1}. The results of such tests demonstrate that the nanoconfined FeF_2 is significantly more stable than the reference sample (Figure 5.5b). The initial discharge capacity of FeF_2/PB ball milled electrode is ~100 mAh g^{-1} and it quickly fades to below 20 mAh g^{-1} after 40 cycles. The rapid fading likely originates either from (i) the loss in electrical contact between fluoride material and conductive additive particles during volume-changing charge-discharge or (ii) unrestricted growth of the passivation layer on Fe particles (discharge reaction product), which prevents its reversible reaction with F of LiF. [165,179] On the contrary, the discharge capacity of FeF_2/C nanocomposite remains stable at ~120 mAh g^{-1} and after 200 cycles exhibits very moderate (for this system) 20% loss. The conversion reaction in

confined space defined by the micropores of carbon microspheres guarantees electron transport between phases after lithiation (LiF and metallic Fe) and also the contact in between active material and the conductive carbon matrix. In addition, it shall limit the expected passivation layer on the surface of active material to sub-nm dimensions.

The content of VC additives was found to impact only the initial 30 cycles. With VC-free electrolyte, the specific capacity of nanoconfined FeF_2 is initially higher (up to ~ 230 mAh g^{-1}), but in 30 cycles it drops to the same values as the one for VC-containing electrolytes. Since electrolyte composition in general and VC addition in particular, should not affect electrical conductivity of electrodes, we postulate that VC decomposition products passivate the surface of Fe and FeF_2 (as well as the surface of Li counter electrode) faster than other carbonates used (DEC and DMC). Indeed, VC additive in the electrolyte has been reported to enhance properties by forming a thinner but more stable solid electrolyte interphase (SEI) layer on the anode surface. [180-182] VC has also been reported to suppress the dissolution of metallic elements from the cathode material and re-deposition on the anode, by forming protective coatings during cycling. [183,184] In case of ball-milled sample electrodes, their slightly better stability of in VC-containing electrolytes might originate from: (i) a better protection of the lithiation products of FeF_2 from dissolution, (ii) improved stability of the SEI on a Li anode (since anode degradation also negatively affects the overall cell performance). The SEI that forms on the cathode may also block fresh solvent from undesirably propagating into the LiF/Fe interface, when smaller Fe particles are formed from FeF_2. [81] However, as we see from the observed fading, such a protection is clearly not sufficient for the ball-milled cathodes.

Somewhat to our initial surprise, the voltage profiles of nanoconfined FeF_2 exhibit a significant hysteresis (Figure 5.5c), comparable to that of the ball milled samples (Figure 5.5d). The slopping profile of the discharge curve from 4 to 1.6 V (above the conversion reaction plateau) is attributed to an intermediate phase (Li_xFeF_2), which accommodates Li ions via a reversible intercalation process, similar to the formation of Li_xFeF_3 observed at the initial stages of FeF_3 lithiation. [73] Interestingly, the ball milled sample exhibit significantly smaller capacity of such a phase (compare Figure 5.5c and 5d), suggesting that small active particle (Li_xFeF_2) size and its proximity to conductive carbon significantly favor its electrochemical activity. We postulate that a significant portion of the observed polarization (Figure 5.5c) originates from a LiF/Fe interface barrier layer, which forms during electrolyte decomposition. Due to the high surface to volume ratio of sub-4 nm (as defined by the carbon pore size, Figure 5.2c) FeF_2 nanoparticles, the contribution of such a layer to polarization might be significant.

In order to get more insights into the mechanisms of slow cell degradation, we conducted electrochemical impedance spectroscopy (EIS) studies of the electrodes over charge-discharge cycles and measured cell equivalent series resistances (ESRs). The Nyquist plots of the nanoconfined FeF_2 intact and cycled for 50, 100 and 150 cycles are presented in Figure 5.6a. The diameter of the semicircle for the fresh electrode in the medium frequency region is 200 Ohms, but it grows by ~two times to 450 Ohms after 150 cycles. The size of the semicircle corresponds to the combined effect of the electrode charge-transfer impedance and the electrode/electrolyte interphase (SEI) resistance, assuming that such components are small for the Li counter-electrode. As previously

discussed, the charge-transfer impedance for our conversion process may also be impacted by the SEI barrier film formed on the Fe surface.

When looking at the changes in the shape of the charge-discharge curves (Figure 5.6b) we find more evidence that growing polarization is the major cause of the slow capacity fading in cell cycled within a fixed 1.5-4V voltage range. Indeed, the activity of the Li_xFeF_2 phase even increases with cycling, as evidenced by the larger capacity of the slopping discharge region (Figure 5.6b). Growing activity may originate from the improved Li ion conductance within individual spheres when repeated volume changes form lower resistance ionic channels. At the same time, the increasing polarization (as evidenced by the hysteresis growth) shifts the conversion reaction to lower voltage, thus reducing total accessible capacity. We propose that a significant portion of such polarization may originate from building a physical barrier (SEI) at the interphase between Fe and LiF, which would slow down their reversible reaction of F upon Li extraction from LiF. In order to overcome this degradation mechanism our future studies will focus on investigating efficiency of various Li ion permeable (solvent impermeable) shells around the particles. In addition, the use of the proposed approach will allow us to systematically investigate the impact of electrolyte components on the properties of the passivating SEI.

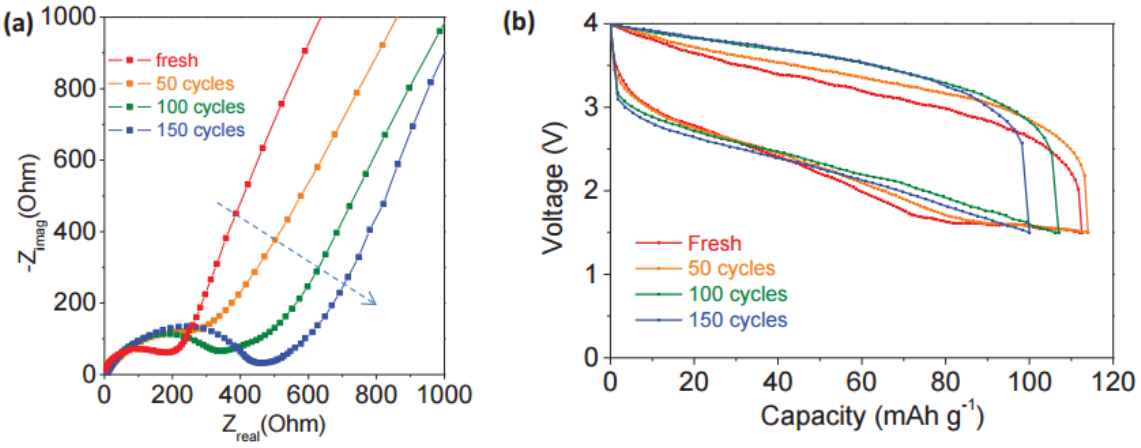

Figure 5.6 Electrochemical studies of nano-confined FeF_2 during a cycle stability test: a) Nyquist plots of intact electrodes and those after 50, 100 and 150 cycles and b) voltage profiles of intact electrodes and those after 50, 100, and 150 cycles. The electrolyte is 1 M $LiPF_6$ /(DMC:DEC) with 10% VC as additive.

5.4 Summary

In summary, we have demonstrated that a simple method of vacuum impregnation of micro/mesoporous carbons with a MF precursor and the precursor subsequent transformation into MF allows one to produce uniform nanocomposites, where MF nanoparticles are evenly distributed within the carbon matrix and their maximum size is determined by the size of the largest pores present in carbon. We have further demonstrated that nano-confinement of metal fluorides, such as FeF_2 within carbon nanopores allows formation of FeF_2/C nanocomposites with high fraction of FeF_2 and attractive performance characteristics when tested as cathodes in Li batteries with Li counter electrodes. More specifically, at a slow C/20 rate the produced FeF_2/C composites demonstrated specific capacity approaching 90% of their theoretical value. Their rate performance significantly exceeded that of the FeF_2 ball milled with carbon in spite of the three times higher carbon content of the later. Cycle stability tests conducted

at a high current density of 150 mA g^{-1} demonstrated over 80% reversible capacity retention after 200 cycles. The small degradation observed was found to be caused by the growing polarization, which, in turn, was linked to electrolyte decomposition on the surface of active particles. The excellent rate performance and capacity retention of nanoconfined FeF_2 (compared to the similar fluoride based materials reported in previous works [67,185-187]) can be attributed to the small size of the FeF_2 nanoparticles and the use of conductive carbon as confinement media. The Fe nanoparticles formed in the lithiation process are partially protected by the carbon matrix from exposure to the electrolyte, which limits the thickness of the SEI that forms and commonly grows rapidly during cycling. [165] Finally, nano-confinement of FeF_2 greatly reduced the dissolution of fluorides during cycling and Fe precipitation on the Li anode. The simplicity of the suggested synthesis route and its efficiency in producing very uniform nanocomposite powders suggest its promises for both fundamental studies of the MF interactions with various electrolytes and potential industrial applications.

CHAPTER 6

IMPROVED ELECTROLYTE FOR METAL FLUORIDE BASED CATHODE WITH POROUS CARBON SCAFFOLD

6.1 Introduction & Motivation

The rapidly growing markets of electric ground, sea and aerial vehicles, energy-efficient industrial tools and portable electronic devices demand lighter, smaller and cheaper rechargeable batteries. Conversion-type lithium cathode chemistries are attracting more recent attention due to their lower cost, higher capacities and greater safety characteristics [188]. Sulfur-lithium (S-Li) cells have already been used in unmanned air vehicle applications [189] and now become one of the most extensively studied chemistries. Metal fluoride-lithium (MF-Li) cells exhibit theoretical energy density higher than S-Li, while offering additional attractive features [63,163,190-192] ENREF_3 ENREF_3. Both fluorine and many metal elements are more abundant than S. For example, iron (Fe) is 130 times more abundant in the Earth's crust than S. While FeF_2 does not offer the highest theoretical potential and volumetric capacity among various MFs [68], it still "beats" S. Indeed, in the lithiated state it offers 2002 mAh/cc (vs. 1935 mAh/cc for S) approaching that for pure Li (2060 mAh/cc), while its theoretical Li extraction potential is 0.3 V above that for S.

In spite of their theoretically attractive features, MF cathodes also suffer from multiple limitations. For example, due to the large band gaps induced by the strong ionic character of the metal-halogen bonds, MFs exhibit notoriously poor electronic conductivity [193]. As such, to attain high capacity even at a slow rate, MFs are commonly

mixed or ball milled with high content of conductive additives _ENREF_7[80,194-197] _ENREF_7. In some cases near theoretical capacity has been achieved during the first cycle, although at elevated temperatures of up to 70 ℃[198-200] _ENREF_5. Several recent approaches by other groups involved formation of _ENREF_6 _ENREF_5 100-1000 nm FeF_2 rods inside carbon nanotube (CNT) shells via co-pyrolysis of ferrocene and NH_4F [201] or wet-chemistry deposition of 50-200 nm FeF_3 particles on the CNT surface [73] in order to achieve higher capacity with the reduced carbon content. But in spite of these efforts, the majority of the previous works showed limited capacity achieved at room temperature (commonly < 40 % of theoretical).

Another serious limitation observed in MF-Li cells is rapid degradation. Indeed, prior-art studies commonly show either only a few (20-50) cycles or demonstrate noticeable capacity fading within 100 cycles [196,198,201,202]. While the origins of the observed degradation make a subject of scientific debates, several mechanisms could be proposed. Firstly, metal (M) nanoparticles produced during lithiation of MF exhibit large surface energy when in contact with LiF due to the mismatch in their bonding nature (metallic bonds in M vs. ionic bonds in LiF). which results in large charge discharge voltage hysteresis and therefore low energy efficiency[63]. In addition, the significant volume changes occurring during the conversion reaction [203] [81] may induce mechanical degradation of the electrode. Second, the catalytic effect of metal nanoparticles on the decomposition of cyclic carbonate solvents [165,179] may induce formation of a passivating layer at the interface between the M and LiF, similarly leading to capacity fading. Finally, conventional lithium battery electrolyte, composed of $LiPF_6$ in carbonates, produces free

protons *via* undesired electrolyte decomposition[204], which may contribute to MF dissolution during cycling.

FeF_2-Li cells reported in this study demonstrate a major progress in overcoming the discussed above limitations. We chose a holistic approach, in which we addressed the cell performance by (i) selecting a rational architecture for the structurally robust FeF_2-C nanocomposites, (ii) employing *in-situ* formation of the effective protective shells around the composite cathode particles that prevent their discovered dissolution and (iii) identifying cell chemistry that reduces Li dendrite growth to the undetectable level.

6.2 Materials & Methods

Raw chemicals including LiFSI (> 99.9%, Suzhou Fluolyte Corp.), DME (anhydrous, 99.5%, Sigma Aldrich), H_2SiF_6 (25% aq. sol., Sigma Aldrich), Fe powder (>99.9%, Sigma Aldrich) were used as received. For the formation of porous carbon spheres we first synthesized polydivinylbenzene spheres by using precipitation polymerization carbonized the polymer produced carbon spheres and activated them to increase carbon porosity. Prior to carbonization, polymerized spherical polydivinylbenzene powder was stabilized in air at 300 ℃ for 3 h. Activation was conducted in a CO_2 gas at 950 ℃ for 5 hours, similar to the procedure previously used by our group and others.

For electrode preparation we used 15 wt. % PVDF binder and Aluminum foil current collector. No conductive additives were added. After casting, the electrode was dried in vacuum at 100 ℃ for 8 h to evaporate the solvent. The electrode was then assembled against metallic Li which was applied as counter electrode in type 2032 coin

cells. The electrolytes used in these coin cells were prepared by dissolving various molarities of LiFSI or LiTFSI in DME solvent.

The ionic conductivity of the electrolytes were measured by a simple test set-up which is consisted of insulating teflon block and L-shaped Al plates. The distance between the Al plates is well defined by the thickness of the teflon block as L = 0.7cm. The L-shaped Al plates are applied as conducting probes. The inner sides of the Al plates were polished for good conductivity, while the outer sides were insulated by resin coatings. The area of Al plates exposed to the electrolyte is A = 0.15cm^2. The test set-up was immersed in the electrolyte and conducted with constant current. The voltage between the two probes were recorded, and the conductivity of the electrolyte was calculated following Ohm's Law: $\sigma = \frac{L}{A} \cdot \frac{I}{V}$

Galvanostatic charge-discharge test was performed using an Arbin galvanostat/potentiostat (USA). After 200 charge-discharge cycles, the cells were carefully cut open inside the glovebox and post-mortem XPS (Thermo K-Alpha) characterizations were performed on surfaces of both electrodes to identify the composition of the SEI. Another batch of coin cells with stainless steel (ss) plates as working electrodes were made for cyclic voltammetry test. The stainless steel plates were assembled against metallic Li foil and scanned at 1 mV s^{-1} between 1.5V-4.0V (Solatron).

The morphology of the nanocomposite electrodes and Li foils before and after charge-discharge cycling were recorded by scanning electron microscopy (SEM, LEO 1550, Netherland) and tunneling electron microscopy (TEM, JEOL 100CX, Japan). To remove electrolyte salt residues, the SEM samples were thoroughly cleaned by DME solvent with ultra-sonication for 1h. The crystal structures of materials were characterized

by X-ray diffraction (X'Pert PRO XRD, Alpha-1). Gas sorption-desorption isotherms were collected at 77K using Tristar gas sorption and surface area analyzer (Micromeritics, USA).

6.3 Results & Discussion

Figure 6.1 schematically shows synthesis steps involved in the composite fabrication. We start with the formation of activated carbon (AC) powder with high specific surface area (~3200 m^2 g^{-1}) and pore volume (~1.4 cc g^{-1}), according to the procedure described in the experimental section and previously employed by our group [203]. The second step involves infiltrating porous carbon with an aqueous solution of $FeSiF_6$ (FeF_2 precursor) using a simple vacuum-infiltration setup (Figure 6.1b), followed by water evaporation (Figure 6.1c). In order to warrant $FeSiF_6$ precipitations within the carbon pores only (and thus prevent their nucleation and growth on the outer surface of the particles), while achieving high particle-to-particle uniformity, it is critical to satisfy several criteria. First, the carbon should be sufficiently hydrophilic to warrant complete pore wetting by the precursor solution. Second, in order to achieve nearly identical fraction of FeF_2 in all individual carbon particles, the total amount of the precursor solution should be identical or slightly larger than the total carbon pore volume. Finally, when the precursor solution amount is slightly larger and some solvent evaporation is needed to accommodate all of the solution volume within the pores, it is critical that the concentration of $FeSiF_6$ does not exceed the solubility limit before capillary forces pull all the liquid into the pores. The final step involves conversion of $FeSiF_6$ into FeF_2 nanoparticles and SiF_4 gas during heat-treatment at ~ 240 ℃ (Figure 6.1d). In order to increase the FeF_2 loading, the infiltration and conversion steps could be repeated.

The FeF_2-C composite particles produced according to such a process flow (Figure 6.1e) may offer the following advantages: (i) high electrical conductivity due to small distance between the active material and pore walls (Figure 6.1d), (ii) excellent mechanical stability due to porosity available for accommodating the volume expansion and due to excellent mechanical properties of carbon [203,205] , (iii) better protection from surface passivation and (iv) resistance to segregation due to the confinement of FeF_2 nanoparticles within the small carbon pores. In addition, the process is simple, scalable and requires low temperature, low-cost solvent (water) and inexpensive precursors.

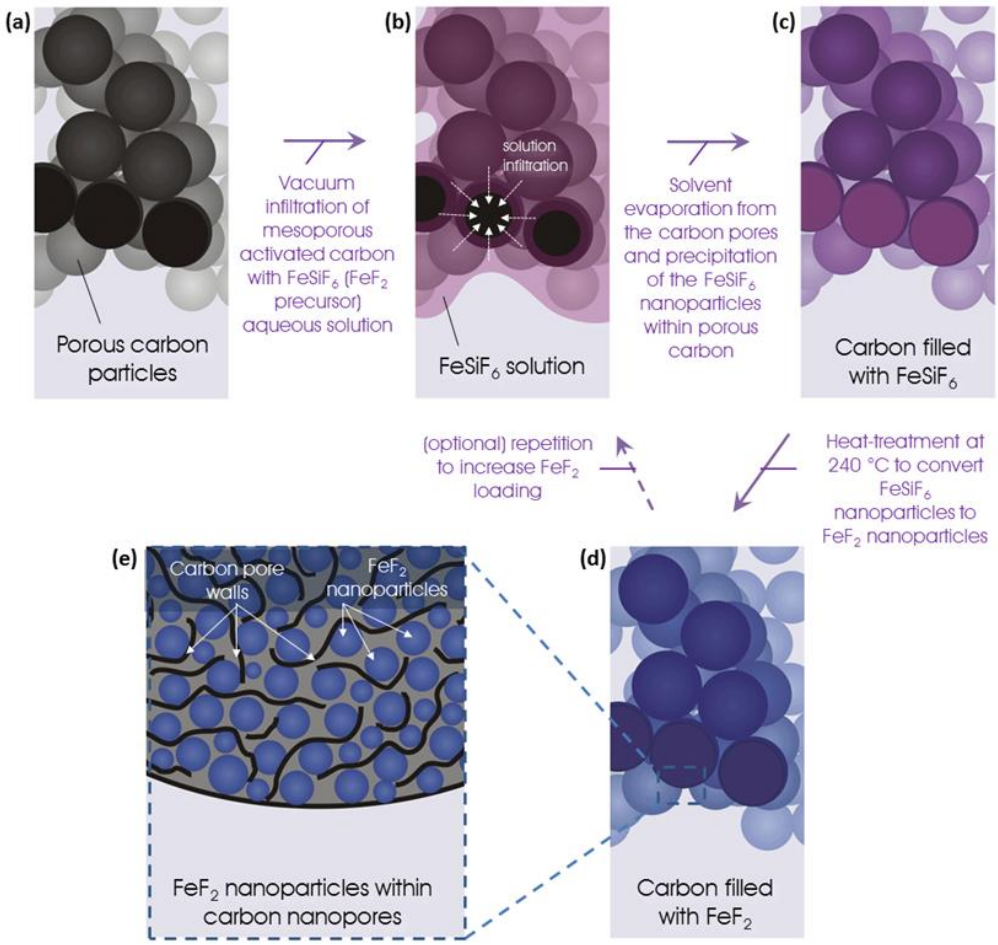

Figure 6.1 Schematic of the synthesis procedure of FeF_2-C nanocomposites

Figure 6.2 compares the morphology of the AC spherical powder before (Figure 6.2a, b) and after (Figure 6.2c, d) infiltration with FeF_2. The average size of the individual particles is ~ 1 μm. The majority of pores within AC are distributed within 1-4 nm (Figure 6.2a, inset). As a result, less than 2 nm separation distances exist between the center of FeF_2 and conductive pore walls, which permits quantum mechanical tunneling of electrons to/from electrochemical reaction sites[206]. Carbon microstructure is highly disordered, as shown in a high resolution TEM micrograph (Figure 6.2b, inset). The smooth surface of the FeF_2 infiltrated AC particles (Figure 6.2c) indicates a good efficiency of our synthesis procedure, where no nanoparticles present outside the carbon pores. X-ray diffraction (XRD) detects the presence of FeF_2 nanoparticles and the lack of any crystalline impurities (Figure 2c, inset), while energy dispersive spectroscopy (EDS) only detects the presence of Fe, F, C and very small amount of O (less than 1 %) residues in the samples. The high contrast low-resolution TEM micrograph further confirms the infiltration of FeF_2 within the AC spheres.

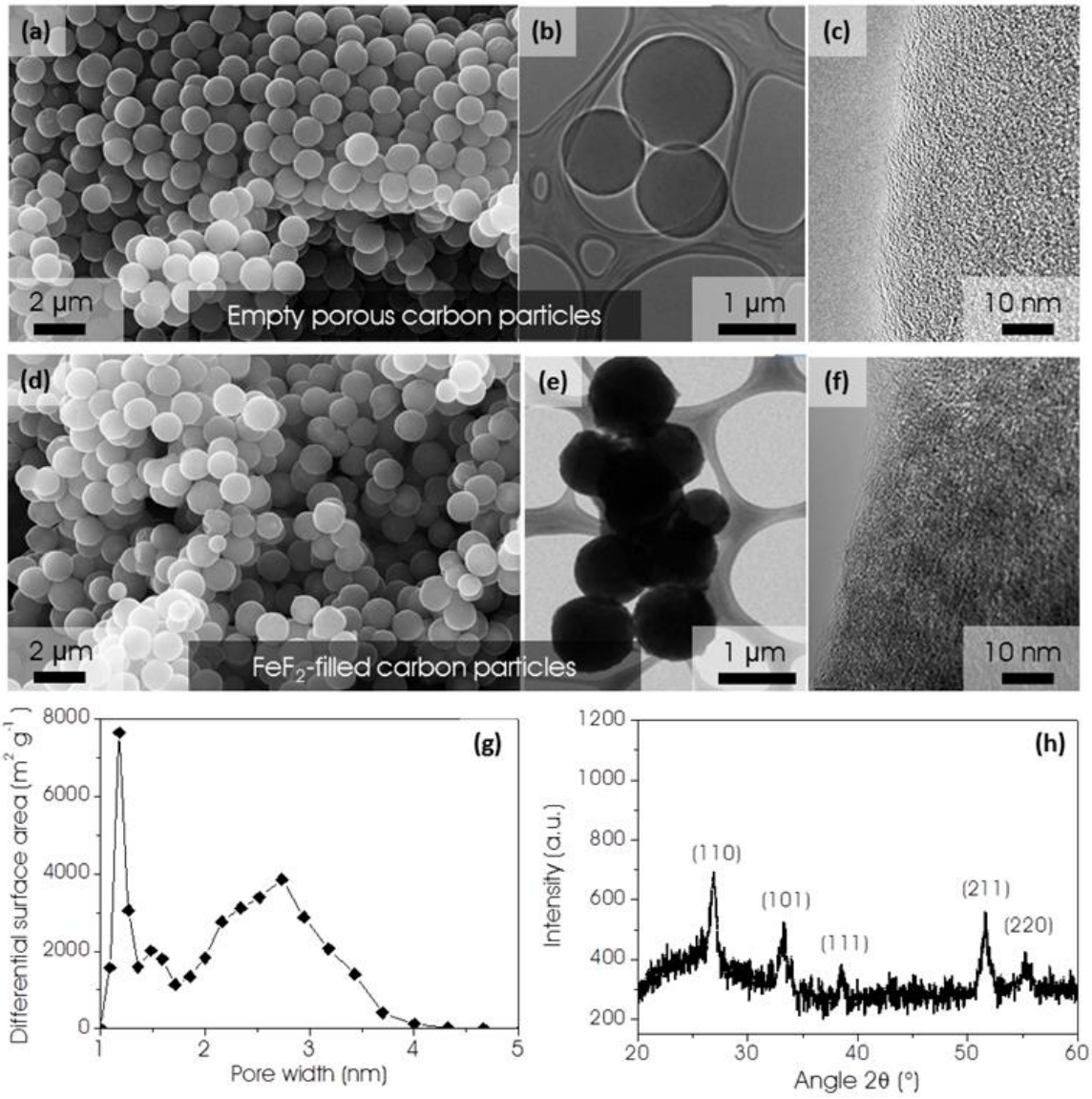

Figure 6.2 Structural characterization of the produced materials: SEM and TEM micrographs of porous carbon spheres before (a, b, c) and after (d, e, f) filling with FeF_2 to produce uniform nanocomposites; (g) pore size distribution of the porous spheres, showing its high mesopore volume; (h) X-ray diffraction of the composite, showing the presence of FeF_2 nanocrystals and the lack of crystalline impurities.

Figure 3a shows the room temperature discharge curve of the FeF_2 nanoparticles within AC pores, revealing very high capacity utilization in the first discharge. Somewhat similar to some other conversion materials[74,77], the first discharge cycle of metal fluorides are known to exhibit significant over-potential (Figure 6.3a), the origins of which are still unclear, but could be related to multiple factors, such as (i) the energy barrier originating from forming new interfaces or (ii) disruption of the FeF_2 crystal structure or (iii) initial plastic and elastic deformations within the system (which could be reduced after the irreversible changes accompanying the first volume expansion), to name a few. As a result, the first conversion reaction takes place at a relatively low potential of ~ 1.5 V and involves significant irreversible capacity losses (Figure 6.3a), which could be related to various undesirable side reactions. For example, as we will later demonstrate, this initial conversion reaction induces substantial cathode dissolution (likely as both LiF and Fe^{2+} ions) and re-precipitation of some of the dissolved species (such as Fe) on the surface of Li anode. This finding contradicts the common belief on the stability of this cathode against dissolution [207].

In this study we were interested to investigate if electrolyte reduction taking place at the potential above that of the initial conversion reaction (above ~ 1.5 V) may induce formation of the protective layer, which would resist undesirable reactions between liquid electrolyte and discharged cathode components (such as freshly produced LiF and Fe). We were also interested to see if formation of such a protective layer may impact the first cycle hysteresis. Recently, we discovered the ability lithium bis(fluorosulfonyl)imide (LiFSI) salt – based electrolyte to induce formation of the ionically conductive layer on the S cathode surface at elevated potentials[208], which noticeably improved stability of the

Li-S cells. Additional advantages of LiFSI over $LiPF_6$ include its higher conductivity in electrolytes and the dramatically reduced formation of acidic matter (such as HF) during decomposition $LiPF_6$[208-211].

Figure 6.3b shows cyclic voltammetry of a bare stainless steel (ss) foil vs. a Li counter electrode cell in LiFSI/ dimethoxyethane (DME) electrolytes having different salt concentration. Interestingly, at higher salt concentration we observe a noticeable increase in the intensity of the reduction peak at ~1.8 V vs. Li/Li^+. The area under the anodic current curve is becoming significantly larger than that of the cathodic curve for higher salt content with coulombic efficiency (CE) reducing from 98 to 87 and 56%, respectively. These results indicate irreversible electrolyte reductions with the likely formation of the solid electrolyte interphase (SEI) on the ss surface. Because the position of this reduction peak is sufficiently high (> 1.6 V) and because our further studies confirmed the produced SEI to passivate the foil surface with continuous cycling (Figure 6.3c), we selected LiFSI/DME system for systematic studies.

Our very initial experiments revealed that both the overpotential for the first discharge and the first cycle irreversible capacity loss reduced dramatically in high molarity electrolyte (Figure 6.3d). Since the electrodes in these experiments are identical we conclude that the reduced hysteresis in the modified electrolyte likely originates from the reduced energy barrier associated with lower electrolyte/electrode interfacial energies. Since electrolyte reduction is more significant in high molarity electrolytes (Figure 6.3b), the reduced losses are likely linked to the reduced cathode dissolution. As will be later discussed, post-mortem analysis also supported this hypothesis.

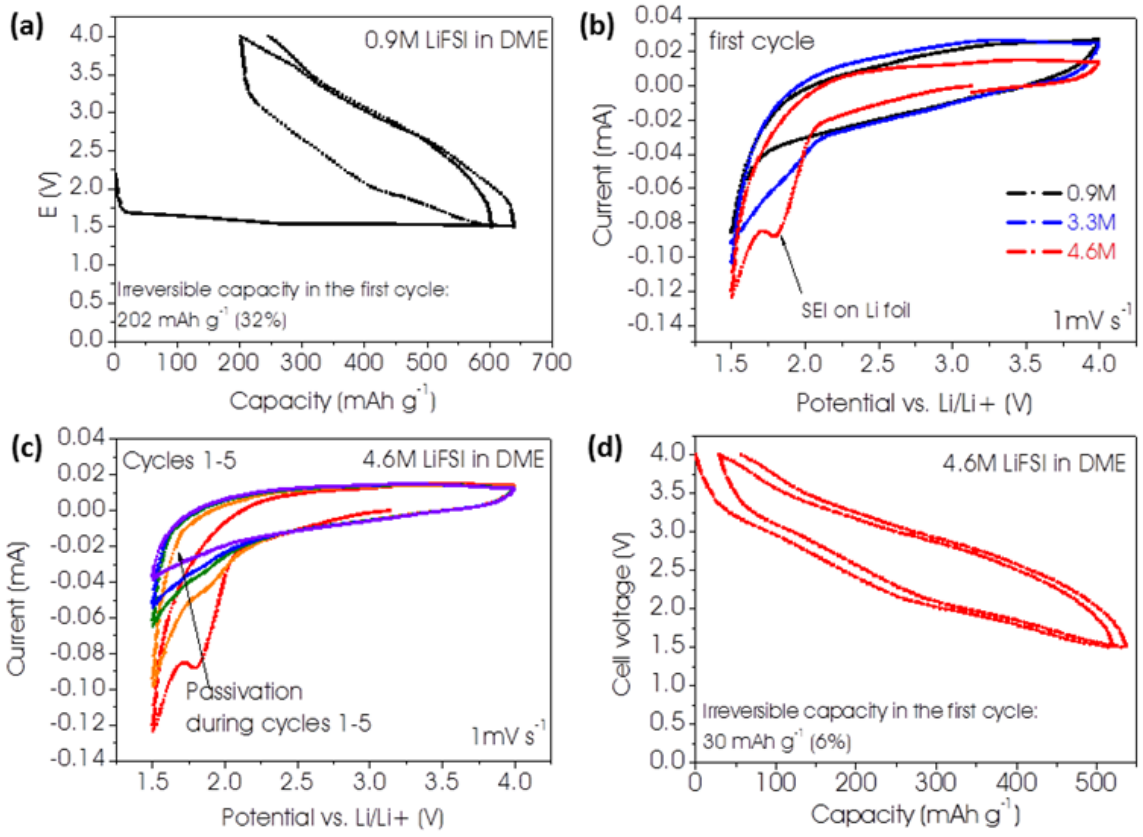

Figure 6.3 Selected electrochemical tests: (a, d) The charge and discharge profiles of the nanocomposite FeF_2/C – Li cells in 0.9M and 4.6M LiFSI in DME during the initial 2 cycles; (b) The first cycle cyclic voltammetry of the nanocomposite FeF_2/C – Li cells in 0.9M, 3.3M and 4.6M LiFSI in DME; (c) The changes in the cyclic voltammetry diagrams of the nanocomposite FeF_2/C – Li cells in 4.6M LiFSI in DME.

In order to investigate efficiency of the high molarity electrolytes to stabilize FeF_2-Li cell chemistry we have conducted cycle stability tests. Figure 6.4 shows results of the charge-discharge tests conducted at a moderately high (for this system) current density of 140 mA g^{-1}. While increasing electrolyte molarity from 0.9 to 3.3M had a very minor impact on capacity stabilization, the highest molarity electrolyte (4.6 M) exhibited noticeably improved performance. This improvement correlates with noticeably increased reduction of this electrolyte at potentials below 2.1 V vs. Li/Li^+ (Figure 6.3b). Since many applications of high energy cells require cycle stability in the range from 200 to 1000 cycles, we conducted the long-term cycle stability test of the most promising cell (Figure 6.4b). The achieved combination of the outstanding (for metal fluorides) stability and high capacity utilization at high current density is unprecedented. As we see, even some of the best prior-art studies of similar chemistry demonstrated 2-3 times lower capacity in spite of the lower current densities used (Figure 6.4b).

In contrast to our initial expectations the cell with high molarity electrolyte exhibited smaller hysteresis (the difference of discharge and charge voltages) than the 0.9M cell (compare Figure 6.4c and d). Li insertion into FeF_2 are generally believed to be divided into two steps: initial intercalation (high voltage sloping plateau at ~3V, best visible in Figure 6.3a and 3d collected at a lower current density) followed by the actual conversion reaction (lower voltage plateau at ~2V). [212] The capacity of the conversion reaction of the 0.9M cell fades rapidly, which reduces its charge-discharge voltage hysteresis (Figure 6.4c). In contrast, the 4.6 M cell retains capacity of both reactions well. After the initial capacity fading, the cell stabilizes. The average charge and discharge voltages (calculated by dividing the integral of the area beneath the voltage curve with

the total capacity) of the 4.6 M cell remain constant with cycling (Figure 6.4e). More importantly, the average overpotential in this cell is 0.1-0.2V smaller than that in 0.9 and 3.3M cells. Considering the higher ionic resistance of 4.6 M electrolyte, the smaller charge transfer resistance of the 4.6M cell may explain the observed phenomenon. The ~0.5 V hysteresis observed in the best cell at 140 mA g^{-1} is certainly larger than what typically observed in intercalation-type materials at similar current densities (0.05-0.2 V), but noticeably smaller than what was achieved in prior art studies of metal fluorides at room temperature and comparable (or even lower) currents (0.6-1.5 V) [63,201]. As a result, the average discharge voltage of all our cells (2.2-2.4 V) is significantly higher than what was reported in the prior art studies. The rate performance of the cells was also very promising for this cell chemistry (Figure 6.4f).

Comparison of the surface morphology of the cathodes before and after charge-discharge cycling reveals a dramatic impact of electrolyte salt concentration (Figure 6.5a-d). Homogeneous organic coatings were observed on the surface of all electrodes, but the highest electrolyte molarity of 4.6M resulted in the formation of significantly surface layer formed (compare Figure 6.5b and d), consistent with the large reduction peak of this electrolyte observed in CV tests (Figure 6.3b, c). This solid layer of reduced electrolyte, evidently conductive for Li ions (Figure 6.4), may have acted as a barrier for cathode dissolution, which may explain excellent long-term stability of the 4.6M cell (Figure 6.4b).

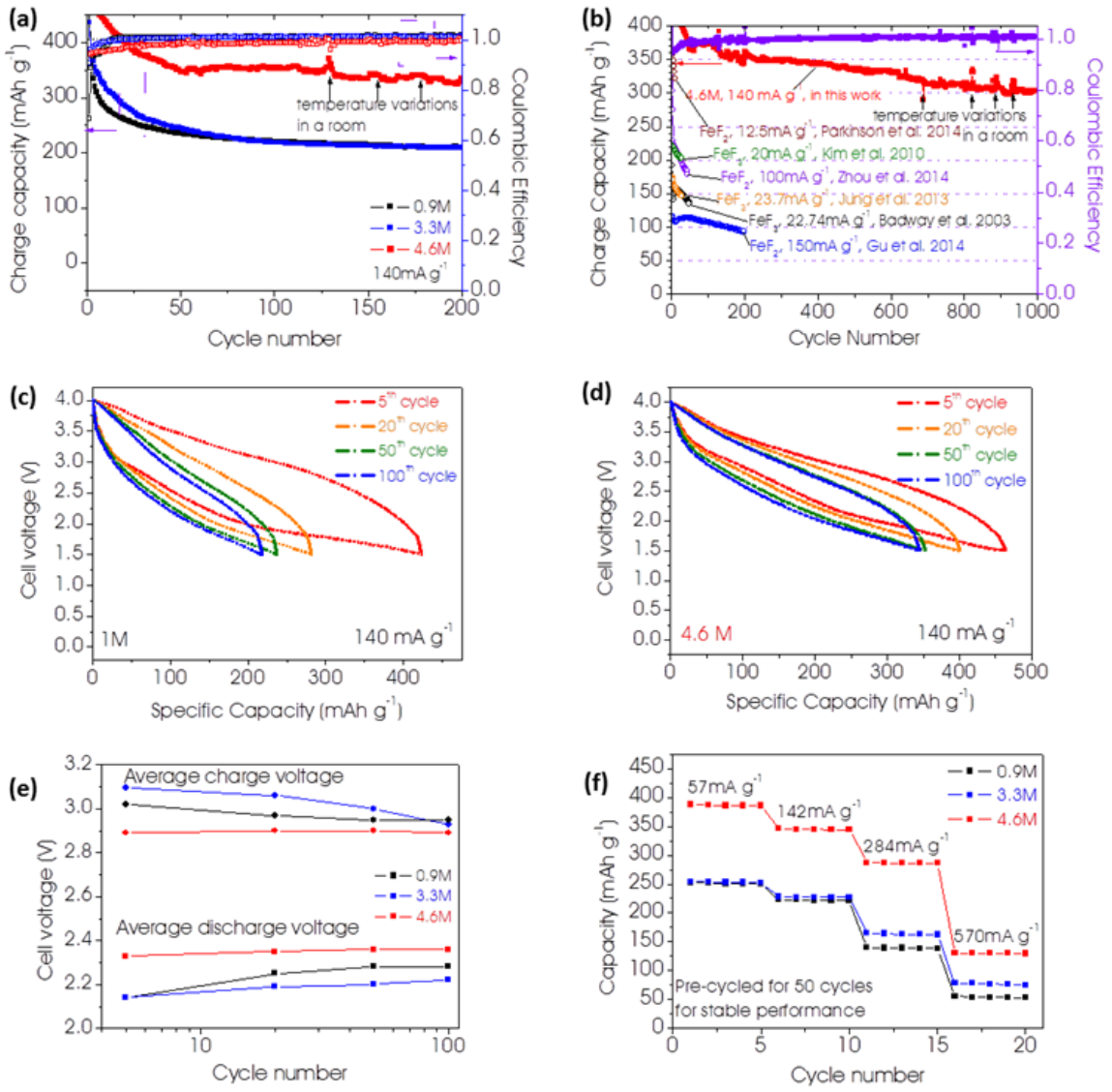

Figure 6.4 Cycle stability and rate performance tests on the produced cells: (a) Charge capacities and coulombic efficiencies of nanocomposite FeF_2/C – Li cells in 0.9M, 3.3M and 4.6M LiFSI in DME; (b) Charge capacity and coulombic efficiency of nanocomposite FeF_2/C – Li cells in 4.6M LiFSI in DME for 1000 cycles. Previously reported performances of FeF_2 based cathode materials are provided for comparison; (c,d) Charge-discharge profiles of nanocomposite FeF_2/C – Li cells in 0.9M and 4.6M LiFSI in DME during 5^{th}, 20^{th}, 50^{th}, and 100^{th} cycles; (e) Average charge and discharge voltages of nanocomposite FeF_2/C – Li cells in 0.9M, 3.3M and 4.6M LiFSI in DME during the first 100 cycles; (f) Charge capacities of nanocomposite FeF_2/C – Li cells in 0.9M, 3.3M and 4.6M LiFSI in DME at 57, 142, 284 and 570 mA g^{-1}.

To examine the chemical nature of the surface coatings, we performed X-ray photoelectron spectroscopy (XPS) characterization of the cycled FeF_2/C nanocomposite cathodes (Figure 6.6).The major peak of the C_{1s} spectra (Figure 6.6a) at 285eV is attributed to C-C bonds from AC spheres, and -CH_2-CH_2- bonds from polymerized DME. At higher electrolyte concentration, the C-F peak attributed to PVdF binder at 290.5eV is diminished, which is due to the much thicker layer of the reduced electrolyte. The peak at 286.4eV corresponding to C-O-C bonds from polymerized DME intensifies with increasing salt concentration, as expected from more vigorous DME polymerization at the cathode surface with higher concentration electrolyte (Figure 6.5d). We also observe a C=O peak at higher electrolyte concentrations, which may originate from the breakdown of the backbone chain of DME monomers. The O1s spectra (Figure 6.6b) confirmed the appearance of C=O peak at high electrolyte concentration. The major peak at 532.4eV is assigned to O-C bonds in DME and O=S in LiFSI and its reduction products such as $LiNSO_2$ and $LiFSO_2$ F1s spectra shows dampening of the LiF peak at 685eV and rise of the F-S peak at 687.8eV (Figure 6.6c). In this process, a large fraction of the LiF detected could be contributed to the lithiation of FeF_2. The reduced LiF/F-S ratio with increase in the electrolyte concentration indicates thicker surface layer blocking the signal from the cathode core. Finally, with the increase in the electrolyte concentration, peaks representing FSI^- (170.1eV and 171.4eV) and its decomposition products (167.1eV) are increasing in S_{2p} spectra (Figure 6.5d), as shall be expected for thicker surface layer.

Other interesting and very promising results were obtained when studying the surface morphology of Li foil cycled in the described cells. Long-term plating and

striping of Li onto/from the Li foil is known to induce severe surface roughening and dendrite growth, which presents cell safety hazard [213-216] _ENREF_43. This is one of the key reasons bare Li foils are not used in commercial cells. In contrast, the surfaces of Li foils cycled in our cells are remarkably smooth (compare Figure 6.7a with Figure 6.7b-d), particularly the one cycled in the 4.6 M electrolyte (Figure 6.7d). Clearly, the surface layer of reduced electrolyte prevented the dendrite growth. We propose several possible explanations. Firstly, decomposition of LiFSI on the surface of both electrodes induces formation of LiF [208,217,218], which was recently proposed to result in a stable Li electrodeposition due to increased Li surface energy in LiF comprising electrolytes[219]. Secondly, electrolyte composition itself may similarly prevent Li dendrite growth and smooth out the Li surface due to expectedly high energy of the interface between the Li and LiFSI/DME electrolyte, particularly at high salt concentrations. [216] Thirdly, elastic modulus and hardness of the Li SEI could be sufficiently high to provide additional resistance to the growth of dendrites. We shall note that the composition of the surface films on the cathode (Figure 6.6) and anode surfaces are similar. The high ionic transport through such surface layer, as evidenced by low polarization during cycling of a symmetric Li-Li cell[208] as well as by low polarization of our FeF_2-Li cells (Figure 6.4d), shall similarly lead to large improvements in the stability of Li electrodeposition [219]. Finally, the majority of traditional intercalation cathodes comprise Mn, Ni and Co, the leaching of which into electrolyte is known to induce damages within the SEI [220]. In contrast, the small dissolution of our cathode shall introduce LiF into electrolyte, which is advantageous for Li dendrite growth prevention, and Fe species, which we propose induces less SEI damage.

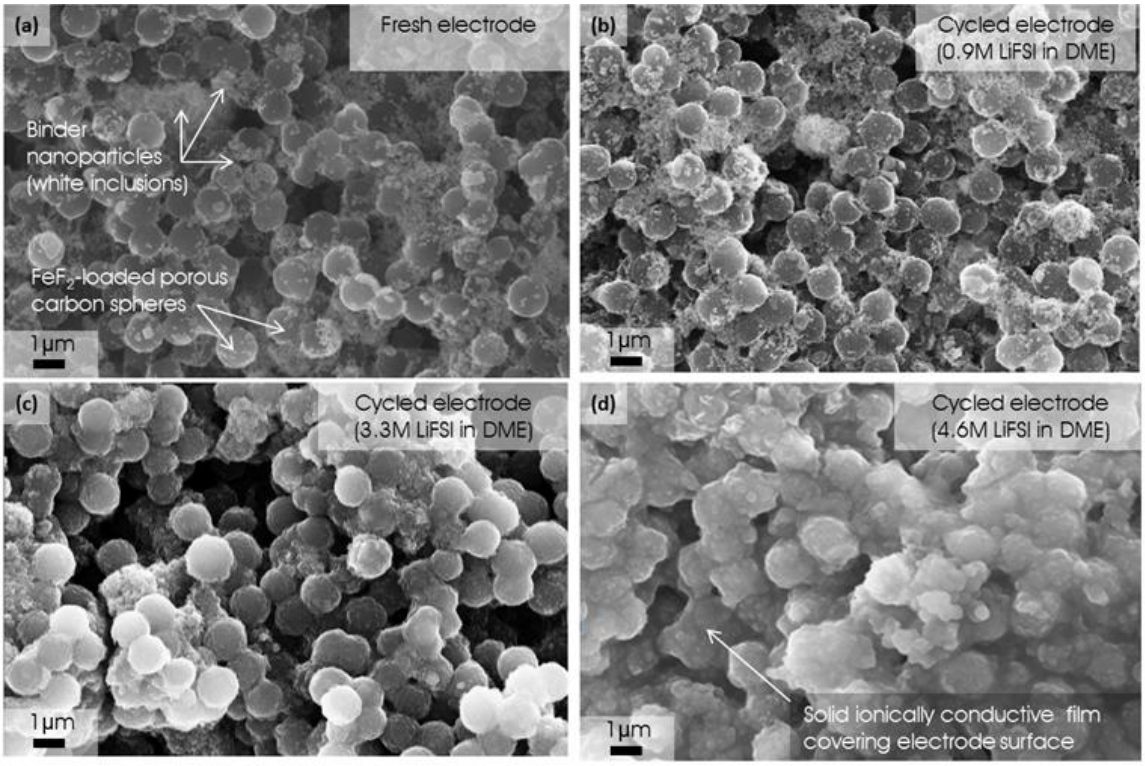

Figure 6.5 SEM micrographs of the nanocomposite cathodes (a) before and (b-d) after charge-discharge cycling in 0.9, 3.3 and 4.6M LiFSI/DME electrolytes.

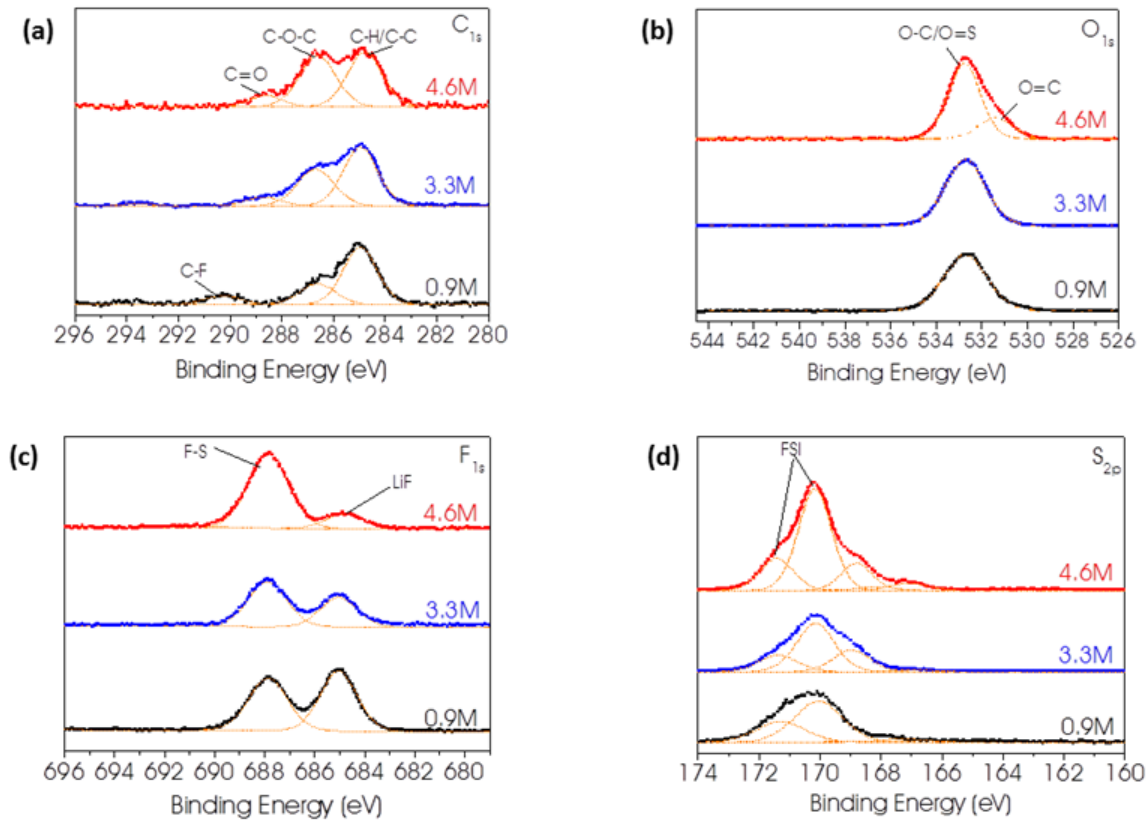

Figure 6.6 High resolution XPS spectra of FeF_2/C nanocomposite cathode cycled in 0.9M, 3.3M and 4.6M LiFSI/DME electrolytes: (a) C_{1s}; (b) O_{1s}; (c) F_{1s}; (d) S_{2p}.

Chemical analysis of the cycled Li surface detects the presence of significant Fe content in cells cycled in 0.9M electrolyte (Figure 6.7e), fully supporting our hypothesis on cathode dissolution. In contrast, Li from cells with high salt content did not contain detectable amount of Fe. Here we would like to emphasize that the presence of this Fe evidently does not induce significant dendrite growth (Figure 6.7b), in contrast to the significant negative impact of Mn, Ni and Co [220].

Quantum chemistry (QC) calculations provided additional insights on the mechanisms of film formation and reduced cathode dissolution (Figure 6.8). Previous QC studies[217,218] indicated that the LiFSI reduction potential is dependent of the FSI^- anion

environment. For example, the reduction potential of LiFSI in contact with DME is ~1.6 V vs. Li/Li^+, while reduction potential of $(LiFSI)_n$ aggregates is significantly higher, ~ 2.3 V vs. Li/Li^+. Molecular dynamics (MD) simulations revealed no LiFSI aggregation in 1 M DME(LiFSI) electrolytes.[216] Extensive aggregates, however, were found in the highly concentrated DME:LiFSI=1:1 electrolyte. These aggregates consisted on average of one Li^+ being surrounded by 2.5 O of FSI^-, thus forming $(LiFSI)_n$ clusters, similar to those shown in Figure 6.8a. The reduction peak at ~2 V (Figure 6.3c) is attributed to the reduction of such aggregates.

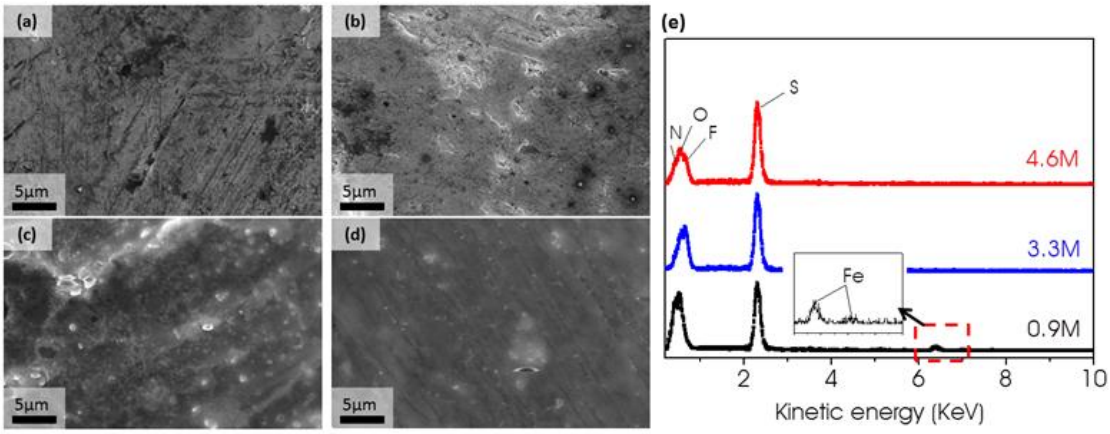

Figure 6.7 Post-mortem Li anode characterization: (a-d) SEM of original Li foil (a) and Li foil cycled in 0.9M (b), 3.3M (c) and 4.6M (d) LiFSI in DME; (e) EDS spectra of the original Li foil and Li foils cycled in 0.9M, 3.3M and 4.6M LiFSI in DME. Tiny amount of Fe was detected on the surface of Li foil cycled in 0.9M LiFSI in DME.

Reduction of LiFSI leads to its decomposition and the formation of LiF and $FSI_{(-F)}\bullet^-$ anion radicals (Figure 6.8a) which, in turn, may induce polymerization of $FSI_{(-F)}\bullet^-$ (Figure 6.8a), further reduce forming $LiNSO_2$, $LiFSO_2$ salts (Figure 6.8b) or react with DME upon oxidation, forming other reactive species (Figure 6.8c-d). The $FSI_{(-F)}^-\bullet$ or

NSO_2^- anions were predicted to oxidize at the cathode below 4.0 V yielding various co-polymerized products or produce DME• radicals by H abstraction (Figure 6.8c,d). The produced DME• radicals are of course extremely reactive towards DME polymerization and formation of the passivating SEI. In summary, our molecular modeling results suggest that the reduction of highly concentrated LiFSI in DME at the cathode yields LiF and polymerized DME (or DME with attached $FSI_{(-F)}$ or NSO_2) coating doped with LiFSI, $LiFSI_{(-F)}$, $LiFSI_{(-2F)}$ and other salts, such as $LiNSO_2$, $LiFSO_2$ and LiNSO. Interestingly, our modeling also predicts that numerous decomposition products are expected to form long-lived radicals (such as $FSI_{(-F)}^-$•,NSO_2•) with redox potentials between 1.5 and 4 V. Such redox active may serve as charge-transfer shuttles to further aid charge transfer from Fe or carbon to the insulating domains of LiF, thus contributing to a lower overpotential (Figure 6.3d) The high molecular weight $F(SO_2NSO_2)_nF/Li_n$ salts are expected to have a high transference number that would reduce concentration polarization within the passivation layer on both electrodes.

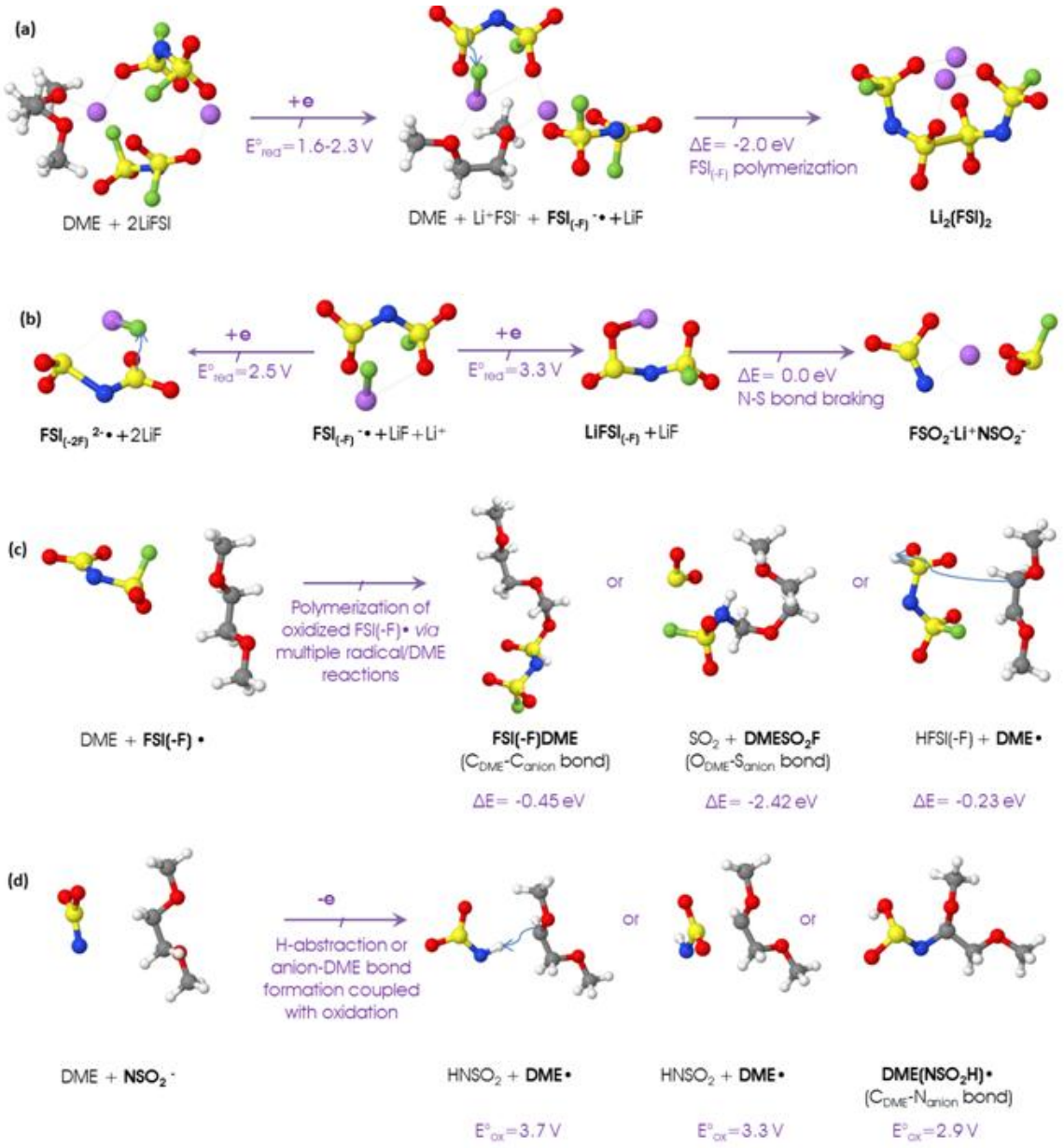

Figure 6.8 Selected results of G4MP2 quantum chemistry calculations, showing the LiFSI(DME) redox, decomposition and polymerization reactions and the expected SEI components: (a) formation of $FSI_{(-F)}^{-\bullet}$ radicals and their potential polymerization; (b) reduction of $FSI_{(-F)}^{-\bullet}$ and decomposition of some of the reduction products; (c) co-polymerization and other reactions of oxidized $FSI_{(-F)}^{-\bullet}$ with DME, such as H abstraction; (d) NSO_2^- oxidation coupled with its reaction with DME, leading to H abstraction and the resulting formation of DME• radicals or co-polymerization. Li is represented by green, S - by yellow, O – by red, N – by blue, C- by grey, H- by white and F – by purple spheres.

6.4 Summary

In-situ formation of the conformal Li-ion permeable solid coatings of the reduced LiFSI-DME electrolyte around FeF_2–based nanocomposite cathode particles was found to be a successful strategy to protect FeF_2 from dissolution and to achieve exceptionally long-term stability of the rechargeable MF-Li cells. By controlling the FeF_2-conductive carbon separating distance within ~ 2nm, by utilizing electrolyte that greatly minimizes Li dendrite and Li impedance growth and additionally produces redox active species that aid charge transfer in the cathode we have further demonstrated near-theoretical capacity and remarkable (for this chemistry) rate performance characteristics. We expect that QC calculations conducted on other electrolytes will assist in further electrolyte and protective layer optimization, revitalizing the MF research and contributing to their successful implementation. The success of this study further emphasizes the great potential of the rechargeable Li metal batteries with ultra-high energy density.

CHAPTER 7
CONCLUSIONS AND RECOMMENDATIONS

7.1 Conclusions

In this thesis, we studied the application of highly porous carbon in electrochemical energy storage devices. On the application of highly porous carbon in supercapacitors, we have investigated the effects of a variety of different factors and their correlations on the performance of porous carbon based electrodes, including the pore size distribution, electrode surface functionalizations, pH value of the electrolyte, polarity of electrolyte solvent, size of electrolyte ions, etc. Specifically, we have found the strong correlations between functionalization-enabled pseudocapacitance on carbon based electrodes and their self-discharge. We explained this phenomenon with the undesired participation of functional groups in irreversible redox reactions and the decomposition of electrolyte solvent due to the modification of pH value at the vicinity of electrode/electrolyte interface. Based on the fundamental knowledge about the effects of these key factors, we demonstrated high-power, high capacitance EDLCs based on sulfur-containing activated carbons. The pore size distribution of this carbon has been modified by the redox-inactive sulfide groups. As the result, the formation of bottle-necks in carbon pores has been greatly suppressed, and the portion of accessible mesopores has been increased. Based on the difference between the characteristic times required to establish a double layer and that of the pseudocapacitive redox reactions, we proposed a simple method to estimate the fraction of pseudocapacitance. This method is particularly valuable in cases when CV measurements do not show clear characteristic redox peaks.

On the application of highly porous carbon as electron conducting scaffold for electrodes of Li-ion batteries, we enabled high conductivity, prolonged cycle life and promoted reversibility of transition metal fluoride by developing metal fluoride/carbon nanocomposites. Liquid precursor of $FeSiF_6$ was vacuum-infiltrated into porous carbon and dispersed homogeneously. The nanocomposite was then heat-treated to convert $FeSiF_6$ into FeF_2. The size of metal fluoride nanoparticles is confined by the size of carbon pores within the range of 2-5nm, which greatly reduced the necessary diffusion length of electrolyte ions. The volume change of metal fluoride during charge-discharge is accommodated by the porosity in the carbon material, and the surface of metal fluoride is largely protected by carbon which could otherwise be passivated when in direct contact with electrolytes. The performance of metal fluoride based Li-ion battery was further improved by optimized electrolyte system, in which commonly used cyclic carbonate solvents which cause side-reaction were replaced by ether based solvents, such as DME. The application of LiFSI as electrolyte salt resulted in formation of stable and conductive SEI on the surface of nanocomposite particles, which improved the capacity and cycle life of the electrode. The composition of the in-situ formed SEI was characterized and analyzed. The FSI^- anion catalyzed the decomposition and polymerization of DME molecules, which contributes to the formation of SEI. Lastly, we observed compact and smooth SEI formation on the surface of lithium metal as anode, which greatly suppressed the growth of lithium dendrites.

In conclusion, we have gained valuable fundamental insights on the effects of various structural and chemical factors and their correlations on the performance of highly porous carbon based EDLCs. We also demonstrated the validity of highly porous

carbon as conductive scaffold for electrodes of Li-ion batteries. This information may assist in the future design and commercialization of viable carbon based EDLCs and highly capacitive but electronically insulating electrode materials.

7.2 Recommendations

While significantly improved performance has been demonstrated in FeF_2 based electrodes, a large pool of transition metal fluorides could be enabled as cathode materials for Li-ion batteries following the same strategy, with higher capacities and higher operating voltages. Besides, the effects of carbon pore size and pore size distribution, surface functionalization and solvent for the precursor solution should be systematically studied for optimization of metal fluoride/carbon nanocomposite as cathode material, ready for commercialization and real-life utilities. Possible chemical bondings in between carbon and metal fluoride may also be interesting, which further suppresses the detachment of metal fluoride during battery operation and maintains the mechanical integrity of the electrode.

In-situ formed SEI on metal fluoride cathode was found to be effective to improve long term cycle stability. However we still lack the information regarding the optimum condition of solid electrolyte layer formation. Further studies on reduction voltage cut off, current rate, different solid electrolyte forming additive, layer forming temperature would result in interesting and promising results.

Finally, a more comprehensive study of the impact of electrolyte composition (chemistry of salt(s) and solvent(s)) on the performance of metal fluoride based cathodes might provide additional pathways for controlling electrochemical reactions and further improvement of cell performance.

REFERENCES

1 Du, Q. L. *et al.* Preparation of functionalized graphene sheets by a low-temperature thermal exfoliation approach and their electrochemical supercapacitive behaviors. *Electrochimica Acta* **55**, 3897-3903, doi:10.1016/j.electacta.2010.01.089 (2010).

2 Inagaki, M., Konno, H. & Tanaike, O. Carbon materials for electrochemical capacitors. *Journal of Power Sources* **195**, 7880-7903 (2010).

3 Lin, Z. Y. *et al.* Superior Capacitance of Functionalized Graphene. *Journal of Physical Chemistry C* **115**, 7120-7125, doi:10.1021/jp2007073 (2011).

4 Goodenough, J. B. & Kim, Y. Challenges for Rechargeable Li Batteries†. *Chemistry of Materials* **22**, 587-603, doi:10.1021/cm901452z (2010).

5 Ellis, B. L., Lee, K. T. & Nazar, L. F. Positive Electrode Materials for Li-Ion and Li-Batteries†. *Chemistry of Materials* **22**, 691-714, doi:10.1021/cm902696j (2010).

6 Wang, Y. & Cao, G. Developments in Nanostructured Cathode Materials for High-Performance Lithium-Ion Batteries. *Advanced Materials* **20**, 2251-2269 (2008).

7 Etacheri, V., Marom, R., Elazari, R., Salitra, G. & Aurbach, D. Challenges in the development of advanced Li-ion batteries: a review. *Energy & Environmental Science* **4**, 3243-3262 (2011).

8 Lozano-Castello, D. *et al.* Influence of pore structure and surface chemistry on electric double layer capacitance in non-aqueous electrolyte. *Carbon* **41**, 1765-1775, doi:10.1016/s0008-6223(03)00141-6 (2003).

9 T. Morimoto, K. H., Y. Sanada, K. Kurihara. Electric double-layer capacitor using organic electrolyte. *Journal of Power Sources* **60** (1996).

10 Conway, B. E. *Electrochemical Supercapacitors*. Vol. 1 (Kluwer Academic / Plenum Publishers, 1999).

11 Shi, H. Activated carbons and double layer capacitance. *Electrochim. Acta.* **41**, 1633 (1996).

12 Chmiola, J. *et al.* Anomalous increase in carbon capacitance at pore sizes less than 1 nanometer. *Science* **313**, 1760-1763 (2006).

13 Chmiola, J., Yushin, G., Dash, R. & Gogotsi, Y. Effect of pore size and surface area of carbide derived carbons on specific capacitance. *Journal of Power Sources* **158**, 765-772 (2006).

14 Ravikovitch, P. I. & Neimark, A. V. Characterization of nanoporous materials from adsorption and desorption isotherms. *Colloids and Surfaces A: Physicochemical and Engineering Aspects* **187**, 11-21 (2001).

15 Frackowiak, E. Carbon materials for supercapacitor application. *Physical chemistry chemical physics : PCCP* **9**, 1774-1785, doi:10.1039/b618139m (2007).

16 Vaquero, S., D ́az, R., Anderson, M., Palma, J. & Marcilla, R. Insights into the influence of pore size distribution and surface functionalities in the behaviour of carbon supercapacitors. *Electrochimica Acta* **86**, 241-247 (2012).

17 Gryglewicz, G., Machnikowski, J., Lorenc-Grabowska, E., Lota, G. & Frackowiak, E. Effect of pore size distribution of coal-based activated carbons on double layer capacitance. *Electrochimica Acta* **50**, 1197-1206 (2005).

18 Su, D. S. & Schlogl, R. Nanostructured carbon and carbon nanocomposites for electrochemical energy storage applications. *ChemSusChem* **3**, 136-168, doi:10.1002/cssc.200900182 (2010).
19 Zhang, L. *et al.* Controlling the Effective Surface Area and Pore Size Distribution of sp2 Carbon Materials and Their Impact on the Capacitance Performance of These Materials. *J. Am. Chem. Soc.* **135**, 5921-5929 (2013).
20 Huang, J. S., Sumpter, B. G. & Meunier, V. A universal model for nanoporous carbon supercapacitors applicable to diverse pore regimes, carbon materials, and electrolytes. *Chemistry-a European Journal* **14**, 6614-6626, doi:10.1002/chem.200800639 (2008).
21 Eliad, L. *et al.* Assessing optimal pore-to-ion size relations in the design of porous poly(vinylidene chloride) carbons for EDL capacitors. *Applied Physics a-Materials Science & Processing* **82**, 607-613 (2006).
22 Wei, L., Sevilla, M., Fuertes, A. B., Mokaya, R. & Yushin, G. Hydrothermal Carbonization of Abundant Renewable Natural Organic Chemicals for High-Performance Supercapacitor Electrodes. *Advanced Energy Materials* **1**, 356-361 (2011).
23 Vix-Guterl, C. *et al.* Electrochemical energy storage in ordered porous carbon materials. *Carbon* **43**, 1293-1302 (2005).
24 Frackowiak, E. & Beguin, F. Carbon materials for the electrochemical storage of energy in capacitors. *Carbon* **39**, 937-950 (2001).
25 Xia, K., Gao, Q., Jiang, J. & Hu, J. Hierarchical porous carbons with controlled micropores and mesopores for supercapacitor electrode materials. *Carbon* **46**, 1718-1726 (2008).
26 Korenblit, Y. *et al.* High-Rate Electrochemical Capacitors Based on Ordered Mesoporous Silicon Carbide-Derived Carbon. *Acs Nano* **4**, 1337-1344, doi:10.1021/nn901825y (2010).
27 Xing, W. *et al.* Hierarchical porous carbons with high performance for supercapacitor electrodes. *Carbon* **47**, 1715-1722 (2009).
28 Gu, W., Sevilla, M., Magasinski, A., Fuertes, A. B. & Yushin, G. Sulfur-containing activated carbons with greatly reduced content of bottle neck pores for double-layer capacitors: a case study for pseudocapacitance detection. *Energy & Environmental Science* **6**, 2465, doi:10.1039/c3ee41182f (2013).
29 Tanahashi, I., Yoshida, A. & Nishino, A. Electrochemical Characterization of Activated Carbon-Fiber Cloth Polarizable Electrodes for Electric Double-Layer Capacitors. *Journal of the Electrochemical Society* **137**, 3052-3057 (1990).
30 Wang, H. L., Gao, Q. M. & Hu, J. Preparation of porous doped carbons and the high performance in electrochemical capacitors. *Microporous and Mesoporous Materials* **131**, 89-96, doi:10.1016/j.micromeso.2009.12.007 (2010).
31 Hsieh, C. T. & Teng, H. Influence of oxygen treatment on electric double-layer capacitance of activated carbon fabrics. *Carbon* **40**, 667-674, doi:10.1016/s0008-6223(01)00182-8 (2002).
32 Jurewicz, K., Babeł, K., Źiółkowski, A. & Wachowska, H. Ammoxidation of active carbons for improvement of supercapacitor characteristics. *Electrochimica Acta* **48**, 1491-1498, doi:10.1016/s0013-4686(03)00035-5 (2003).

33 Pandolfo, A. G. & Hollenkamp, A. F. Carbon properties and their role in supercapacitors. *Journal of Power Sources* **157**, 11-27, doi:10.1016/j.jpowsour.2006.02.065 (2006).
34 Raymundo-Piñero, E., Leroux, F. & Béguin, F. A High-Performance Carbon for Supercapacitors Obtained by Carbonization of a Seaweed Biopolymer. *Advanced Materials* **18**, 1877-1882, doi:10.1002/adma.200501905 (2006).
35 Radeke, K., Backhaus, K. & Swiatkowski, A. Electrical conductivity of activated carbons. *Carbon* **29**, 122-123 (1991).
36 Polovina, M., Babić, B., Kaluderović, B. & Dekanski, A. Surface characterization of oxidized activated carbon cloth. *Carbon* **35**, 1047-1052 (1997).
37 Lota, G., Lota, K. & Frackowiak, E. Nanotubes based composites rich in nitrogen for supercapacitor application. *Electrochemistry Communications* **9**, 1828-1832 (2007).
38 Gu, W. & Yushin, G. Review of nanostructured carbon materials for electrochemical capacitor applications: advantages and limitations of activated carbon, carbide-derived carbon, zeolite-templated carbon, carbon aerogels, carbon nanotubes, onion-like carbon, and graphene. *Wiley Interdisciplinary Reviews: Energy and Environment* **3**, 424-473 (2014).
39 Avraham, E., Yaniv, B., Soffer, A. & Aurbach, D. Developing ion electroadsorption stereoselectivity, by pore size adjustment with chemical vapor deposition onto active carbon fiber electrodes. Case of Ca2+/Na+ separation in water capacitive desalination. *The Journal of Physical Chemistry C* **112**, 7385-7389 (2008).
40 Noked, M., Avraham, E., Bohadana, Y., Soffer, A. & Aurbach, D. Development of anion stereoselective, activated carbon molecular sieve electrodes prepared by chemical vapor deposition. *The Journal of Physical Chemistry C* **113**, 7316-7321 (2009).
41 Qiao, W., Korai, Y., Mochida, I., Hori, Y. & Maeda, T. Preparation of an activated carbon artifact: oxidative modification of coconut shell-based carbon to improve the strength. *Carbon* **40**, 351-358 (2002).
42 Nishihara, H. *et al.* Investigation of the Ion Storage/Transfer Behavior in an Electrical Double-Layer Capacitor by Using Ordered Microporous Carbons as Model Materials. *Chemistry-a European Journal* **15**, 5355-5363, doi:10.1002/chem.200802406 (2009).
43 Brian E Conway, W. G. P., T-C. Liu. Diagnostic analyses for mechanisms of self-discharge of electrochemical capacitors and batteries. *Journal of Power Sources* **65** (1997).
44 Tongchang Liu, W. G. P., B. E. Conway. Self-discharge and potential recovery phenomena at thermally and electrochemically prepared RuO2 supercapacitor electrodes. *Electrochimica Acta* **42** (1996).
45 Zhang, Q., Rong, J. P., Ma, D. S. & Wei, B. Q. The governing self-discharge processes in activated carbon fabric-based supercapacitors with different organic electrolytes. *Energy & Environmental Science* **4**, 2152-2159, doi:10.1039/c0ee00773k (2011).

46 Kaus, M., Kowal, J. & Sauer, D. U. Modelling the effects of charge redistribution during self-discharge of supercapacitors. *Electrochimica Acta* **55**, 7516-7523, doi:10.1016/j.electacta.2010.01.002 (2010).
47 Yasser Diab, P. V., Hamid Gualous, Gerard Rojat. Self-discharge characterization and modeling of electrochemical capacitor used for power electronics applications. *IEEE Transactions on power electronics* **24** (2009).
48 Zhang, X. *et al.* The effects of surfactant template concentration on the supercapacitive behaviors of hierarchically porous carbons. *Journal of Power Sources* **199**, 402-408, doi:10.1016/j.jpowsour.2011.10.070 (2012).
49 Tarascon, J. M. Nano-sized transition-metal oxides as negative-electrode materials for lithium-ion batteries. *Nature* **407** (2000).
50 Zhao, L., Hu, Y. S., Li, H., Wang, Z. & Chen, L. Porous Li4Ti5O12 Coated with N-Doped Carbon from Ionic Liquids for Li-Ion Batteries. *Advanced Materials* **23**, 1385-1388 (2011).
51 Dominko, R. *et al.* The role of carbon black distribution in cathodes for Li ion batteries. *Journal of Power Sources* **119**, 770-773 (2003).
52 Evanoff, K. *et al.* Towards ultrathick battery electrodes: Aligned carbon nanotube–enabled architecture. *Advanced Materials* **24**, 533-537 (2012).
53 Ren, J. *et al.* Twisting Carbon Nanotube Fibers for Both Wire-Shaped Micro-Supercapacitor and Micro-Battery. *Advanced Materials* **25**, 1155-1159 (2013).
54 Wang, H. *et al.* Graphene-wrapped sulfur particles as a rechargeable lithium–sulfur battery cathode material with high capacity and cycling stability. *Nano Letters* **11**, 2644-2647 (2011).
55 Zhou, G. *et al.* Graphene-Wrapped Fe3O4 Anode Material with Improved Reversible Capacity and Cyclic Stability for Lithium Ion Batteries. *Chemistry of Materials* **22**, 5306-5313, doi:10.1021/cm101532x (2010).
56 Hu, L.-H., Wu, F.-Y., Lin, C.-T., Khlobystov, A. N. & Li, L.-J. Graphene-modified LiFePO4 cathode for lithium ion battery beyond theoretical capacity. *Nature communications* **4**, 1687 (2013).
57 Shi, Y. *et al.* Hollow structured Li3VO4 wrapped with graphene nanosheets in situ prepared by a one-pot template-free method as an anode for lithium-ion batteries. *Nano Letters* **13**, 4715-4720 (2013).
58 Zhang, C. *et al.* Carbon-coated SnO 2/graphene nanosheets as highly reversible anode materials for lithium ion batteries. *Carbon* **50**, 1897-1903 (2012).
59 Luo, J. *et al.* Crumpled graphene-encapsulated Si nanoparticles for lithium ion battery anodes. *The Journal of Physical Chemistry Letters* **3**, 1824-1829 (2012).
60 Wen, Z., Yang, J., Wang, B., Wang, K. & Liu, Y. High capacity silicon/carbon composite anode materials for lithium ion batteries. *Electrochemistry Communications* **5**, 165-168 (2003).
61 Liu, N. *et al.* A yolk-shell design for stabilized and scalable Li-ion battery alloy anodes. *Nano Letters* **12**, 3315-3321 (2012).
62 Magasinski, A. *et al.* High-performance lithium-ion anodes using a hierarchical bottom-up approach. *Nature Materials* **9**, 353-358 (2010).
63 Cabana, J., Monconduit, L., Larcher, D. & Palacin, M. R. Beyond Intercalation-Based Li-Ion Batteries: The State of the Art and Challenges of

Electrode Materials Reacting Through Conversion Reactions. *Advanced Materials* **22**, E170-E192 (2010).

64 Debart, A., Dupont, L., Poizot, P., Leriche, J. & Tarascon, J. A transmission electron microscopy study of the reactivity mechanism of tailor-made CuO particles toward lithium. *Journal of the Electrochemical Society* **148**, A1266-A1274 (2001).

65 Armand, M. & Tarascon, J.-M. Building better batteries. *Nature* **451**, 652-657 (2008).

66 Hajime Arai, S. O., Yoji Sakurai, Jun-ichi Yamaki. Cathode performance and voltage estimation of metal trihalides. *Journal of Power Sources* **68** (1997).

67 Badway, F., Pereira, N., Cosandey, F. & Amatucci, G. Batteries, Fuel Cells, and Energy Conversion-Carbon-Metal Fluoride Nanocomposites-Structure and Electrochemistry of FeF3: C. *Journal of the Electrochemical Society* **150**, A1209 (2003).

68 Badway, F., Pereira, N., Cosandey, F. & Amatucci, G. G. Carbon-Metal Fluoride Nanocomposites. *Journal of the Electrochemical Society* **150**, A1209, doi:10.1149/1.1596162 (2003).

69 Makimura, Y., Rougier, A. & Tarascon, J.-M. Pulsed laser deposited iron fluoride thin films for lithium-ion batteries. *Applied Surface Science* **252**, 4587-4592, doi:10.1016/j.apsusc.2005.06.043 (2006).

70 McChesney, J., Hetzer, M., Shi, H., Charlton, T. & Lederman, D. Growth study of epitaxial FexZn1− xF2 thin films. *Journal of Materials Research* **16**, 1769-1775 (2001).

71 Qiu, S. & Yarmoff, J. Self-limiting growth of transition-metal fluoride films from the reaction with XeF 2. *Physical Review B* **63**, 115409 (2001).

72 Barriere, A., Gianduzzo, J. & Fournes, L. Magnetic and Mössbauer resonance studies of FeF 3 thin films as a function of their growth model. *Thin Solid Films* **89**, 233-238 (1982).

73 Kim, S. W., Seo, D. H., Gwon, H., Kim, J. & Kang, K. Fabrication of FeF3 Nanoflowers on CNT branches and their application to high power lithium rechargeable batteries. *Adv Mater* **22**, 5260-5264, doi:10.1002/adma.201002879 (2010).

74 Fu, Z.-W. *et al.* Electrochemical Reaction of Lithium with Cobalt Fluoride Thin Film Electrode. *Journal of the Electrochemical Society* **152**, E50, doi:10.1149/1.1839512 (2005).

75 Shi, Y.-L. *et al.* Electrochemical impedance spectroscopic study of the electronic and ionic transport properties of NiF2/C composites. *International Journal of Electrochemical Science* **6**, 3399-3415 (2011).

76 Lee, D. H., Carroll, K. J., Calvin, S., Jin, S. & Meng, Y. S. Conversion mechanism of nickel fluoride and NiO-doped nickel fluoride in Li ion batteries. *Electrochimica Acta* **59**, 213-221, doi:10.1016/j.electacta.2011.10.105 (2012).

77 Zhang, H., Zhou, Y.-N., Sun, Q. & Fu, Z.-W. Nanostructured nickel fluoride thin film as a new Li storage material. *Solid State Sciences* **10**, 1166-1172, doi:10.1016/j.solidstatesciences.2007.12.019 (2008).

78 Hu, B. *et al.* Effects of amorphous AlPO 4 coating on the electrochemical performance of BiF 3 cathode materials for lithium-ion batteries. *Journal of Power Sources* **218**, 204-211 (2012).
79 Hu, B. *et al.* Improved electrochemical properties of BiF 3/C cathode via adding amorphous AlPO 4 for lithium-ion batteries. *Electrochimica Acta* **102**, 8-18 (2013).
80 F. Badway, A. N. M., N. Pereira, J.F. Al-Sharab, F. Cosandey, I. Plitz, G.G. Amatucci. Structure and electrochemistry of copper fluoride nanocomposites utilizing mixed conducting matrices. *Chemistry of Materials* **19** (2007).
81 Wang, F. *et al.* Conversion reaction mechanisms in lithium ion batteries: study of the binary metal fluoride electrodes. *J Am Chem Soc* **133**, 18828-18836, doi:10.1021/ja206268a (2011).
82 Wang, F. *et al.* Ternary metal fluorides as high-energy cathodes with low cycling hysteresis. *Nature communications* **6** (2015).
83 Wall, C., Prakash, R., Kübel, C., Hahn, H. & Fichtner, M. Synthesis of [Co/LiF/C] nanocomposite and its application as cathode in lithium-ion batteries. *Journal of Alloys and Compounds* **530**, 121-126 (2012).
84 Zhou, Y. *et al.* LiF/ Co Nanocomposite as a New Li Storage Material. *Electrochemical and Solid-State Letters* **9**, A147-A150 (2006).
85 Zhou, Y., Wu, C., Zhang, H., Wu, X. & Fu, Z. The Electrochemical Properties of LiF-Ni Nanocomposite Thin Film. *Acta Physico-Chimica Sinica* **22**, 1111-1115 (2006).
86 Liao, P., MacDonald, B. L., Dunlap, R. & Dahn, J. Combinatorially Prepared [LiF] 1− x Fe x Nanocomposites for Positive Electrode Materials in Li-Ion Batteries. *Chemistry of Materials* **20**, 454-461 (2007).
87 Hua, X. *et al.* Comprehensive Study of the CuF2 Conversion Reaction Mechanism in a Lithium Ion Battery. *The Journal of Physical Chemistry C* **118**, 15169-15184 (2014).
88 Bervas, M., Badway, F., Klein, L. C. & Amatucci, G. G. Bismuth Fluoride Nanocomposite as a Positive Electrode Material for Rechargeable Lithium Batteries. *Electrochemical and Solid-State Letters* **8**, A179, doi:10.1149/1.1861040 (2005).
89 Bervas, M., Klein, L. & Amatucci, G. Reversible conversion reactions with lithium in bismuth oxyfluoride nanocomposites. *Journal of the Electrochemical Society* **153**, A159-A170 (2006).
90 Simon, P. & Gogotsi, Y. Materials for electrochemical capacitors. *Nature Materials* **7**, 845-854, doi:10.1038/nmat2297 (2008).
91 Khomenko, V., Raymundo-Piñero, E. & Béguin, F. High-energy density graphite/AC capacitor in organic electrolyte. *Journal of Power Sources* **177**, 643-651, doi:10.1016/j.jpowsour.2007.11.101 (2008).
92 Amatucci, G. G., Badway, F., Du Pasquier, A. & Zheng, T. An Asymmetric Hybrid Nonaqueous Energy Storage Cell. *Journal of the Electrochemical Society* **148**, A930, doi:10.1149/1.1383553 (2001).
93 Lee, S. W., Kim, B. S., Chen, S., Shao-Horn, Y. & Hammond, P. T. Layer-by-Layer Assembly of All Carbon Nanotube Ultrathin Films for Electrochemical Applications. *J. Am. Chem. Soc.* **131**, 671-679, doi:10.1021/ja807059k (2009).

94 Lee, S. W. *et al.* High-power lithium batteries from functionalized carbon-nanotube electrodes. *Nat Nano* **5**, 531-537, doi:http://www.nature.com/nnano/journal/v5/n7/suppinfo/nnano.2010.116_S1.html (2010).
95 Shenderova, O. *et al.* Detonation nanodiamond and onion-like carbon: applications in composites. *Physica Status Solidi a-Applications and Materials Science* **205**, 2245-2251, doi:10.1002/pssa.200879706 (2008).
96 Portet, C., Yushin, G. & Gogotsi, Y. Electrochemical performance of carbon onions, nanodiamonds, carbon black and multiwalled nanotubes in electrical double layer capacitors. *Carbon* **45**, 2511-2518 (2007).
97 Osswald, S., Yushin, G., Mochalin, V., Kucheyev, S. O. & Gogotsi, Y. Control of sp(2)/sp(3) carbon ratio and surface chemistry of nanodiamond powders by selective oxidation in air. *J. Am. Chem. Soc.* **128**, 11635-11642, doi:10.1021/ja063303n (2006).
98 Yushin, G. N., Osswald, S., Padalko, V. I., Bogatyreva, G. P. & Gogotsi, Y. Effect of sintering on structure of nanodiamond. *Diam. Related Mater.* **14**, 1721-1729 (2005).
99 Kovalenko, I., Bucknall, D. & Yushin, G. Detonation Nanodiamond and Onion-like Carbon - Embedded Polyaniline for Supercapacitors. *Advanced Functional Materials*, DOI: 10.1002/adfm.201000906 (2010).
100 Kuznetsov, V. L., Chuvilin, A. L., Butenko, Y. V., Malkov, I. Y. & Titov, V. M. Onion-like Carbon from Ultra-Disperse Diamond. *Chemical Physics Letters* **222**, 343-348 (1994).
101 Pech, D. *et al.* Ultrahigh-power micrometre-sized supercapacitors based on onion-like carbon. *Nature Nanotechnology* **5**, 651-654, doi:10.1038/nnano.2010.162 (2010).
102 Korenblit, Y. *et al.* In-Situ Studies of Ion Transport in Microporous Supercapacitor Electrodes at Ultra-Low Temperatures. *Advanced Functional Materials* (2012).
103 Wei, L. & Yushin, G. Electrical double layer capacitors with activated sucrose-derived carbon electrodes. *Carbon* **49**, 4830-4838 (2011).
104 Rose, M. *et al.* in *Small* Vol. 7 1108-1117 (2011).
105 Al-zubaidi, A. *et al.* Cyclic voltammogram profile of single-walled carbon nanotube electric double-layer capacitor electrode reveals dumbbell shape. *The Journal of Physical Chemistry C* **116**, 7681-7686 (2012).
106 Elzbieta Frackowiak, F. B. Carbon materials for the electrochemical storage of energy in capacitors. *Carbon* **39** (2001).
107 Kotz, R. Principles and applications of electrochemical capacitors. *Electrochimica Acta* **45** (2000).
108 Patrice Simon, Y. G. Materials for electrochemical capacitors. *Nature materials* **7** (2008).
109 Hu, C.-C. Ideal capacitive behavior of hydrous maganese oxide prepared by anodic deposition. *Electrochemistry Communications* **4** (2002).
110 Zhang, K., Zhang, L. L., Zhao, X. S. & Wu, J. Graphene/Polyaniline Nanofiber Composites as Supercapacitor Electrodes. *Chemistry of Materials* **22**, 1392-1401, doi:10.1021/cm902876u (2010).

111 Wang, Y. Supercapacitor devices based on graphene materials. *The journal of physical chemistry C* **113** (2009).
112 Brousse, T. *et al.* Long-term cycling behavior of asymmetric activated carbon/MnO2 aqueous electrochemical supercapacitor. *Journal of Power Sources* **173**, 633-641, doi:10.1016/j.jpowsour.2007.04.074 (2007).
113 Balducci, A. *et al.* Cycling stability of a hybrid activated carbon//poly(3-methylthiophene) supercapacitor with N-butyl-N-methylpyrrolidinium bis(trifluoromethanesulfonyl)imide ionic liquid as electrolyte. *Electrochimica Acta* **50**, 2233-2237, doi:10.1016/j.electacta.2004.10.006 (2005).
114 Lee, S. W. *et al.* High-power lithium batteries from functionalized carbon-nanotube electrodes. *Nature Nano* **5**, 531-537, doi:http://www.nature.com/nnano/journal/v5/n7/suppinfo/nnano.2010.116_S1.html (2010).
115 Gu, W., Peters, N. & Yushin, G. Functionalized Carbon Onions, Detonation Nanodiamond and Mesoporous Carbon as Cathodes in Li-ion Electrochemical Energy Storage Devices. *Carbon* (2012).
116 Gallagher, K. G., Yushin, G. & Fuller, T. F. The Role of Nanostructure in the Electrochemical Oxidation of Model-Carbon Materials in Acidic Environments. *Journal of the Electrochemical Society* **157**, B820-B830, doi:10.1149/1.3374662 (2010).
117 Jow, T. R. & Zheng, J. P. Electrochemical capacitors using hydrous ruthenium oxide and hydrogen inserted ruthenium oxide. *Journal of the Electrochemical Society* **145**, 49-52 (1998).
118 Zheng, J. P. & Jow, T. R. A new charge storage mechanism for electrochemical capacitors. *Journal of the Electrochemical Society* **142**, L6-L8 (1995).
119 Itai, H., Nishihara, H., Kogure, T. & Kyotani, T. Three-Dimensionally Arrayed and Mutually Connected 1.2-nm Nanopores for High-Performance Electric Double Layer Capacitor. *J. Am. Chem. Soc.* **133**, 1165-1167, doi:10.1021/ja108315p (2011).
120 Kyotani, T., Ma, Z. X. & Tomita, A. Template synthesis of novel porous carbons using various types of zeolites. *Carbon* **41**, 1451-1459, doi:10.1016/s0008-6223(03)00090-3 (2003).
121 Ma, Z. X., Kyotani, T. & Tomita, A. Preparation of a high surface area microporous carbon having the structural regularity of Y zeolite. *Chemical Communications*, 2365-2366, doi:10.1039/b006295m (2000).
122 Korenblit, Y. *et al.* In Situ Studies of Ion Transport in Microporous Supercapacitor Electrodes at Ultralow Temperatures. *Advanced Functional Materials* **22**, 1655-1662, doi:10.1002/adfm.201102573 (2012).
123 Kajdos, A., Kvit, A., Jones, F., Jagiello, J. & Yushin, G. Tailoring the Pore Alignment for Rapid Ion Transport in Microporous Carbons. *J. Am. Chem. Soc.* **132**, 3252 (2010).
124 Portet, C. *et al.* Electrical Double-Layer Capacitance of Zeolite-Templated Carbon in Organic Electrolyte. *Journal of the Electrochemical Society* **156**, A1-A6, doi:10.1149/1.3002375 (2009).
125 Ania, C. O., Khomenko, V., Raymundo-Pinero, E., Parra, J. B. & Beguin, F. The large electrochemical capacitance of microporous doped carbon obtained by using

a zeolite template. *Advanced Functional Materials* **17**, 1828-1836, doi:10.1002/adfm.200600961 (2007).

126 Oschatz, M. *et al.* A cubic ordered, mesoporous carbide-derived carbon for gas and energy storage applications. *Carbon* **48**, 3987-3992, doi:10.1016/j.carbon.2010.06.058 (2010).

127 Vix-Guterl, C. *et al.* Electrochemical energy storage in ordered porous carbon materials. *Carbon* **43**, 1293-1302, doi:10.1016/j.carbon.2004.12.028 (2005).

128 Lee, J., Kim, J. & Hyeon, T. Recent Progress in the Synthesis of Porous Carbon Materials. *Advanced Materials* **18**, 2073-2094, doi:10.1002/adma.200501576 (2006).

129 Borchardt, L. *et al.* Ordered mesoporous carbide-derived carbons prepared by soft templating. *Carbon* **50**, 3987-3994, doi:10.1016/j.carbon.2012.04.006 (2012).

130 Hoffman, E. N., Yushin, G., El-Raghy, T., Gogotsi, Y. & Barsoum, M. W. Micro and mesoporosity of carbon derived from ternary and binary metal carbides. *Microporous and Mesoporous Materials* **112**, 526-532, doi:10.1016/j.micromeso.2007.10.033 (2008).

131 Portet, C., Yushin, G. & Gogotsi, Y. Effect of Carbon Particle Size on Electrochemical Performance of EDLC *J. Electrochem. Soc* **155 (7)**, A531-A536 (2008).

132 Yushin, G., Nikitin, A. & Gogotsi, Y. in *Nanomaterials Handbook* (ed Y. Gogotsi) 239-282 (CRC Press, 2006).

133 Chmiola, J., Yushin, G., Gogotsi, Y., Portet, C. & Simon, P. Anomalous increase in carbon capacitance at pore size below 1 nm. *Science* **313**, 1760-1763 (2006).

134 Oschatz, M. *et al.* Carbide-Derived Carbon Monoliths with Hierarchical Pore Architectures. *Angewandte Chemie-International Edition* **51**, 7577-7580, doi:10.1002/anie.201200024 (2012).

135 Presser, V., Heon, M. & Gogotsi, Y. Carbide-Derived Carbons - From Porous Networks to Nanotubes and Graphene. *Advanced Functional Materials* **21**, 810-833, doi:10.1002/adfm.201002094 (2011).

136 Eskusson, J., Janes, A., Kikas, A., Matisen, L. & Lust, E. Physical and electrochemical characteristics of supercapacitors based on carbide derived carbon electrodes in aqueous electrolytes. *Journal of Power Sources* **196**, 4109-4116, doi:10.1016/j.jpowsour.2010.10.100 (2011).

137 Kurig, H., Janes, A. & Lust, E. Electrochemical Characteristics of Carbide-Derived Carbon vertical bar 1-Ethyl-3-methylimidazolium Tetrafluoroborate Supercapacitor Cells. *Journal of the Electrochemical Society* **157**, A272-A279, doi:10.1149/1.3274208 (2010).

138 Permann, L., Latt, M., Leis, J. & Arulepp, M. Electrical double layer characteristics of nanoporous carbon derived from titanium carbide. *Electrochimica Acta* **51**, 1274-1281 (2006).

139 Leis, J., Arulepp, M., Kuura, A., Latt, M. & Lust, E. Electrical double-layer characteristics of novel carbide-derived carbon materials. *Carbon* **44**, 2122-2129, doi:10.1016/j.carbon.2006.04.022 (2006).

140 Janes, A. & Lust, E. Electrochemical characteristics of nanoporous carbide-derived carbon materials in various nonaqueous electrolyte solutions. *Journal of the Electrochemical Society* **153**, A113-A116, doi:10.1149/1.2135212 (2006).

141 Laudisio, G. *et al.* Carbide-derived carbons: A comparative study of porosity based on small-angle scattering and adsorption isotherms. *Langmuir* **22**, 8945-8950, doi:10.1021/1a060860e (2006).
142 Wei, L. & Yushin, G. Nanostructured Activated Carbons from Natural Precursors for Electrical Double Layer Capacitors. *Nano Energy* **1**, 552–565 (2012).
143 Wei, L., Sevilla, M., Fuertes, A. B., Mokaya, R. & Yushin, G. Polypyrrole-Derived Activated Carbons for High-Performance Electrical Double-Layer Capacitors with Ionic Liquid Electrolyte. *Advanced Functional Materials* **22**, 827-834, doi:10.1002/adfm.201101866 (2012).
144 Choi, N.-S., Chen, Z., Freunberger, S.A., Ji, X., Sun, Y.-K., Amine, K., Yushin, G., Nazar, L.F., Cho, J., and Bruce, P.G. Current Current Issues in Energy Storage Materials and Devices in Energy Storage Materials and Devices. *Angewandte Chemie International Edition* **in press** (2012).
145 Gu, W., Peters, N. & Yushin, G. Functionalized Carbon Onions, Detonation Nanodiamond and Mesoporous Carbon as Cathodes in Li-ion Electrochemical Energy Storage Devices. *Carbon*.
146 Wei, L. & Yushin, G. Electrical double layer capacitors with activated sucrose-derived carbon electrodes. *Carbon* **49**, 4830-4838, doi:10.1016/j.carbon.2011.07.003 (2011).
147 Wei, L. & Yushin, G. Electrical Double Layer Capacitors with Sucrose Derived Carbon Electrodes in Ionic Liquid Electrolytes *Power Sources* **196** 4072 - 4079 (2011).
148 Wei, L., Sevilla, M., Fuertesc, A. B., Mokaya, R. & Yushin, G. Hydrothermal Carbonisation of Abundant Renewable Natural Organic Chemicals for High-Performance Supercapacitor Electrodes. *Advanced Energy Materials* **1**, 356-361 (2011).
149 Rufford, T. E., Hulicova-Jurcakova, D., Khosla, K., Zhu, Z. H. & Lu, G. Q. Microstructure and electrochemical double-layer capacitance of carbon electrodes prepared by zinc chloride activation of sugar cane bagasse. *Journal of Power Sources* **195**, 912-918, doi:10.1016/j.jpowsour.2009.08.048 (2010).
150 Hulicova-Jurcakova, D., Seredych, M., Lu, G. Q. & Bandosz, T. J. Combined Effect of Nitrogen- and Oxygen-Containing Functional Groups of Microporous Activated Carbon on its Electrochemical Performance in Supercapacitors. *Advanced Functional Materials* **19**, 438-447, doi:10.1002/adfm.200801236 (2009).
151 Hulicova-Jurcakova, D. *et al.* Nitrogen-Enriched Nonporous Carbon Electrodes with Extraordinary Supercapacitance. *Advanced Functional Materials* **19**, 1800-1809, doi:10.1002/adfm.200801100 (2009).
152 Raymundo-Pinero, E., Kierzek, K., Machnikowski, J. & Beguin, F. Relationship between the nanoporous texture of activated carbons and their capacitance properties in different electrolytes. *Carbon* **44**, 2498-2507, doi:10.1016/j.carbon.2006.05.022 (2006).
153 Salitra, G., Soffer, A., Eliad, L., Cohen, Y. & Aurbach, D. Carbon electrodes for double-layer capacitors - I. Relations between ion and pore dimensions. *Journal of the Electrochemical Society* **147**, 2486-2493, doi:10.1149/1.1393557 (2000).

154 Arulepp, M. *et al.* Influence of the solvent properties on the characteristics of a double layer capacitor. *Journal of Power Sources* **133**, 320-328, doi:10.1016/j.jpowsour.2004.03.026 (2004).
155 Lust, E. *et al.* Electrochemical Properties of Nanoporous Carbon Electrodes in Various Nonaqueous Electrolytes. *J. Solid State Electrochem.* **7**, 91-105 (2003).
156 Hasegawa, G., Kanamori, K., Nakanishi, K. & Hanada, T. Fabrication of activated carbons with well-defined macropores derived from sulfonated poly(divinylbenzene) networks. *Carbon* **48**, 1757-1766, doi:10.1016/j.carbon.2010.01.019 (2010).
157 Hasegawa, G. *et al.* Monolithic electrode for electric double-layer capacitors based on macro/meso/microporous S-Containing activated carbon with high surface area. *Journal of Materials Chemistry* **21**, 2060, doi:10.1039/c0jm03793a (2011).
158 Sevilla, M. & Fuertes, A. B. Highly porous S-doped carbons. *Microporous and Mesoporous Materials* **158**, 318-323, doi:10.1016/j.micromeso.2012.02.029 (2012).
159 Yang, R. T. *Adsorbents: Fundamentals and Applications*. (Wiley & Sons, Inc., 2003).
160 Thomsen, C. & Reich, S. Doable resonant Raman scattering in graphite. *Phys. Rev. Lett.* **85**, 5214-5217 (2000).
161 Tan, P. H., Dimovski, S. & Gogotsi, Y. Raman scattering of non-planar graphite: arched edges, polyhedral crystals, whiskers and cones. *Phil. Trans. Royal Soc. A* **362** (2004).
162 Goodenough, J. B. & Kim, Y. Challenges for Rechargeable Li Batteries†. *Chemistry of Materials* **22**, 587-603 (2009).
163 Amatucci, G. G. & Pereira, N. Fluoride based electrode materials for advanced energy storage devices. *Journal of Fluorine Chemistry* **128**, 243-262, doi:10.1016/j.jfluchem.2006.11.016 (2007).
164 Li, B., Rooney, D. W., Zhang, N. & Sun, K. An In Situ Ionic-Liquid-Assisted Synthetic Approach to Iron Fluoride/Graphene Hybrid Nanostructures as Superior Cathode Materials for Lithium Ion Batteries. *ACS applied materials & interfaces* **5**, 5057-5063 (2013).
165 Gmitter, A. J. *et al.* Formation, dynamics, and implication of solid electrolyte interphase in high voltage reversible conversion fluoride nanocomposites. *Journal of Materials Chemistry* **20**, 4149-4161 (2010).
166 Titirici, M.-M. & Antonietti, M. Chemistry and materials options of sustainable carbon materials made by hydrothermal carbonization. *Chemical Society Reviews* **39**, 103-116 (2010).
167 Li, W. *et al.* Nitrogen enriched mesoporous carbon spheres obtained by a facile method and its application for electrochemical capacitor. *Electrochemistry Communications* **9**, 569-573 (2007).
168 Yang, J.-B. *et al.* Preparation and properties of phenolic resin-based activated carbon spheres with controlled pore size distribution. *Carbon* **40**, 911-916 (2002).
169 Wang, Q. *et al.* Preparation of polystyrene-based activated carbon spheres with high surface area and their adsorption to dibenzothiophene. *Fuel Processing Technology* **90**, 381-387 (2009).

170 Bai, F., Yang, X. & Huang, W. Synthesis of narrow or monodisperse poly (divinylbenzene) microspheres by distillation-precipitation polymerization. *Macromolecules* **37**, 9746-9752 (2004).
171 Downey, J. S., Frank, R. S., Li, W.-H. & Stöver, H. D. Growth mechanism of poly (divinylbenzene) microspheres in precipitation polymerization. *Macromolecules* **32**, 2838-2844 (1999).
172 Wei, L., Sevilla, M., Fuertes, A. B., Mokaya, R. & Yushin, G. Polypyrrole-derived Activated Carbons for High-performance Electrical Double-layer Capacitors with Ionic Liquid Electrolyte. *Advanced Functional Materials* **under review** (2011).
173 Yan, J. *et al.* A high-performance carbon derived from polyaniline for supercapacitors. *Electrochemistry Communications* **12**, 1279–1282 (2010).
174 Shuangling Guo, F. W., Hao Chen, He Ren, Rongshun Wang, Xiumei Pan. Preparation and performance of polyvinyl alcohol-based activated carbon as electrode material in both aqueous and organic electrolytes. *Journal of Solid State Electrochemistry* **16** (2012).
175 Tien, C. *Adsorption calculations and modeling*. Vol. 244 (Butterworth-Heinemann Boston, 1994).
176 Ravikovitch, P. I., Vishnyakov, A. & Neimark, A. V. Density functional theories and molecular simulations of adsorption and phase transitions in nanopores. *Physical Review E* **64**, 011602 (2001).
177 Pereira, N., Badway, F., Wartelsky, M., Gunn, S. & Amatucci, G. G. Iron Oxyfluorides as High Capacity Cathode Materials for Lithium Batteries. *Journal of the Electrochemical Society* **156**, A407, doi:10.1149/1.3106132 (2009).
178 Breitung, B. *et al.* Influence of particle size and fluorination ratio of CFx precursor compounds on the electrochemical performance of C–FeF2 nanocomposites for reversible lithium storage. *Beilstein journal of nanotechnology* **4**, 705-713 (2013).
179 Gmitter, A. J., Gural, J. & Amatucci, G. G. Electrolyte development for improved cycling performance of bismuth fluoride nanocomposite positive electrodes. *Journal of Power Sources* **217**, 21-28 (2012).
180 Matsuoka, O. *et al.* Ultra-thin passivating film induced by vinylene carbonate on highly oriented pyrolytic graphite negative electrode in lithium-ion cell. *Journal of Power Sources* **108**, 128-138 (2002).
181 Möller, K.-C. *et al.* In situ characterization of the SEI formation on graphite in the presence of a vinylene group containing film-forming electrolyte additives. *Journal of Power Sources* **119**, 561-566 (2003).
182 Ota, H., Sakata, Y., Inoue, A. & Yamaguchi, S. Analysis of vinylene carbonate derived SEI layers on graphite anode. *Journal of the Electrochemical Society* **151**, A1659-A1669 (2004).
183 Wu, H.-C., Su, C.-Y., Shieh, D.-T., Yang, M.-H. & Wu, N.-L. Enhanced high-temperature cycle life of LiFePO4-based Li-ion batteries by vinylene carbonate as electrolyte additive. *Electrochemical and Solid-State Letters* **9**, A537-A541 (2006).

184 Komaba, S., Kumagai, N. & Kataoka, Y. Influence of manganese (II), cobalt (II), and nickel (II) additives in electrolyte on performance of graphite anode for lithium-ion batteries. *Electrochimica Acta* **47**, 1229-1239 (2002).
185 Hong Li, G. R., Joachim Maier. Reversible formation and decomposition of LiF clusters using transition metal fluorides as precursors and their application in rechargeable Li batteries. *Advanced Materials* **15** (2003).
186 Badway, F., Pereira, N., Cosandey, F. & Amatucci, G. in *MRS Proceedings.* EE7. 1 (Cambridge Univ Press).
187 Badway, F. *et al.* Structure and electrochemistry of copper fluoride nanocomposites utilizing mixed conducting matrices. *Chemistry of Materials* **19**, 4129-4141 (2007).
188 Choi, N. S. *et al.* Challenges Facing Lithium Batteries and Electrical Double-Layer Capacitors. *Angewandte Chemie-International Edition* **51**, 9994-10024, doi:10.1002/anie.201201429 (2012).
189 Bruce, P. G., Hardwick, L. J. & Abraham, K. Lithium-air and lithium-sulfur batteries. *MRS Bulletin* **36**, 506-512 (2011).
190 Bruce, P. G., Scrosati, B. & Tarascon, J. M. Nanomaterials for rechargeable lithium batteries. *Angewandte Chemie International Edition* **47**, 2930-2946 (2008).
191 Wang, F. *et al.* Ternary metal fluorides as high-energy cathodes with low cycling hysteresis. *Nature communications* **6**, 6668-6668, doi:10.1038/ncomms7668 (2015).
192 Hu, Y.-Y. *et al.* Origin of additional capacities in metal oxide lithium-ion battery electrodes. *Nature Materials* **12**, 1130-1136, doi:10.1038/nmat3784 (2013).
193 Johnson, Z., Cordova, S. & Amatucci, G. Advanced FeF3 Cathode Enabled Lithium-ion Battery. (SAE Technical Paper, 2008).
194 Liu, L. *et al.* Excellent cycle performance of Co-doped FeF 3/C nanocomposite cathode material for lithium-ion batteries. *Journal of Materials Chemistry* **22**, 17539-17550 (2012).
195 Li, L., Meng, F. & Jin, S. High-capacity lithium-ion battery conversion cathodes based on iron fluoride nanowires and insights into the conversion mechanism. *Nano Letters* **12**, 6030-6037 (2012).
196 Li, T., Li, L., Cao, Y. L., Ai, X. P. & Yang, H. X. Reversible three-electron redox behaviors of FeF3 nanocrystals as high-capacity cathode-active materials for Li-ion batteries. *The Journal of Physical Chemistry C* **114**, 3190-3195 (2010).
197 Myung, S.-T., Sakurada, S., Yashiro, H. & Sun, Y.-K. Iron trifluoride synthesized via evaporation method and its application to rechargeable lithium batteries. *Journal of Power Sources* **223**, 1-8 (2013).
198 Badway, F., Pereira, N., Cosandey, F. & Amatucci, G. Carbon-Metal Fluoride Nanocomposites Structure and Electrochemistry of FeF 3: C. *Journal of the Electrochemical Society* **150**, A1209-A1218 (2003).
199 Plitz, I. *et al.* Structure and electrochemistry of carbon-metal fluoride nanocomposites fabricated by solid-state redox conversion reaction. *Journal of the Electrochemical Society* **152**, A307-A315 (2005).
200 Li, H., Balaya, P. & Maier, J. Li-Storage via Heterogeneous Reaction in Selected Binary Metal Fluorides and Oxides. *Journal of the Electrochemical Society* **151**, A1878, doi:10.1149/1.1801451 (2004).

201 Zhou, J., Zhang, D., Zhang, X., Song, H. & Chen, X. Carbon-Nanotube-Encapsulated FeF2 Nanorods for High-Performance Lithium-Ion Cathode Materials. *ACS applied materials & interfaces* **6**, 21223-21229 (2014).
202 Li, L., Meng, F. & Jin, S. High-capacity lithium-ion battery conversion cathodes based on iron fluoride nanowires and insights into the conversion mechanism. *Nano Lett* **12**, 6030-6037, doi:10.1021/nl303630p (2012).
203 Gu, W., Magasinski, A., Zdyrko, B. & Yushin, G. Metal Fluorides Nanoconfined in Carbon Nanopores as Reversible High Capacity Cathodes for Li and Li-Ion Rechargeable Batteries: FeF2 as an Example. *Advanced Energy Materials* (2014).
204 Campion, C. L., Li, W. & Lucht, B. L. Thermal decomposition of LiPF6-based electrolytes for lithium-ion batteries. *Journal of the Electrochemical Society* **152**, A2327-A2334 (2005).
205 Jung, H., Shin, J., Chae, C., Lee, J. K. & Kim, J. FeF3/Ordered Mesoporous Carbon (OMC) Nanocomposites for Lithium Ion Batteries with Enhanced Electrochemical Performance. *The Journal of Physical Chemistry C* **117**, 14939-14946 (2013).
206 Lukiyanets, B., Matulka, D. & Grygorchak, I. Quantum mechanic tunneling and efficiency of Faraday current-generating process in porous nanostructures. *arXiv preprint arXiv:1106.5142* (2011).
207 Hua, X. *et al.* Comprehensive Study of the CuF2 Conversion Reaction Mechanism in a Lithium Ion Battery. *Journal of Physical Chemistry C* **118**, 15169-15184, doi:10.1021/jp503902z (2014).
208 Kim, H. *et al.* In Situ Formation of Protective Coatings on Sulfur Cathodes in Lithium Batteries with LiFSI-Based Organic Electrolytes. *Advanced Energy Materials* (2014).
209 Han, H.-B. *et al.* Lithium bis (fluorosulfonyl) imide (LiFSI) as conducting salt for nonaqueous liquid electrolytes for lithium-ion batteries: Physicochemical and electrochemical properties. *Journal of Power Sources* **196**, 3623-3632 (2011).
210 Guerfi, A., Duchesne, S., Kobayashi, Y., Vijh, A. & Zaghib, K. LiFePO< sub> 4</sub> and graphite electrodes with ionic liquids based on bis (fluorosulfonyl) imide (FSI)< sup>−</sup> for Li-ion batteries. *Journal of Power Sources* **175**, 866-873 (2008).
211 Miao, R. *et al.* Novel dual-salts electrolyte solution for dendrite-free lithium-metal based rechargeable batteries with high cycle reversibility. *Journal of Power Sources* **271**, 291-297 (2014).
212 Doe, R. E., Persson, K. A., Meng, Y. S. & Ceder, G. First-Principles Investigation of the Li−Fe−F Phase Diagram and Equilibrium and Nonequilibrium Conversion Reactions of Iron Fluorides with Lithium. *Chem. Mater.* **20**, 5274-5283, doi:10.1021/cm801105p (2008).
213 Tarascon, J.-M. & Armand, M. Issues and challenges facing rechargeable lithium batteries. *Nature* **414**, 359-367 (2001).
214 Biensan, P. *et al.* On safety of lithium-ion cells. *Journal of Power Sources* **81**, 906-912 (1999).
215 Crowther, O. & West, A. C. Effect of electrolyte composition on lithium dendrite growth. *Journal of the Electrochemical Society* **155**, A806-A811 (2008).

216 Qian, J. *et al.* High rate and stable cycling of lithium metal anode. *Nat Commun* **6**, 6362, doi:10.1038/ncomms7362 (2015).
217 Shkrob, I. A., Marin, T. W., Zhu, Y. & Abraham, D. P. Why Bis(fluorosulfonyl)imide Is a "Magic Anion" for Electrochemistry. *J. Phys. Chem. C* **118**, 19661-19671, doi:10.1021/jp506567p (2014).
218 Budi, A. *et al.* Study of the Initial Stage of Solid Electrolyte Interphase Formation upon Chemical Reaction of Lithium Metal and N-Methyl-N-Propyl-Pyrrolidinium-Bis(Fluorosulfonyl)Imide. *J. Phys. Chem. C* **116**, 19789-19797, doi:10.1021/jp304581g (2012).
219 Lu, Y., Tu, Z. & Archer, L. A. Stable lithium electrodeposition in liquid and nanoporous solid electrolytes. *Nature Materials* (2014).
220 Joshi, T., Eom, K., Yushin, G. & Fuller, T. F. Effects of Dissolved Transition Metals on the Electrochemical Performance and SEI Growth in Lithium-Ion Batteries. *Journal of the Electrochemical Society* **161**, A1915-A1921 (2014).

VITA

WENTIAN GU

Wentian Gu was born in Harbin, China. He received his B.S. in Dept. of Materials Science and Engineering from Tsinghua University in 2009, and M.S. in Materials Science and Engineering from Georgia Institute of Technology in 2011. He then pursued a doctoral degree in Materials Science Engineering at Georgia Institute of Technology.